ΠΑΝΕΠΙΣΤΗΜΙΟ ΔΥΤΙΚΗΣ ΑΤΤΙΚΗΣ
ΣΧΟΛΗ ΜΗΧΑΝΙΚΩΝ
ΤΜΗΜΑ ΗΛΕΚΤΡΟΛΟΓΩΝ & ΗΛΕΚΤΡΟΝΙΚΩΝ ΜΗΧΑΝΙΚΩΝ

Διπλωματική Εργασία

Εγκατάσταση, ανάπτυξη, αποσφαλμάτωση συστημάτων και ανάλυση δεδομένων του αναβαθμισμένου ανιχνευτή New Small Wheel του πειράματος ATLAS στο CERN

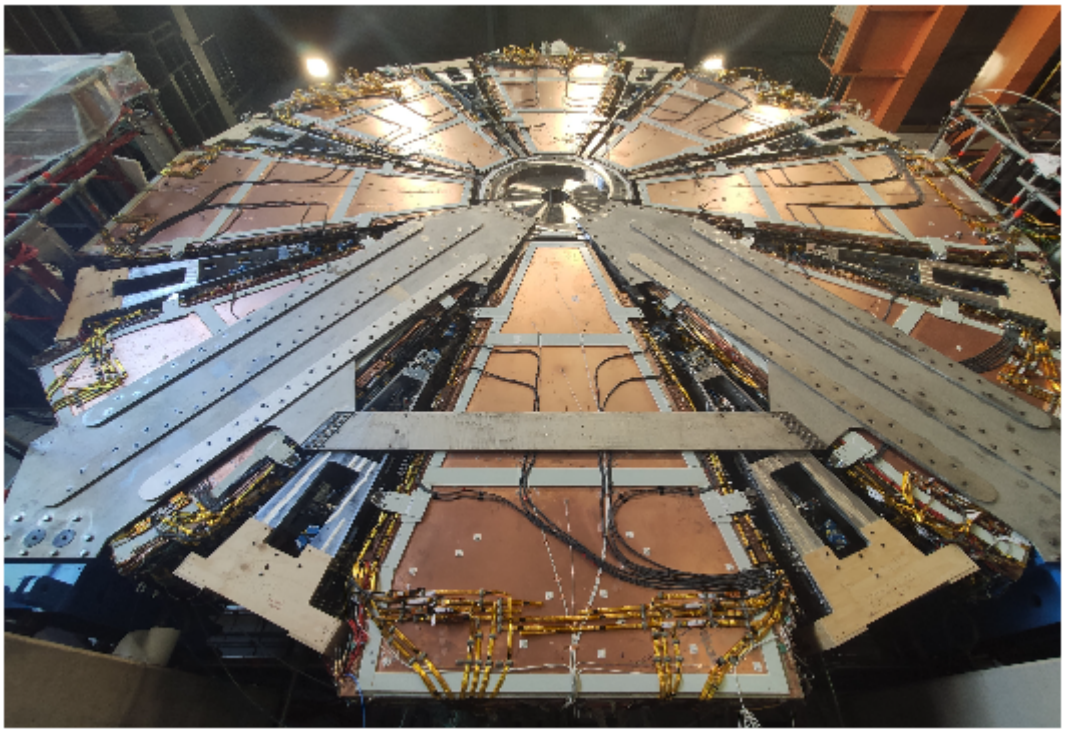

Φοιτητές:

Σταμούλος Ιωάννης
ΑΜ: 47564

Στούρας Νικόλαος
ΑΜ: 47900

Επιβλέπουσα Καθηγήτρια
Ζαχαριάδου Αικατερίνη - Στυλιανή
Καθηγήτρια

Αθήνα - Αιγάλεω, Μάρτιος 2023

UNIVERSITY OF WEST ATTICA
FACULTY OF ENGINEERING
DEPARTMENT OF ELECTRICAL & ELECTRONICS ENGINEERING

Diploma Thesis

Installation, development, debugging of systems and data analysis of the upgraded New Small Wheel Detector of the Atlas experiment at CERN

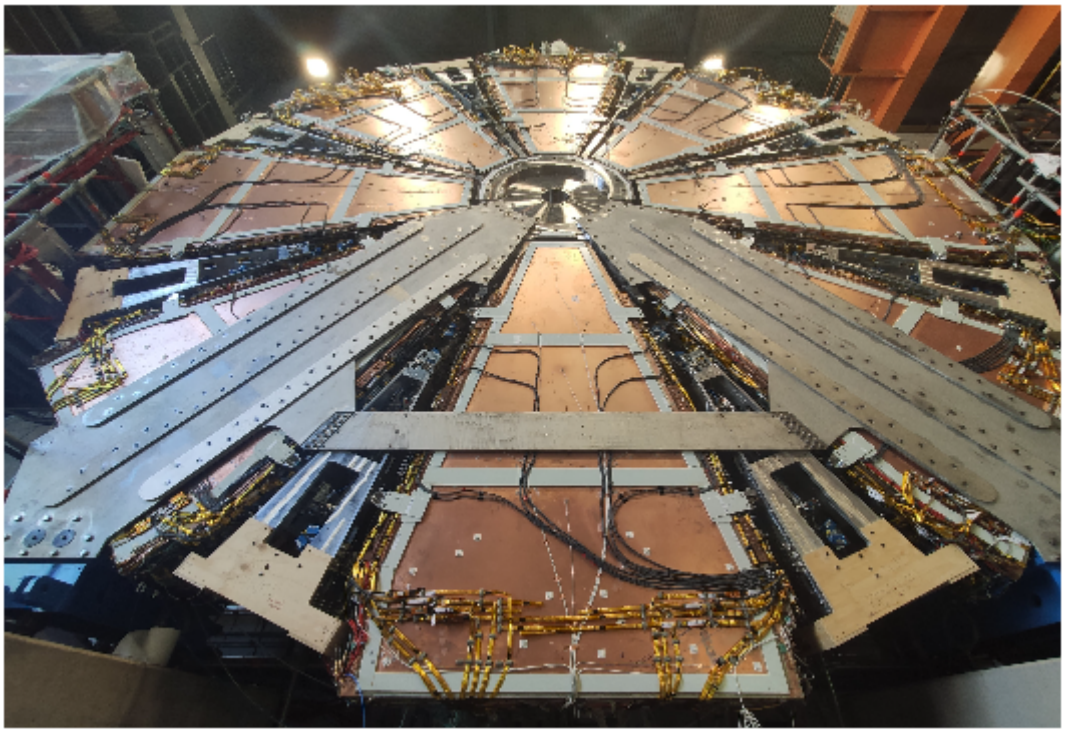

Students:

Stamoulos Ioannis
Registration Number: 47564

Stouras Nikolaos
Registration Number: 47900

Supervisor
Zachariadou Aikaterini - Styliani
Professor

Athens - Egaleo, March 2023

Η Διπλωματική Εργασία έγινε αποδεκτή και βαθμολογήθηκε από την εξής τριμελή επιτροπή:

Ζαχαριάδου Αικατερίνη - Στυλιανή, Καθηγήτρια (Επιβλέπουσα)	Κυριάκης - Μπιτζάρος Ευστάθιος, Καθηγητής	Φασουλιώτης Δημήτριος, Καθηγητής (Ε.Κ.Π.Α.)
Aikaterini -Styliani Zachariadou Digitally signed by Aikaterini-Styliani Zachariadou Date: 2023.03.31 18:10:16 +03'00'	Efstathios Kyriakis-Bitzaros 2023.03.31 15:35:42 +03'00'	Dimitrios Fasouliotis Digitally signed by Dimitrios Fasouliotis Date: 2023.03.31 14:30:08 +03'00'

ΔΗΛΩΣΗ ΣΥΓΓΡΑΦΕΩΝ ΔΙΠΛΩΜΑΤΙΚΗΣ ΕΡΓΑΣΙΑΣ

Οι κάτωθι υπογεγραμμένοι Σταμούλος Ιωάννης του Χαράλαμπου με αριθμό μητρώου 50347564 και Στούρας Νικόλαος του Δημητρίου, με αριθμό μητρώου 50347900 φοιτητές του Πανεπιστημίου Δυτικής Αττικής της Σχολής ΜΗΧΑΝΙΚΩΝ του Τμήματος ΗΛΕΚΤΡΟΛΟΓΩΝ ΚΑΙ ΗΛΕΚΤΡΟΝΙΚΩΝ ΜΗΧΑΝΙΚΩΝ,

δηλώνουν υπεύθυνα ότι:

«Είμαστε συγγραφείς αυτής της διπλωματικής εργασίας και ότι κάθε βοήθεια την οποία είχαμε για την προετοιμασία της είναι πλήρως αναγνωρισμένη και αναφέρεται στην εργασία. Επίσης, οι όποιες πηγές από τις οποίες κάναμε χρήση δεδομένων, ιδεών ή λέξεων, είτε ακριβώς είτε παραφρασμένες, αναφέρονται στο σύνολό τους, με πλήρη αναφορά στους συγγραφείς, τον εκδοτικό οίκο ή το περιοδικό, συμπεριλαμβανομένων και των πηγών που ενδεχομένως χρησιμοποιήθηκαν από το διαδίκτυο. Επίσης, βεβαιώνουμε ότι αυτή η εργασία έχει συγγραφεί από εμάς αποκλειστικά και αποτελεί προϊόν πνευματικής ιδιοκτησίας τόσο δικής μας, όσο και του Ιδρύματος.
Παράβαση της ανωτέρω ακαδημαϊκής μας ευθύνης αποτελεί ουσιώδη λόγο για την ανάκληση των διπλωμάτων μας.

Οι Δηλούντες

Σταμούλος Ιωάννης

Στούρας Νικόλαος

Ευχαριστίες

Σε αυτό το σημείο θα θέλαμε να ευχαριστήσουμε τους καθηγητές μας κα. Ζαχαριάδου Αικατερίνη και κ. Κυριάκη-Μπιτζάρο Ευστάθιο κατ' αρχήν για την ευκαιρία που μάς έδωσαν να δουλέψουμε για μερικά φεγγάρια στο CERN καθώς και για την υποστήριξη που μας παρείχαν σε όλο το διάστημα της παραμονής μας εκεί αλλά και για τον υποστηρικτικό ρόλο που μάς βοήθησε να ολοκληρώσουμε επιτυχώς την εκπόνηση της παρούσας διπλωματικής εργασίας. Θέλουμε επίσης να ευχαριστήσουμε τον κ. Δημήτριο Φασουλιώτη για την συνδρομή του στην επιμέλεια της διπλωματικής μας εργασίας και για την γνώση που μας προσέφερε σε κάθε αλληλεπίδρασή μας. Ευχαριστούμε και την Κουρκουμέλη Αθηνά η οποία για το μεγαλύτερο διάστημα της παραμονής μας στο CERN και το κτήριο 191 είχε καθοδηγητικό ρόλο για εμάς, εφόσον χάρη σε αυτήν εγκλιματιστήκαμε στον χώρο αυτό και στις διαδικασίες του commissioning. Ευχαριστούμε επίσης όλους τους συναδέλφους που είτε πέρασαν είτε είναι ακόμα στην ομάδα του commissioning.

Περίληψη

Η παρούσα διπλωματική εργασία αναφέρεται σε θέματα λειτουργίας και αποσφαλμάτωσης των ανιχνευτών MicroMegas του New Small Wheel (NSW) για το πείραμα ATLAS του CERN κατά την περίοδο της συναρμολόγησης και του ελέγχου τους. Το New Small Wheel αποτελεί μία από τις αναβαθμίσεις του ανιχνευτή ATLAS, προκειμένου να ανταπεξέλθει στις αυξημένες απαιτήσεις του Large Hadron Collider (LHC) και συγκεκριμένα στην αυξημένη ενέργεια και φωτεινότητα. Αυτο το πετυχαίνει μέσω των υπο ανιχνευτών των τεχνολογιών MicroMegas (MM) και small Strip Thin-Gap Chamber (sTGC). Κατασκευάστηκε για να αντικαταστήσει τον παρωχημένο ανιχνευτή Small Wheel ο οποίος δεν τηρούσε τις απαραίτητες προδιαγραφές για το Run-3 του LHC.

Μέσω της διπλωματικής εργασίας αυτής δίνεται μία πλήρης εικόνα για την καθημερινότητα των συγγραφέων κατα την φάση του commissioning στο κτήριο B191 ώστε να μπορέσει κανείς να αντιληφθεί τα προβλήματα που αντιμετώπισαν και την μεθοδολογία που ανέπτυξαν για την γρηγορότερη και βέλτιστη επίλυση προβλημάτων, λαμβάνοντας υπόψη τις αυστηρές προθεσμίες υπό τις οποίες πραγματοποιήθηκαν τα έργα αναβάθμισης του ATLAS.

Στο πλαίσιο αυτής της διπλωματικής εργασίας υπήρξε μεγάλη εξοικείωση με τα υποστηρικτικά συστήματα των ανιχνευτών τεχνολογίας MicroMegas του NSW. Πιο συγκεκριμένα, καλύπτονται ζητήματα γύρω από την αποσφαλμάτωση των συστημάτων χαμηλής τάσης των ανιχνευτών MicroMegas κατά την οποία αντιμετωπίστηκαν κυρίως ζητήματα θορύβου, επικοινωνίας μεταξύ των υποσυστημάτων, τροφοδοσίας και άλλα, με τελικό σκοπό την ορθή λειτουργία των ανιχνευτών κατά τη συναρμολόγηση και μετά την τοποθέτησή τους στους τροχούς New Small Wheel καθώς και τη βέλτιστη απόδοσή τους.

Περιγράφονται όλα τα στάδια ελέγχου, αποσφαλμάτωσης, συναρμολόγησης και τοποθέτησης των υποανιχνευτών στους τροχούς New Small Wheel. Περιγράφονται επίσης οι μέθοδοι και οι έλεγχοι με τους οποίους μπορεί να διαπιστωθεί η ορθή λειτουργία και οι επιδόσεις των ανιχνευτών MicroMegas και γίνεται εκτενέστατη αναφορά στην περιγραφή των όποιων ζητημάτων προέκυψαν καθώς και στους τρόπους με τους οποίους αντιμετωπίστηκαν κατά την περίοδο εργασίας των συγγραφέων στο πείραμα ATLAS στο CERN.

Για την διαπίστωση των επιδόσεων χρησιμοποιήθηκαν διάφοροι έλεγχοι οι οποίοι έδιναν τη συνολική εικόνα όσον αφορά τα επίπεδα ενδογενούς θορύβου και γίνεται εκτενής περιγραφή του τρόπου με τον οποίο οποίο λειτουργούν αυτοί οι έλεγχοι και τι προσφέρουν στην ομάδα της αρχικής τοποθέτησης και επιβεβαίωσης λειτουργίας (commissioning).

Επίσης, περιγράφεται η διαδικασία που ακολουθήθηκε προκειμένου οι ανιχνευτές New Small Wheel να τοποθετηθούν στην τελική τους θέση η οποία βρίσκεται στα end-cap toroids του ATLAS στο Point 1 του LHC. Αναλύεται η διαδικασία επιβεβαίωσης της λειτουργίας τους, ανάλογη αυτής που ακολουθήθηκε στο κτήριο B191, όπως και οι ιδιαιτερότητες που προκύπτουν στις εργασίες αυτές λόγω της μορφολογίας του Point 1. Τέλος, γίνεται αναφορά σε προβλήματα που αντιμετωπίστηκαν εκεί και στα θέματα που παραμένουν ανοιχτά.

Λέξεις – κλειδιά

CERN, Large Hadron Collider, ATLAS Experiment, Muon Spectrometer, End Cap Toroid, New Small Wheel, Commissioning, Troubleshooting.

Abstract

This thesis focuses on the operation and debugging of MicroMegas detectors for the New Small Wheel (NSW) experiment at CERN during their commissioning period. The New Small Wheel is one of the upgrades for the ATLAS detector to meet the increased energy and luminosity demands of the Large Hadron Collider (LHC), achieved through the use of MicroMegas and small Strip Thin-Gap Chamber (sTGC) technologies. It was built to replace the outdated Small Wheel detector, which did not meet the necessary specifications for Run-3 of the LHC.

Through this dissertation, a complete picture of the authors' daily routine during the commissioning phase in building B191 is given, so that readers can understand the problems they faced and the methodology that they developed for faster and optimal problem-solving, taking into account the strict deadlines under which the ATLAS upgrades were carried out.

In the context of this thesis, there were significant issues with the service systems of the MicroMegas detectors of the NSW technology. Specifically, issues are covered around the debugging of low-voltage systems of MicroMegas detectors, during which mainly issues of noise, communication between subsystems, power supply, and others were addressed, with the ultimate goal of ensuring the smooth operation of the NSW detectors during the LHC's Run-3.

All stages of testing, debugging, assembly, and placement of detectors on the New Small Wheel wheels are described. The methods and tests used to determine the correct operation and performance of the MicroMegas detectors are also described in detail, including a description of the issues that arose during the authors' work at the ATLAS experiment at CERN and how they were addressed.

Various tests were used to determine performance, providing an overall picture of the levels of intrinsic noise. These tests and the way they work is described in detail and also an explanation of how they help the commissioning team is given.

The process followed to place the New Small Wheel detectors in their final position, located in the end-cap toroids of the ATLAS at Point 1 of the LHC, is also described. The verification process of their operation is analysed, similar to the one followed in building B191, as well as the peculiarities that arise in these tasks due to the morphology of Point 1. Finally, there is a reference to the problems encountered there and the issues that remain unresolved

Keywords

CERN, Large Hadron Collider, ATLAS Experiment, Muon Spectrometer, End Cap Toroid, New Small Wheel, Commissioning, Troubleshooting.

Introduction **9**
Thesis objective 9
Structure 9
1: CERN, ATLAS and The New Small Wheel **10**
1.1: CERN 10
1.2: The Large Hadron Collider 10
1.3: The ATLAS Experiment 12
1.3.1: The ATLAS sub-detectors 13
1.3.2: The Magnet System 17
1.3.3: The ATLAS Trigger and Data Acquisition Systems 19
1.4: NSW Phase-1 Upgrade 21
1.4.1: The sTGC Detectors 22
1.4.2: The Micromegas Detectors 23
1.4.3 The New Small Wheel Layout 26
2: Electronics Chains of the New Small Wheel **29**
3: New Small Wheel Services **33**
3.1: T-Sensors 33
3.2: Cooling System 35
3.3: Gas System 37
3.4 Power Scheme of the New Small Wheel LV 39
3.5 Fibre Infrastructure - MicroMegas 42
4: Commissioning Workflow and Sector Validation **45**
4.1 Commissioning Workflow 45
4.2 Noise studies - DAQ 48
4.2.1 Baselines 48
4.2.2 Trimmers 53
4.2.3 Noise Runs 54
4.2.4 Pulse Runs 55
5: Troubleshooting **57**
5.1 Noise Related Problems 57
5.1.1 Grounding Issues 57
5.1.2 ICS Noise 67
5.1.3 T-sensor - ELMB related Noise Issues 71
5.1.4: Noise caused by the Cooling System Chiller 75
5.2 Low Voltage Related Problems 79
5.2.1 Polarity, Continuity and Mapping Checks 79
5.2.2 Burnt LVDBs 81
5.2.3 Overheating Connectors 81
6: Installation at Point 1 **83**
7: Conclusions **92**
References **92**
Acronyms **96**

Introduction

Thesis objective

This thesis is a presentation of the contribution of its authors and students of the University of West Attica, Stamoulos Ioannis and Stouras Nikolaos, during their time at CERN. The students were sent to CERN as a part of the collaboration between the two institutes.

The main work of the authors was contributing to the completion of the commissioning of the New Small Wheel, part of the ATLAS detector, and their main tasks revolved around:

- Testing and validating each MM sector of the New Small Wheel both before fully assembling each sector and after assembly as well as on the wheel.
- Tracking and resolving the (many) issues the commissioning procedure unmasked.
- Maintaining an efficient procedure and training new people that eventually populated the Commissioning Team.
- Finding new troubleshooting and problem-solving solutions since new issues were constantly occurring.

Structure

In the first chapter, CERN, LHC, the ATLAS experiment and its sub-detectors are illustrated. Then there is an in-depth description of the New Small Wheel Upgrade and the technologies of the type of detector, specifically the MicroMegas (MM) and the Small-strip Thin Gas Chambers (sTGC). Then we will describe their advantages to the Small Wheel.

We will explain extensively all the electronics used for the New Small Wheel in Chapter 2. Even though we will only focus on the MicroMegas electronics, we will also describe the sTGC electronics. We will provide a detailed description of the inner workings of each board, and we will present their several problems and their respective solutions. We will focus on the Level-1 Data Driver Card (L1DDC) and the MicroMegas Front-End Boards (MMFE8), and we will give a short description of the Address in Real Time Data Driver Card (ADDC).

Chapter 3 discusses all of the crucial New Small Wheel Services, like the Low Voltage infrastructure, the Cooling System, the Gas System and the Fibre infrastructure. We will explain their function extensively and the reasons behind many of the decisions taken in their design.

In chapter 4, we picture the Commissioning workflow in Building 191, explaining every step we followed in the ordinary circumstances of a sector commissioning (testing each sector subsystem and installation on the New Small Wheel). Then the Data Acquisition System (DAQ) tests are defined, which are the baselines, the trimmers, also called thresholds, the noiseruns, and the pulse runs, each contributing different information for the state and efficiency of each sector.

Then in chapter 5, we will give a long list of problems, errors and design flaws. We will discuss their respective solutions in depth since this is the thesis's main chapter and our main area of work during the MicroMegas commissioning.

In chapter 6, we describe the final installation of the NSW at Point 1 where ATLAS is located and all the new challenges and problems that have emerged. Specific issues seen in Building 191 have reappeared, but we had to adapt their solutions to the limiting conditions of Point 1.

1: CERN, ATLAS and The New Small Wheel

Describing ATLAS experiment, LHC and what the New Small Wheels will contribute to the experiment.

1.1: CERN

The European Council for Nuclear Research (CERN) [1], was founded in Geneva, Switzerland, and it is the largest research centre in the world, leading in Particle Physics research, studying matters of fundamental particles and the way they interact with each other.

The CERN convention was signed in 1953 by 12 founding states and entered into force on 29 September 1954. As of today, it has 23 member states (states with specific duties and privileges), three countries are in the pre-stage of Membership, and seven more are Associate Member States. Japan, the Russian Federation and the United States of America hold Observer status with respect to the LHC (Large Hadron Collider), while the United States of America also hold Observer status with respect to the HL-LHC (High Luminosity-LHC). The European Union, JINR and UNESCO also hold Observer status at CERN [2].

The Russian Federation and JINR (located in and mainly funded by Russia) have had their observer status suspended in accordance with the CERN Council Resolution of the 8th and the 25th of March, 2022, respectively, as a result of officially condemning the Invasion of Ukraine by the Russian Federation [3][4]. On the 25th of March it was also decided that any ties between CERN and Belarusian establishments or the Republic of Belarus will be suspended. [67]

1.2: The Large Hadron Collider

The Large Hadron Collider (LHC) [5] is the largest particle accelerator in the world. It started its operation on 10 September 2008 and it is the latest addition to the particle accelerator constellation of CERN. It is located underground in Switzerland and neighbouring France and its circumference is 27 kilometres. It uses superconductive magnets and a number of accelerating structures to give particles along its route large amounts of energy.

LHC is the last accelerator of the CERN accelerator complex, which is a chain of accelerators with increasing energy levels. Each accelerator accelerates a beam of particles to a certain energy level and in succession, it passes this beam to the next accelerator in the complex, which in turn increases the energy level of the beam. The CERN accelerator complex is illustrated in Figure 1.1.

Linear accelerator 4 (Linac4) is the source of the proton beams for the CERN accelerator from 2020. It accelerates negative hydrogen ions to 160 MeV before they enter the Proton Synchrotron Booster (PSB). The ions are stripped of their two electrons during injection from Linac4 into the PSB, leaving only protons. Then they are accelerated to 2 GeV before they are injected into the Proton Synchrotron (PS) where they are further boosted to 26 GeV. From there they are fed to the Super Proton Synchrotron (SPS) which is the last step before the LHC, where they are accelerated to 450 GeV. LHC being the last part of the CERN accelerator complex takes the beam from the SPS through 2 beam pipes, one directing the protons clockwise and the other counter-clockwise, each needing 260 seconds to fill. After that, the LHC needs 20 minutes to energise protons to 6.5 TeV. 2.56 TeV/u (energy/nucleon) for ions and 13 TeV for proton collisions

which take place in the 4 collision points described in Section 1.3. It reached a peak luminosity (which measures how tightly particles are packed into a given space) of $\mathcal{L} = 10^{34} cm^{-2} s^{-1}$.

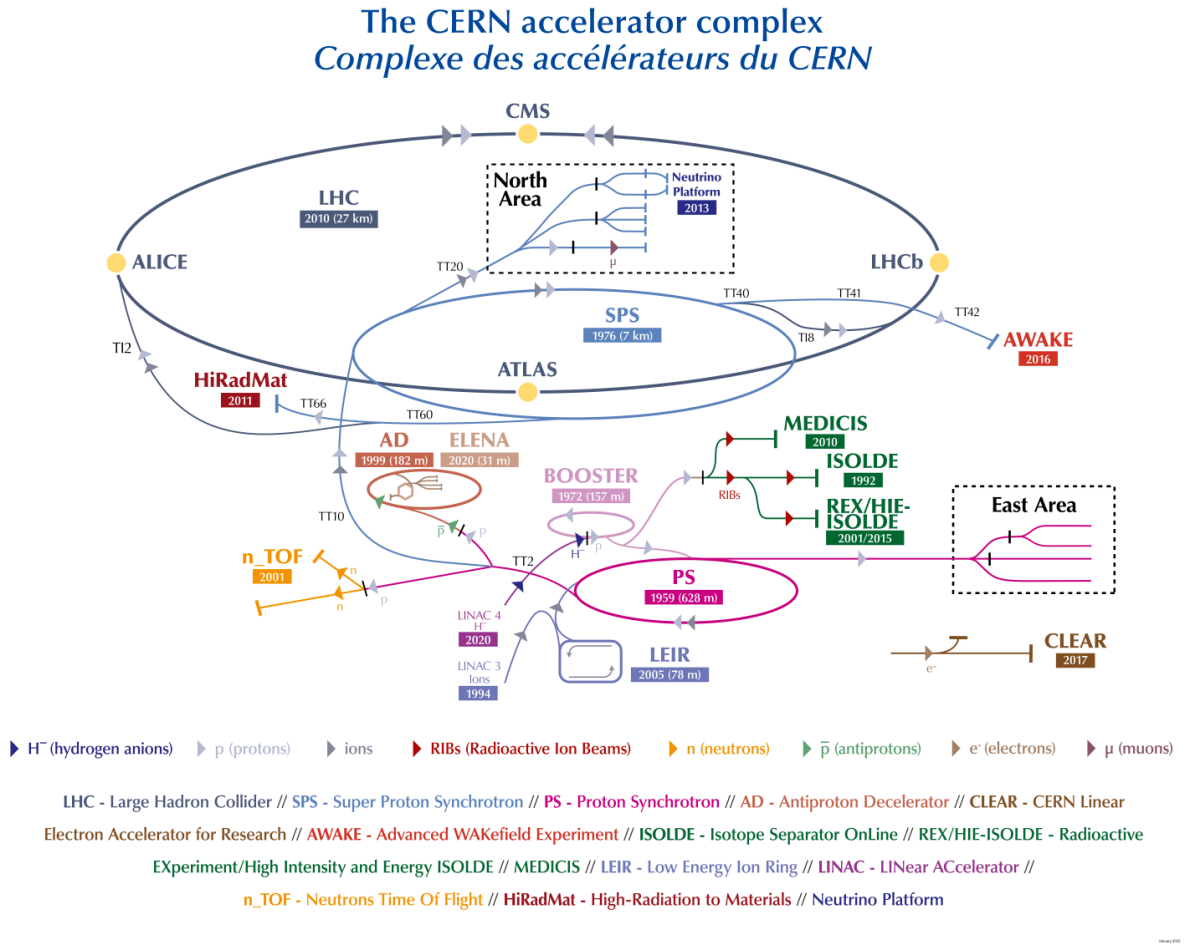

Figure 1.1: The CERN accelerator complex. [6]

Inside the LHC, the two high energy beams travel at a speed near the speed of light until they collide. As mentioned, the beams travel on opposite tracks and through different routes while being kept under ultra-high vacuum. They travel around the accelerator ring by a strong magnetic force provided by the super-conductive magnets. The electromagnets are made of coils with a special electrical wire which is operated at a superconductive state, efficiently conducting electricity with zero resistance and subsequently zero energy waste. This is performed by cooling the magnets to a temperature of -271.3° celsius [5]. For this reason, a large portion of the accelerator is connected to a liquid Helium supply system which cools down the magnets and other supply services.

A total of 9593 magnets of different types and sizes are used to direct the beams along the accelerator. This includes 1232 bipolar magnets 15 metres in length which bend the beams and 392 quadra-polar magnets ranging from 5 to 7 metres in length which focus the beams. Just before the point of collision, one more magnet is used to concentrate the particles in order to increase the chance of particle collisions.

The beams are squeezed down to 64 μm and despite their large number of 100 billion protons per bunch we only get around 19 collisions per crossing. The time spacing between each bunch is 25 ns (at 40 MHz) which does not include some delays caused by some technical

limitations such as the time needed from the dumb kickers to get into an operational state. The average crossing rate is the product of the number of bunches which is 2808 and the revolution frequency, which is 11245 ending up being 31.6 MHz. Multiplying with 19 collisions per crossing we end up with around 600 million collisions per second. Since most protons miss each other at the Interaction Point (Figure 1.2), they carry on the ring time after time, so because of this, the beams keep circulating for hours.

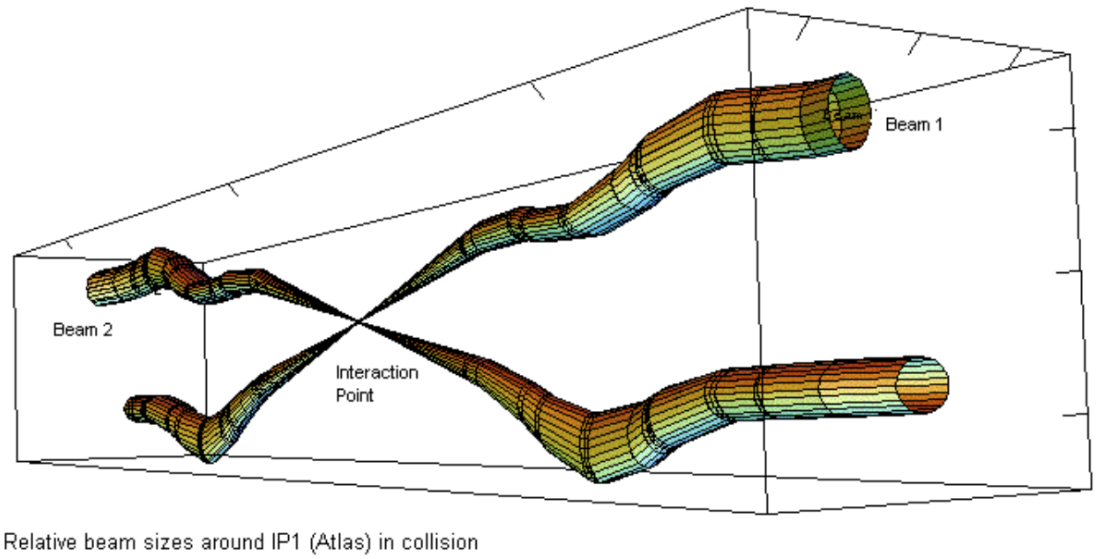

Figure 1.2: Beams interaction point. [7]

The total power consumption of the experiment is around 600 GWh per annum which is around half of CERN's 1.3 GWh annual consumption. For Run 2, it is estimated to be around 750 GWh per annum [8].

All the controls for the accelerator, its services and technical infrastructure are housed under one roof at the CERN Control Centre. From here, the beams inside the LHC are made to collide at four locations around the accelerator ring, corresponding to the positions of four particle detectors

1.3: The ATLAS Experiment

As mentioned above, on the 4 interaction points of the beams of the LHC accelerator, advanced detector systems of different technologies are placed to detect the plethora of particles created by the collisions. These are:

- A Toroidal LHC ApparatuS (ATLAS) [15]
- Compact Muon Solenoid (CMS) [9]
- A Large Ion Collider Experiment (ALICE) [10]
- Large Hadron Collider beauty (LHCb) [11]
- TOTal Elastic and diffractive cross section Measurement (TOTEM) [12]
- Large Hadron Collider forward (LHCf) [13]
- Monopole and Exotics Detector at the LHC (MoEDAL) [14]

ATLAS is one of the two general purpose detectors at the Large Hadron Collider located at Point 1. It investigates a wide range of physics, from the Higgs boson search to the search for extra

dimensions and the particles that could constitute dark matter. Even though it has the same goals as the CMS experiment, it uses a different technical approach and a different magnet system design.

The beams of the LHC collide at the centre of the ATLAS detector, ideally forming new particles which spread across all possible directions. For particle detection, six different detecting subsystems exist which are arranged in layers mapping the paths, momentum and energy of the particles, allowing them to be individually identified. A huge magnetic system bends the paths of the charged particles, showing that their momenta can be measured. The interactions in the ATLAS detector create vast amounts of data. To filter the data ATLAS uses an advanced trigger system to tell the detector which data to record and which to ignore. Complex Data Acquisition (DAQ) and computing systems are used to analyse the interaction event.

ATLAS is the largest detector system ever manufactured [15], it measures 46 metres in length, and 25 metres in width and height, and it weighs around 7000 tonnes.It sits in a cavern 100 m below ground near the main CERN site, close to the village of Meyrin in Switzerland.

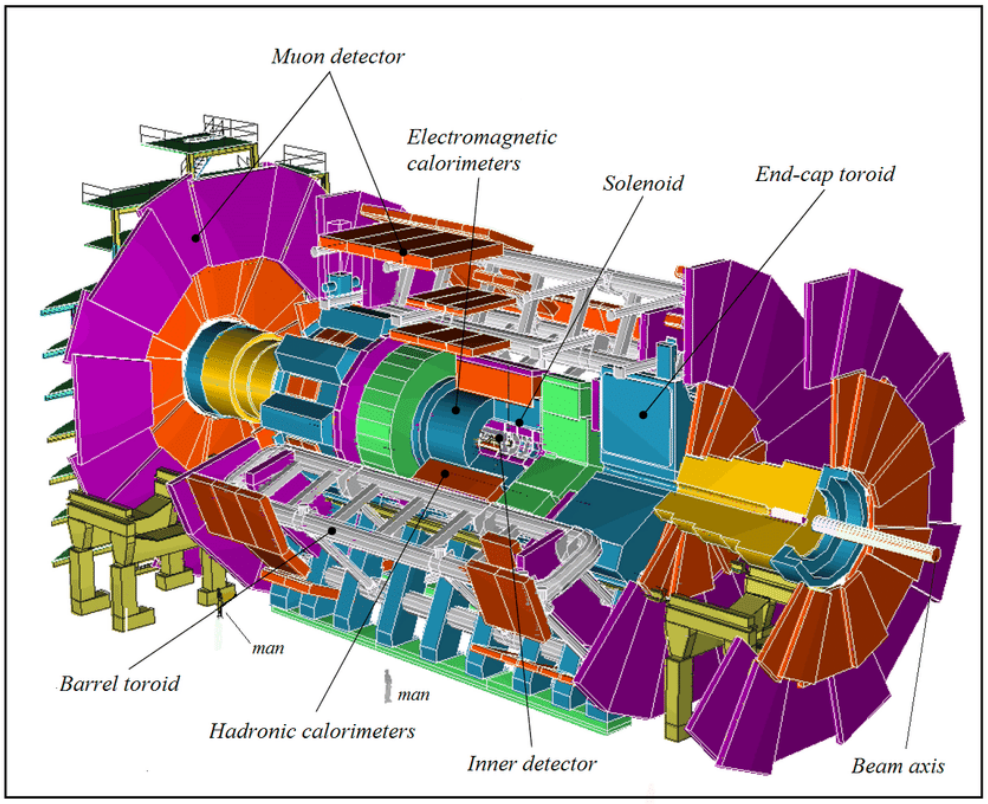

Figure 1.3: The ATLAS detector. [16]

1.3.1: The ATLAS sub-detectors

The Inner Detector (ID)

The ATLAS Inner Detector (ID) [17] provides charged-particle tracking with high efficiency. The ID is 2.3 metres in diameter and 7 metres in length, and it is made of three separate detectors. For analysing the momenta of charged particles, a 2 T solenoidal magnetic field is provided by a superconducting central solenoid which is integrated inside the cryostat of a liquid argon electromagnetic calorimeter.

The Pixel Detector [18] which is the innermost element of the ID contains approximately 80 million channels that are used to provide pattern recognition in order to meet the ATLAS

requirements for track reconstruction of charged particles at the full luminosity of the LHC of $\mathcal{L} = 10^{34} cm^{-2} s^{-1}$ using semiconductor technology. It is the most important detector used in the identification and reconstruction of secondary vertices from the decay of, for example, particles containing a b-quark or for b-tagging of jets. In addition, it provides excellent spatial resolution for reconstructing primary vertices coming from the proton-proton interaction region within ATLAS even in the presence of multiple interactions at the LHC design luminosity.

The Semiconductor Tracker (SCT) [19] hinted by its name, also uses semiconductor technology to provide precision space-point coordinates. The SCT is composed of four cylinders in the barrel and nine discs in each of the two end-caps. Every layer is able to read out a position in two dimensions. There are in all 8448 identical rectangular single-sided p-in-n sensors installed in the ATLAS barrel SCT and 6944 single sided p-in-n sensors, of five different wedge-shaped geometries, in the SCT end caps.

The outer component of the ID is the gaseous/polypropylene fibre Transition Radiation Tracker (TRT) [20]. It consists of three parts, the barrel and two end caps. Its main elements are thin-walled proportional drift tubes called straw tubes. These were chosen as detecting elements because they offer a high degree of modularity of the detector and because they can easily be integrated into a medium producing transition radiation without compromising the continuous tracking concept. The barrel part consists of 52 544 straws 144 cm in length oriented parallel to the beam. The two end-caps each contain 122 880 straws 37 cm in length radially aligned to the beam axis. The operating conditions in the ATLAS experiment at the Large Hadron Collider (LHC) impose stringent requirements on the straw properties. Thus, all choices of materials, the straw design, the active gas, and the operating point were made to ensure safe, and efficient operation in the high radiation environment.

The Calorimeters

The Calorimeters [21] measure the energy of the particles that are created during the collisions while at the same time, they absorb most of these particles. There are two types of Calorimeters based on their technology. The first type is the Liquid Argon Calorimeter (LAr) [22][23] which measures the energy of electrons, photons and hadrons. It consists of metallic layers made of tungsten, copper or lead. These layers absorb incoming particles turning them into new particles of lower energy levels. These particles ionise the Liquid Argon that exists between the layers, in turn producing an electrical current that is measurable. By measuring the distinct currents we can calculate the energy of the particle that hit the Detector. The central region of the Calorimeter detects electrons and photons. To maintain the Argon in a liquid form the Calorimeter is kept at a temperature of -184° Celsius [24]. The barrel of the LAr is 6.4 metres long and 53 centimetres thick and includes 110,000 channels. The LAr end cap is made of the Forward Calorimeter (FCal) and the Hadronic and Electromagnetic end caps. The Electromagnetic end caps are 0.632 metres thick and have a radius of 2.077 metres. The Hadronic end caps are made of two wheels, one at 0.8 metres and one at 1 metre respectively and 2.09 metres in radius. The FCal consists of three modules, measuring 0.45 metres in width and 0.455 in radius [25].

The Tile Calorimeter (TileCal) [26] surrounds the LAr and measures the energy of the hadronic particles that have escaped the LAr without depositing all of their energy there. It consists of scintillating tiles made of steel and plastic. As particles hit the layers of steel, they generate a shower of new particles. The plastic scintillators in turn produce photons, which are converted into an electric current whose intensity is proportional to the original particle's energy. The TileCal

weighs 2900 tonnes, its central barrel is made of 64 wedges, each measuring 5.6 metres long, the two extended barrels are made of 64 wedges 2.6 metres long and it is made of 420,000 scintillating tiles weighing 40 tonnes and includes 9,500 photomultiplier tubes.

The Muon Spectrometer

High energy muons pass through the Calorimeters, leaving behind a fraction of their energy. Therefore, tracking their momenta using the Calorimeters only is impossible. To measure their energy and track their trajectories in high energies another detector is used. As the muons pass through all of the detectors described above undetected, they reach the Muon Spectrometer.

The Muon Spectrometer is the outermost part of the ATLAS detector and measures the energy and trajectory of the muons with high precision. It is located on the outside of the calorimeter modules and covers the space between approximately 4.5m and 11m in radius and 7 m and 23 m longitudinally on both sides of the interaction point. The total volume is approximately 16,000 m3.

The barrel chambers form three cylinders concentric with the beam axis, at radii of about 5, 7.5, and 10 m and are arranged in four disks at distances of 7, 10, 14, and 21–23 m. Both in the barrel and the end-caps, a 16-fold segmentation in azimuth has been chosen that follows the eightfold azimuthal symmetry of the magnet structure. The chambers are arranged in large and small sectors.

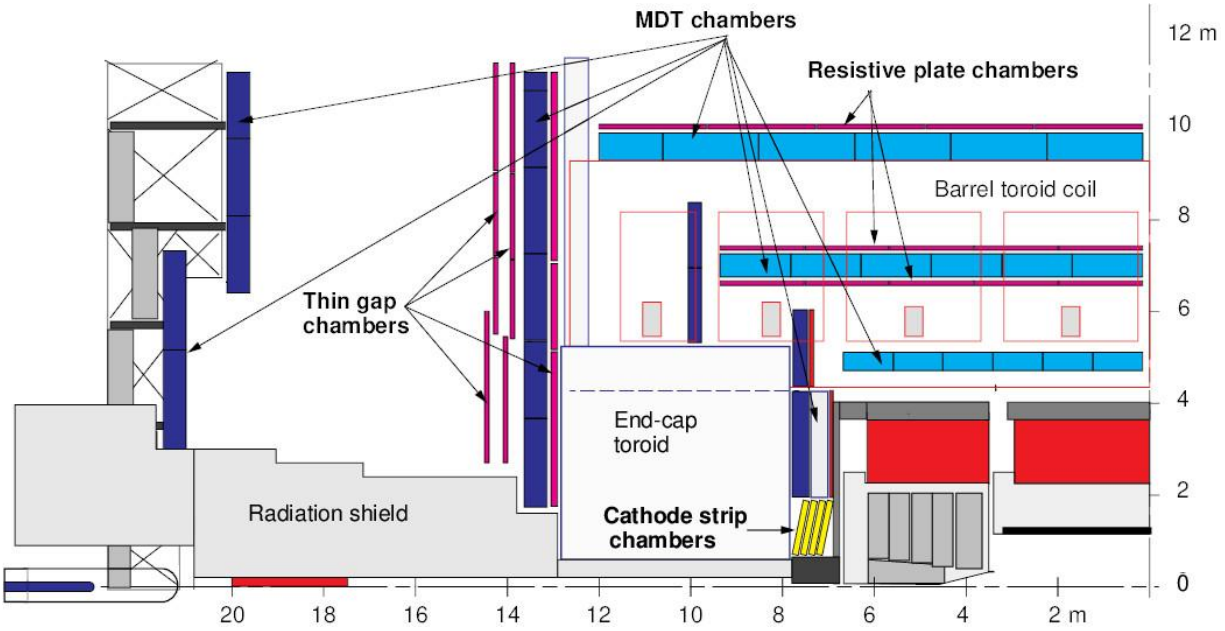

Figure 1.4: Longitudinal section of one quadrant of the muon spectrometer.

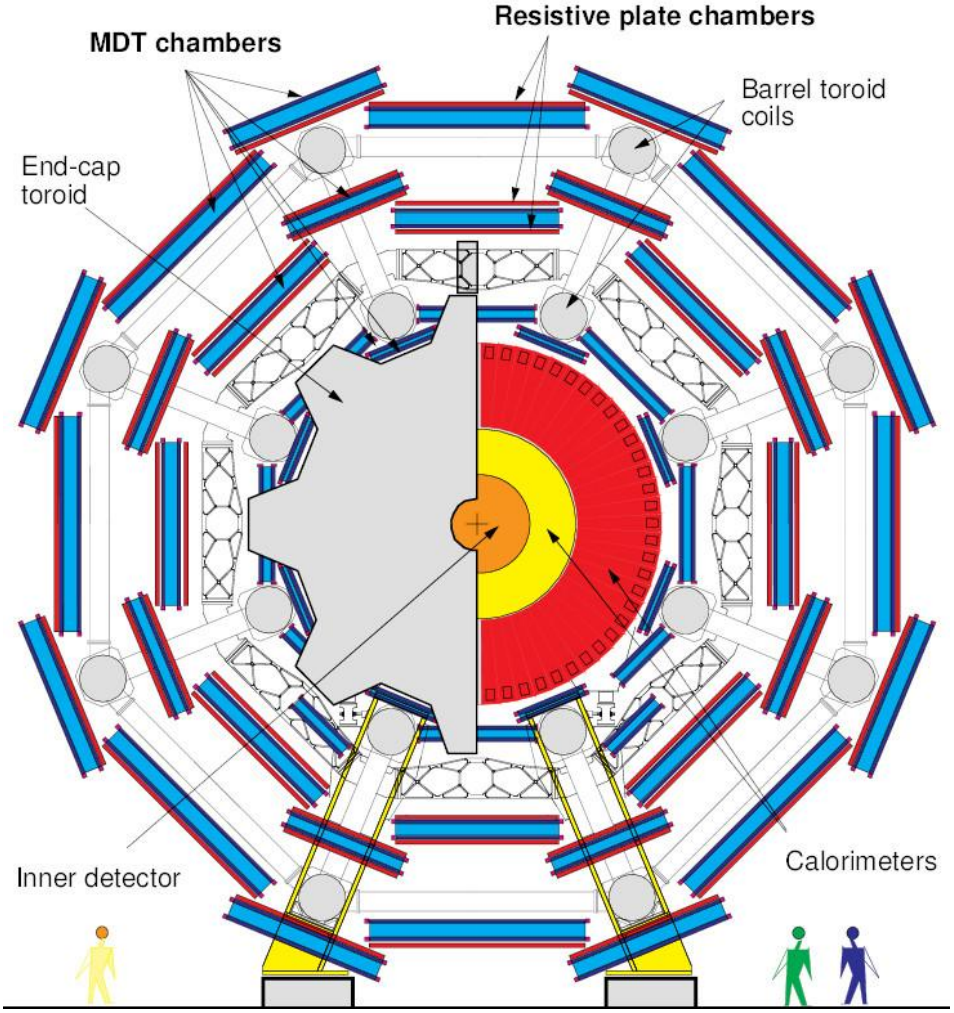

Figure 1.5: Transverse view of the spectrometer.

The Spectrometer is divided into three regions (barrel and end-caps) and consists of four different detector types. The Thin Gap Chambers (TGC), the Resistive Plate Chambers (RPC), the Monitored Drift Tubes (MDT) and the Cathode Strip Chamber (CSC). As shown in Figures 1.4, 1.5, 1.6 MDTs are located both on end caps and in the barrel region, TGC and CSC are located at the end caps and RPC are located in the barrel.

The Spectrometer uses two systems with distinct functionality. Trigger is the most basic functionality and it is provided by the RPC and the TGC. Both types of chambers generate fast signals with a time resolution of a few nanoseconds which are used for level-1 triggering and bunch crossing identification. A spatial resolution of 5–20 mm is adequate for these chambers. It is used in the pattern recognition algorithm and provides the only measurement of the track coordinate in the non-bending plane.

Its second functionality is precision measurement. MDTs cover 99.5% of the area and the CSCs cover the remainder, a very small forward area where particle flows are highest. The precision chambers measure the track coordinates in the bending plane with high precision. For the MDTs no information on the non-bending coordinate and on the bunch crossing time is available. The CSCs, however, do measure both quantities. This are the technologies included in the so called "Small Wheel".

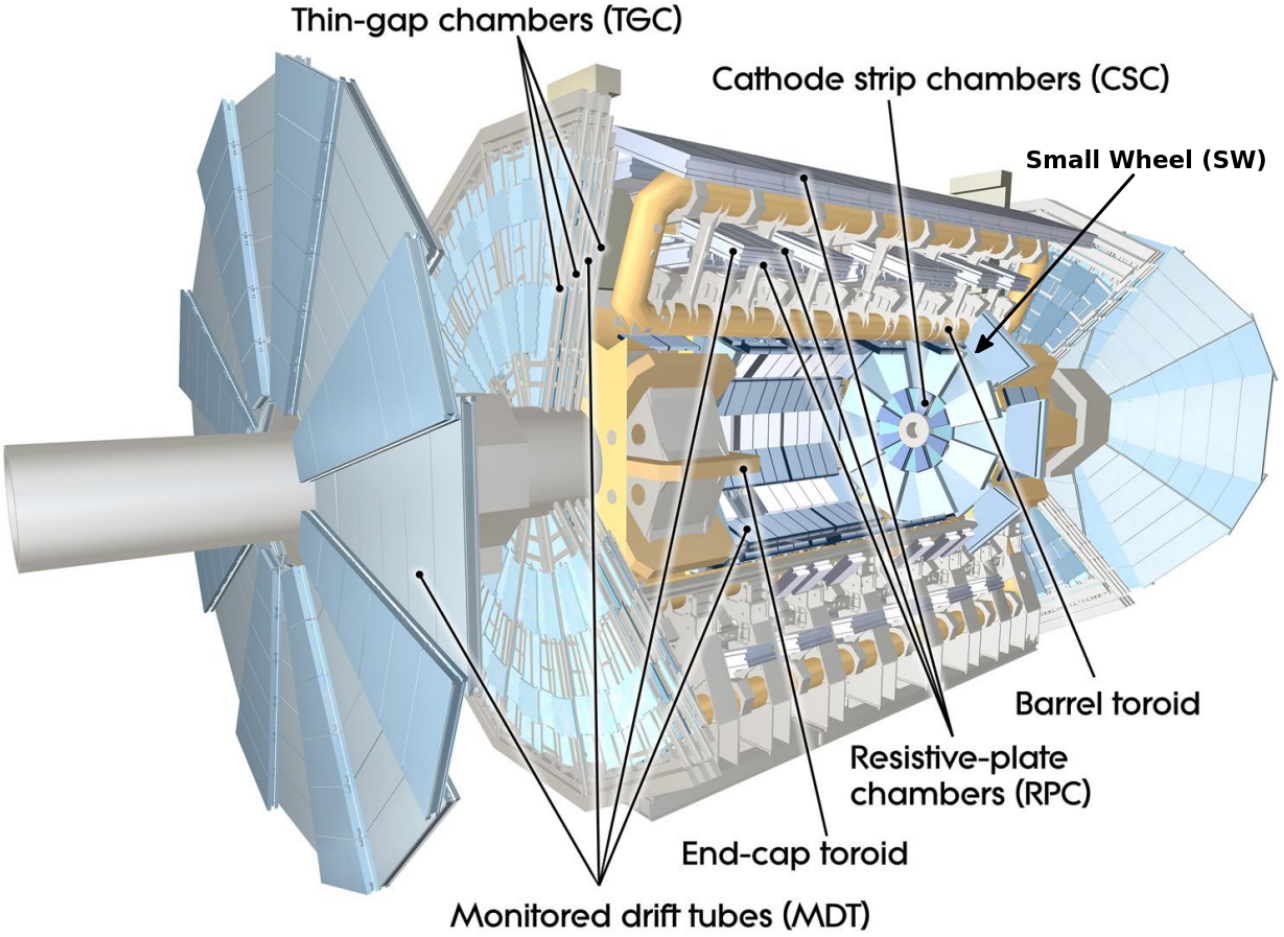

Figure 1.6: Muon spectrometer subsystems. [27]

1.3.2: The Magnet System

ATLAS uses a combination of large superconducting magnets in order to bend the trajectories of large particles so ATLAS can measure their momentum and charge. The Magnet System uses two types of superconducting magnets, one solenoid and three toroids. These magnets are cooled down to approximately 4.5K (-268°C) using liquid helium in order to operate in a superconducting state [28] [29].

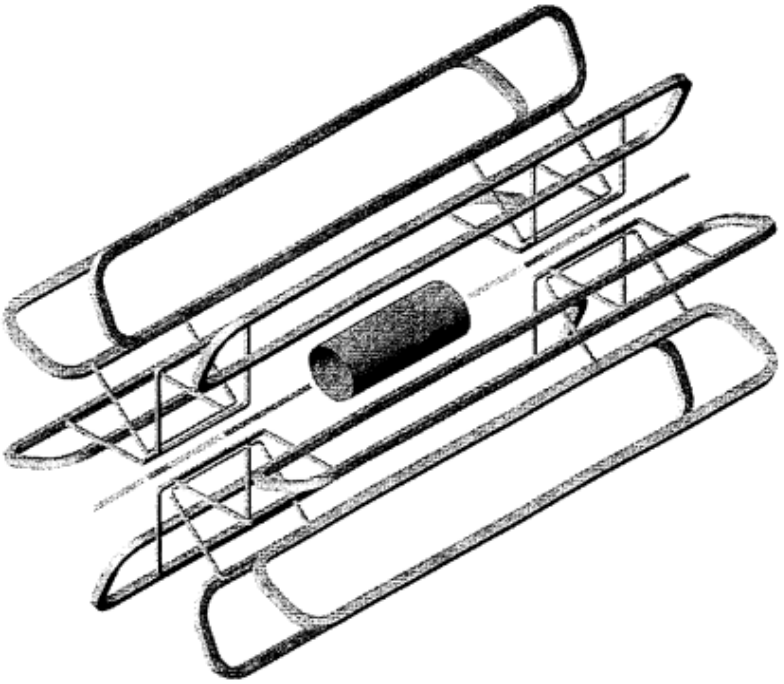

Figure 1.7: Three-Dimensional view of bare windings of the ATLAS Magnet System: The Central Solenoid, the 8 coils of the Barrel Toroid and the two pairs of 8 coils of the End-Cap Toroids.

The Central Solenoid [30] surrounds the Inner Detector, it is 5.6 metres long, 2.56 metres in diameter and just 4.5 centimetres thick and weighs around 5 tonnes. It provides 2 Teslas of magnetic force by embedding over 9 kilometres of niobium-titanium superconductor wires into strengthened, pure aluminium strips that make it possible to minimise interactions between the magnet and the particles being studied. The coil is indirectly cooled using the forced flow of two-phase helium through a single-pass cooling tube. The coil can be cooled down to 4.5 K in 100 hours with a helium gas flow of 20 g/s while keeping the maximum difference in the coil below 40K. The electrical system of the solenoid is designed to keep it under a sustained current of 7.73 kA.

The ATLAS toroids use a series of eight coils to provide a magnetic field of up to 4 Tesla, used to measure the momentum of muons. As mentioned above there are three toroid magnets in ATLAS. The End-cap Toroids, placed at the ends of the experiment, and the massive Barrel Toroid surrounding the centre of the experiment.

At 25.3 metres in length and 20.1 metres in outer diameter, the Barrel Toroid [31] is the largest toroidal magnet ever constructed and weighs about 830 tonnes. It consists of 8 separate coils storing 1.08 GJ of energy and its cold mass is 370 tonnes. It is made of 56 kilometres of Al/NbTi/Cu conductor and uses 100 km of superconducting wire. The eight coils are electrically connected in series and are supplied by a single unipolar DC power supply at 20.5 kA/16 V. The coils are cooled to 4.7K in the indirect mode by circulating liquid helium in tubes welded onto the coil casings.

The End-Cap toroids [32] extend the magnetic field to particles leaving the detector close to the beam pipe. Each end-cap is 10.7 metres in diameter, 5 metres in axial length and weighs 240 tonnes. They also consist of 8 coils and store 0.25 GJ of energy each. Each has a cold mass of 160

tonnes and uses 13 kilometres of the same conductor and the same power supply as the Barrel Toroid. They maintain a working temperature of 4.7 K by flowing helium in a circuit of tubes connected to the outer plates.

1.3.3: The ATLAS Trigger and Data Acquisition Systems

As mentioned in Section 1.2, inside the LHC proton bunches collide every 25 ns. In ATLAS there are up to 1.7 billion collisions happening each second producing over 60 TB of data. These numbers can easily be considered impossible to be processed in real time while most of them are not interesting anyway. This is where the ATLAS trigger and DAQ [33] systems come in. These systems filter the data in real time in order to acquire only the "interesting" data for further processing in no real time.

Triggering consists of two levels. The first level is the hardware trigger where specialised electronic circuits take data from the calorimeters and the muon spectrometer to decide whether they keep each event. From all the events that occur in ATLAS, the level 1 trigger keeps only 100.000 per second for passing it to the level 2 (or software) trigger where 40.000 CPU cores examine data from different detector regions to analyse in detail each event acquired from level 1 trigger and they finally keep only 1.000 events per second for further study.

The Data Acquisition System (DAQ) is responsible for transferring the data from the Readout Devices (RODs) of each sub-detector through all the different stages and to the point where they are permanently saved for offline analysis.

As seen in Figure 1.8 event rejection is made possible through two triggering levels. Level-1 (L1) trigger relies on custom electronics that use the Calorimeter system and a part of the Spectrometer sub-detectors such as the RPC and TGC to define the Regions of Interest (ROI). Separate subsystems search for clusters compatible with electromagnetic, tau and hadronic jet-like energy deposits. The L1 trigger is distributed by the Timing, Trigger and Control system (TTC) to the Readout Systems of the front-ends or in the case of Run-3 to the common element the Front-End Link eXchange (FELIX) [34].

FELIX is the Readout system component which implements the interface to all detector-specific electronics via custom point-to-point serial links. FELIX also acts as the interface to the Data Handlers, monitoring, control & configuration and the Detector Control Systems (DCS) via a commodity multi-gigabit network. TTC information will be received by FELIX from the Local Trigger Interface (LTI) and relayed to detector FE electronics systems in a format satisfying system-specific requirements. The main idea behind the FELIX concept is the development of a modular system which makes it possible to independently upgrade or modify aspects of the system such as computing and buffering resources, network technology or supported point-to-point (or Passive Optical Networks) serial-link protocols. The ability to evolve through further upgrades is a key feature of the Readout System when one considers the performance requirements and long development cycle leading to Phase-II, as well as the long lifetime of the ATLAS experiment beyond this period.

At Run-3, there are 3 important improvements compared to Run-2 for the triggering system. One of these is the High Level Trigger (HLT) software which was upgraded in order to use a multi-threaded technique [35].

The first improvement is the increase of the background rejection for electron/photon trigger candidates through the upgrade of the electromagnetic calorimeter trigger electronics and the corresponding trigger processors.

The next improvement is the rejection of "fake" candidates in the muon endcap spectrometer by installing new precision and high efficiency detectors in the NSW.

The last one is the use of full-event hardware-based charged particle track reconstruction (Fast TracKer (FTK)) during event processing at the HLT CPU farms, e.g. boosting selectivity for certain signatures, as in events with b-jets or τ leptons, and improving object isolation algorithms.

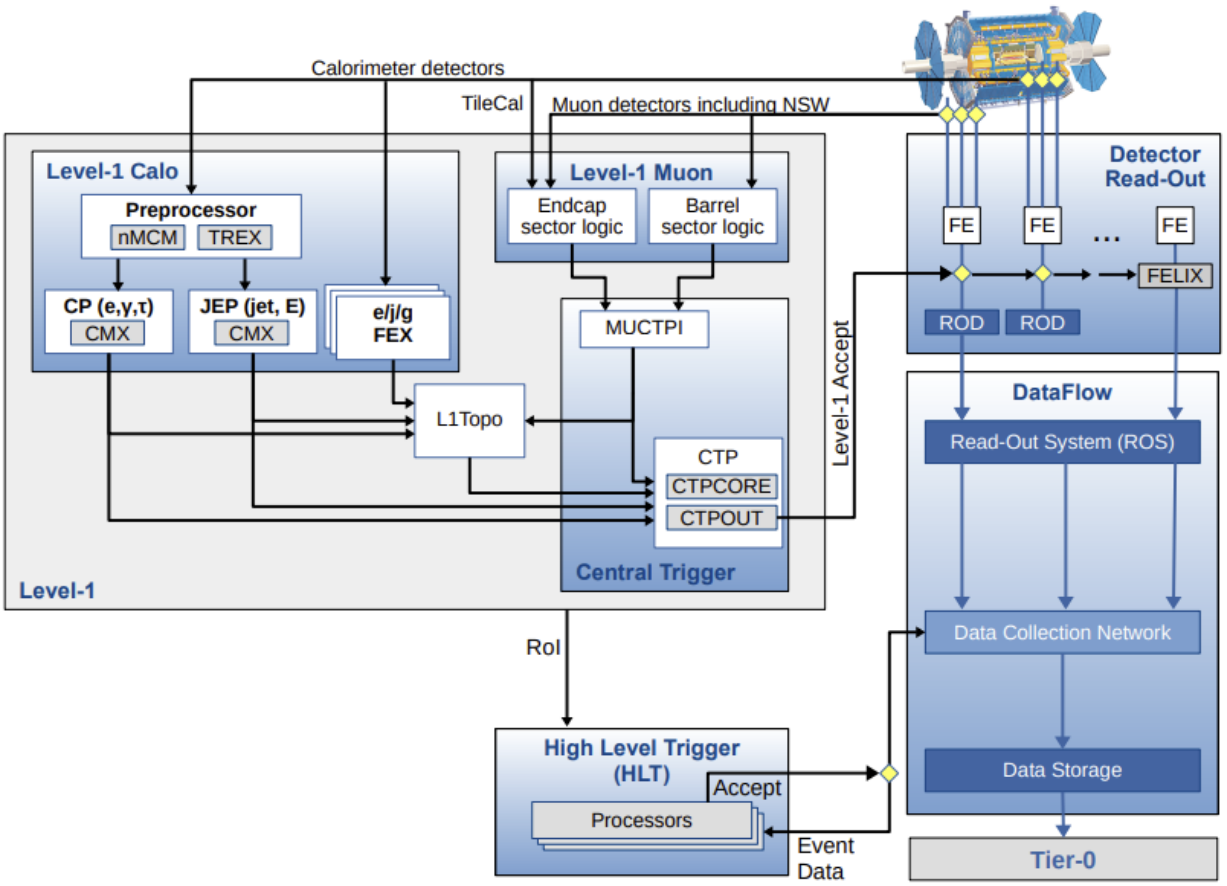

Figure 1.8: The run-3 ATLAS Trigger and DAQ System.

The HL-LHC is expected to start operations in the middle of 2026, and to reach nominally a peak instantaneous luminosity of $\mathcal{L} = 5\,x\,10^{34} cm^{-2} s^{-1}$, corresponding to approximately 140 inelastic proton-proton collisions per bunch crossing, which could be maintained for the duration of the HL-LHC project. Meeting these requirements poses significant challenges to the ATLAS TDAQ system to exploit the physics potential of the HL-LHC fully. Two "custom-hardware" trigger levels were proposed in the Scoping Document that allowed for data streaming off-detector either after an initial trigger decision or in some cases, at the full 40 MHz bunch crossing rate. Since then, the design of the upgraded architecture of the TDAQ system has developed further, resulting in a baseline architecture with a single-level hardware trigger that features a maximum rate of 1 MHz and 10 μs latency.

The hardware-based Level-0 Trigger system is composed of the Level-0 Calorimeter Trigger (L0Calo), the Level-0 Muon Trigger (L0Muon), the Global Trigger and the Central Trigger subsystems. In the L0Calo subsystem, the Phase-I calorimeter feature extraction trigger processors will be complemented by a new forward Feature EXtractor (fFEX) to reconstruct forward jets and

electrons, matching the pseudo-rapidity coverage of the new tracker system. The new L0 Muon subsystem will use upgraded Barrel and Endcap Sector Logic and New Small Wheel (NSW) Trigger Processors, for the reconstruction of muon candidates in the barrel Resistive Plate Chambers (RPCs), in the endcap Thin Gap Chambers (TGCs) and NSW detectors, respectively. The result of the Level-0 trigger decision is transmitted to all detectors and trigger processors, upon which the resulting detector and trigger data, respectively, are transmitted to the Data Acquisition system at 1 MHz through the Readout and the Dataflow subsystems.

Each system and subsystem will be capable of evolving to a dual-level hardware trigger architecture as a mitigation strategy in case pile-up conditions at the HL-LHC either challenge the readout capabilities of detectors to the limits of the bandwidth available or in case the rates of hadronic trigger signatures with the needed thresholds exceed our current allocations. The evolved two-level architecture specifies a Level-0 trigger rate of up to 2-4 MHz and 10 μs latency, followed by a Level-1 trigger rate of 600-800 kHz and latency of up to 35 μs.

1.4: NSW Phase-1 Upgrade

As mentioned in the previous chapters, the several LHC upgrades that have taken place and those that will take place in the future will increase the luminosity even further. These upgrades will result in increased particle rates, collision rates, and data rates and also increased ageing of the detectors. These facts made the ATLAS detector upgrade a necessity. The first upgrade took place during the LHC Long Shutdown 2 (LS2) that took place from December 2018 to July 2022. Long Shutdown 3 (LS3) is planned to take place during 2025-2027 when the High-Luminosity LHC and ATLAS Phase-II upgrades will take place. The Phase-1 upgrade mainly concerns the detector systems installed at the end-caps, the Small Wheel (SW) in particular [36][37]. At high luminosity, there are two main limitations that made the replacement of the Small Wheels inevitable. [38]

The performance of the muon tracking chambers degrades with the expected cavern background rate increase. Studies indicated a substantial degradation of tracking performance in luminosity, in terms of efficiency and resolution in the inner end-cap station at a distance of 7 metres from the Interaction Point, where the Small Wheels are placed. Considering that high resolution momentum measurement greatly relies on the existence of measured points at the Small Wheel level, this degradation heavily affects the performance of the ATLAS detector.

The Level-1 muon trigger in the end-cap region is based on track segments in the Thin Gap Chambers of the middle muon station located after the end-cap toroid magnet. The transverse momentum of the muon is determined by the angle of the segment with respect to the direction pointing to the Interaction Point. A substantial part of the muon trigger rate in the end-caps is noise. Low energy particles, mainly protons, generated in the material located between the Small Wheel and the EM station, produce fake triggers by hitting the end-cap trigger chambers at an angle similar to that of real high pT muons. A study demonstrated that approximately 90% of the muon triggers in the end-caps are fake. As a consequence the rate of the Level-1 muon trigger in the end-cap is eight to nine times higher than that in the barrel region, resulting in a trigger rate higher than the ATLAS limit of 100 KHz.

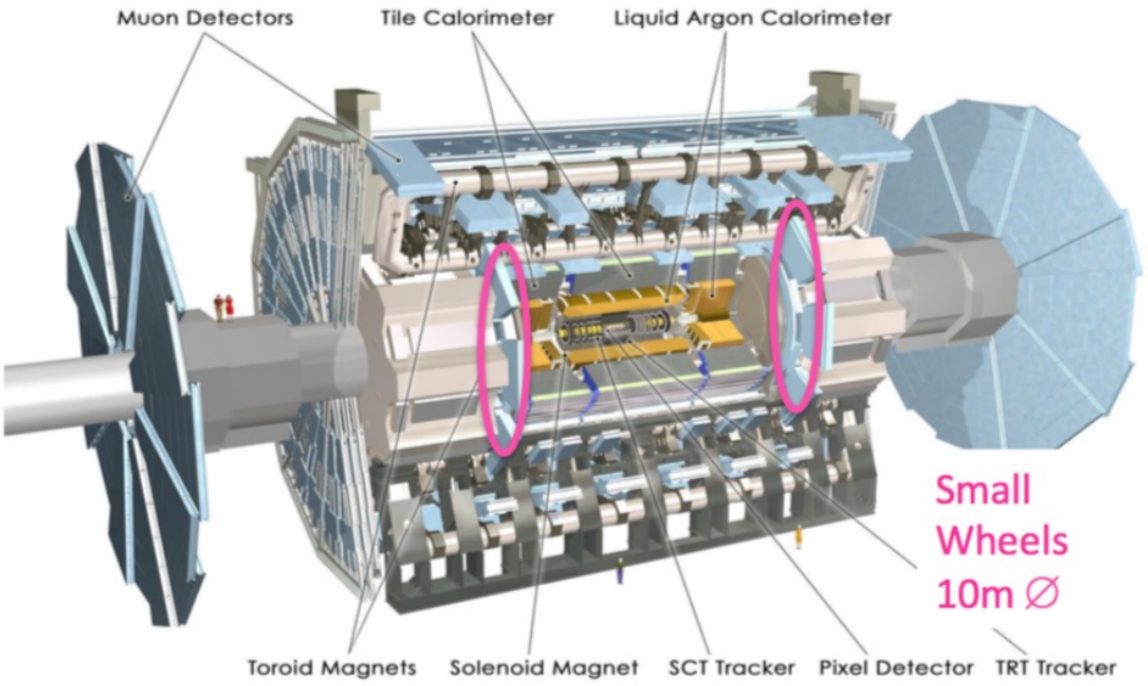

Figure 1.9: Location of the inner End-cap Toroid Small Wheel Detector System. [39]

The New Small Wheel is the upgrade that replaced the Small Wheels, the muon end-cap systems of the ATLAS detector. The goal of this upgrade is to take advantage of the high-luminosity performance which will be provided by the Phase-1 LHC upgrade. NSW meets demanding requirements, such as operation in high levels of background radiation (up to $15kHz/cm^2$), reconstruction of muon tracks with high precision and providing additional information for the Level-1 trigger. Track reconstruction resolution for Offline analysis demands around 100 μm of spatial resolution, and track segments of Level-1 trigger should be able to be processed Online with 1 mrad precision. Two different detector types are used in NSW, MicroMegas (MM) and small Strip Thin Gap Chamber (sTGC). The sTGC will greatly improve the Level-1 trigger function thanks to their great time resolution capabilities whereas the MicroMegas' phenomenal spatial resolution will improve precision tracking. Both of these types of detector use gas-filled detector technologies and will be explained furthermore in Subsections 1.4.1 and 1.4.2.

1.4.1: The sTGC Detectors

The sTGC is an upgraded design of the Thin-Gap Chamber (TGC) detectors. It is a multiwire gaseous chamber that offers high precautions in angular resolution with a very precise time resolution. They consist of a grid of 50 μm gold-plated tungsten wires with a 1.8 mm pitch, sandwiched between two cathode planes at a distance of 1.4 mm from the wire plane. The cathode planes are made of a graphite-epoxy mixture. Behind those planes, there are side strips that run perpendicular to the wires on one side and pads on the other that cover large rectangular surfaces and are placed on 1.6 mm thick PCB with the shielding ground on the opposite side. The strips have a 3.2 mm pitch. To operate these detectors the tungsten wires are held at a potential of 2.9 kV and the chambers are filled with a 55% CO_2, 45% n-pentane gas mixture [40].

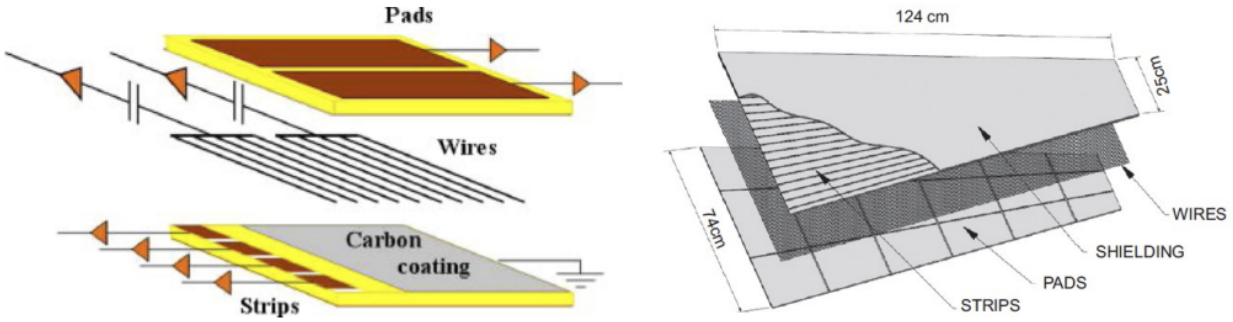

Figure 1.10: The sTGC internal structure.

The pads are used to make a ¾ coincidence to identify muon tracks roughly pointing to the interaction point. They also provide information on which strips should be used to acquire a precise measurement in the bending coordinate, for the online muon candidate selection. The azimuthal coordinate is obtained by grouping wires together since only 10 mm precision is required.

The working principle of these detectors is based upon the ionisation of the gas mixture that is caused when a charged particle passes through the chamber as it continues its trajectory. By ionising the gas, pairs of electrons and positive ions are created which under the effect of an electric field, drift towards the anodes and the cathodes respectively. The electrons created by the ionisation of the gas can meet the closest tungsten wire, which as mentioned above is kept under high voltage, and hit other gas molecules gaining enough energy to cause an avalanche effect. The avalanche electrons reach the anode in an instance conducting a very brief negative signal in the corresponding wire, while the positive ions require a much longer period to reach the cathode due to their much lower drift velocity and the long distance they have to travel. Each anode wire is equipped with its own readout channel, basically making it an independent detector of a certain channel coordinate [41].

1.4.2: The Micromegas Detectors

The Micromegas (Micro Mesh Gaseous Structure - MM) [42] technology was developed in the middle of the 1990s; the detectors consist of a parallel-plate where the amplification takes place in a thin gap, separated from the conversion region by a fine metallic mesh. The MM operation is based on the ionisation of the gas by charged particles traversing the drift space where an electric field of a few hundred V/cm is applied. The electrons, produced by the ionisation, drift towards the mesh and the amplification region, where the signal is created by means of an electric field of about 40–50 kV/cm; the mesh is kept in position by a grid of 128 μm high pillars built on the readout board. The drift time of the electrons in the conversion gap depends on the drift gas, the drift distance and the drift field and typically takes several tens of nanoseconds (about 100 ns in the ATLAS NSW baseline configuration), while for the amplification process, a fraction of a nanosecond is required. As a consequence, a fast pulse of electrons on the readout strips is produced. With an electric field in the amplification region 50 to 100 times stronger than the drift field, the mesh is transparent to more than 95% of the electrons. The electron avalanche takes place in the thin amplification region, immediately above the readout electrode. The drift of the electrons in the conversion gap is a relatively slow process. The ions that are produced in the avalanche process move, in the opposite direction of the electrons, back to the amplification mesh. Most of the ions are produced in the last avalanche step and therefore close to the readout strip. Given the

relatively low drift velocity of the ions, it takes them about 100 ns to reach the mesh, still very fast compared to other detectors. It is the fast evacuation of the positive ions which makes the MM particularly suited to operate at very high particle fluxes.

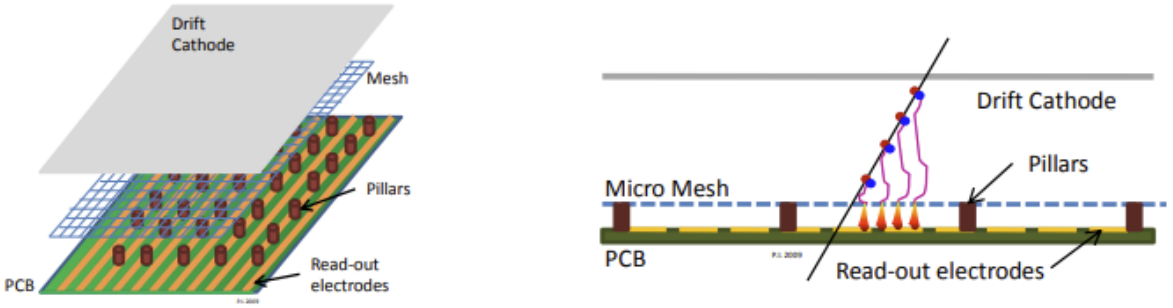

Figure 1.11: Sketch of the layout and operating principle of a MM detector.

The original MM design was vulnerable to sparking. Sparking occurred when the total number of electrons in the avalanche reached a few 10^7. To reach a satisfactory detection efficiency while maintaining a minimum of ionising muons, a gas amplification of the order of 10^4 is required. Ionisation processes that produce more than 1000 electrons over distances comparable to the typical lateral extent of an avalanche carry the risk of sparking. Sparks may damage the detector and readout electronics and lead to large dead times as a result of HV breakdown. Dead time is the amount of time after each incident in which the detector system is unable to record any event.

For the MM detectors that were developed for the New Small Wheel, a spark protection system has been installed. By adding a layer of resistive strips on top of a thin insulator directly above the readout electrode the MM become spark-insensitive. The readout electrode is no longer directly exposed to the charge created in the amplification region, instead, the signals are capacitively coupled to it. By adding this protection some fraction of the signal height is lost but the chamber can be operated at a higher gas gain and thus have spark intensities reduced by about three orders of magnitude.

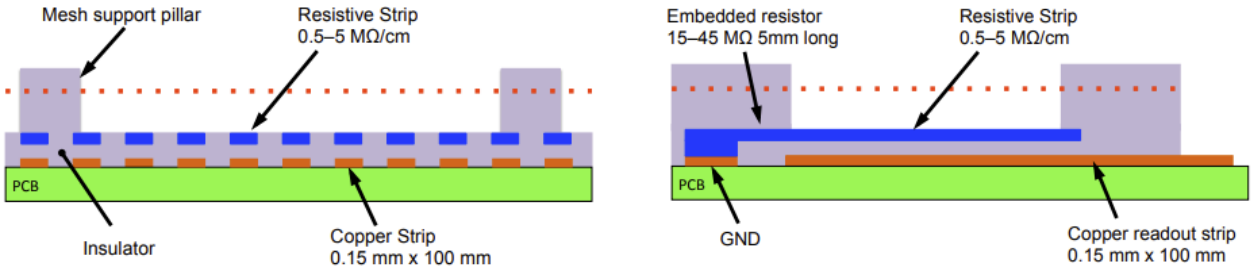

Figure 1.12: Spark protection principle.

The detector concept with resistive strip spark protection has been extensively tested in hadron and neutron test beams up to rates far exceeding the ones expected in ATLAS.

The MM detectors for the NSW notably differ in two ways from the original MM scheme. Firstly, the resistive-strip protection scheme is used, as described above. Secondly, instead of applying negative HV on the amplification mesh and keeping the resistive strips at ground potential,

positive HV is applied to the resistive strips and the amplification mesh is connected to the ground. This scheme resulted in a more stable operation of the detectors. Thus sparks cause a much smaller concern. The spark-induced current can be evacuated very quickly to ground through the mesh and the mesh potential does not change. Further advantages of the modified HV scheme are the better focusing of the field lines between the amplification mesh and the resistive strips, leading to a better charge collection on the resistive strips, and a considerable simplification in the detector construction.

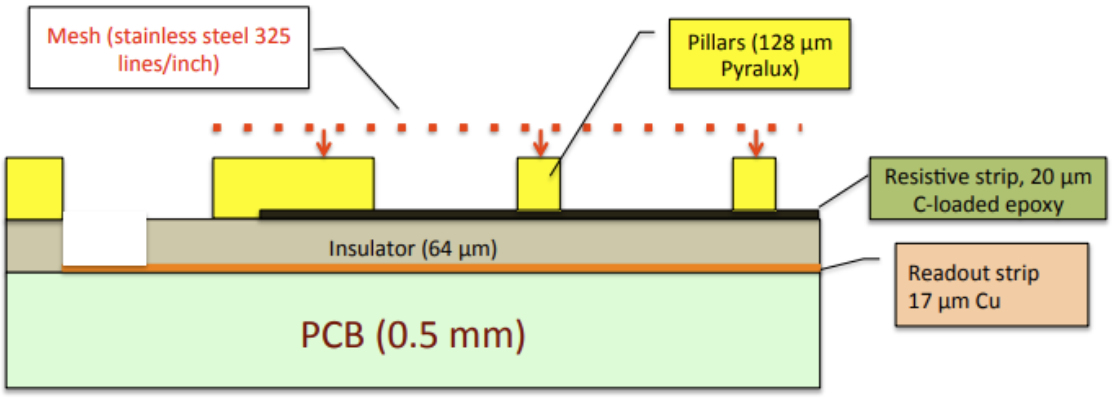

Figure 1.13: Internal structure of the MM.

Contrary to most of the MM detectors now in operation, in the present implementation the amplification mesh is not integrated in the readout structure. The advantages for large-area detectors are that the mesh size is only limited to the mesh fabrication size and stretching machines and not to the size of the individual PCBs, it facilitates detector opening and cleaning and lastly, it separates PCB production from mechanical construction.

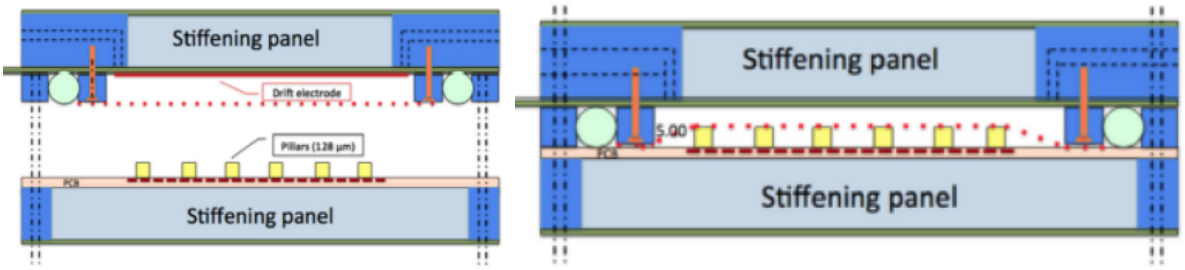

Figure 1.14: Construction schema for the ATLAS Micromegas detector.

For the operation of the ATLAS NSW Micromegas, a nominal value of 550V was selected for the strips (subject to change depending on the condition of each sector) and a value of -300V for the drift cathode. The chambers are filled with a 93% Argon, 5% CO_2, and 2% Isobutane gas mixture [43].

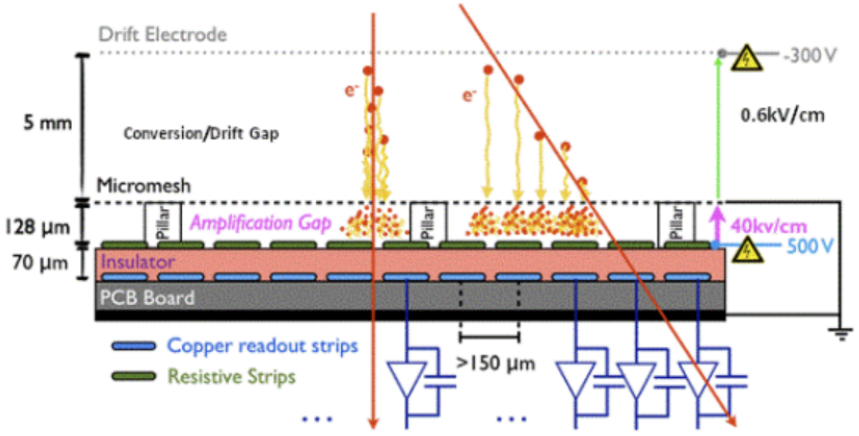

Figure 1.15: Schematic view of Micromegas detector. [44]

1.4.3 The New Small Wheel Layout

The New Small Wheels consist of 16 detector planes, also called Sectors divided into two multilayers (IP for the Interaction Point side and HO for the opposite side). Each multilayer is made of four sTGC and four Micromegas detector planes. As mentioned previously, the sTGC is primarily deployed for triggering given their single bunch crossing identification capability. The detectors are arranged in the following order: sTGC-MM-MM-sTGC. This is done to maximise the distance between the two sTGC multilayers. Online track hit reconstruction is done with limited accuracy, therefore increasing the distance between the two multilayers helps attain an improved online track segment angle reconstruction resolution. Above we described how the Micromegas have exceptional precision tracking capabilities. This is due to their small 5 mm gap and their 0.5 mm strip pitch.

Eight planes per technology were chosen so as to provide a redundant detector system that will be able to perform its functionalities for years to come. With eight layers per detector, track reconstruction can be done reliably with high precision under the conditions described in Section 1.4. The NSW was designed in such a way that even if several detector channels fail, detector performance can stay within ATLAS requirements.

Each of the two wheels will have eight small and eight large sectors. This configuration eliminates dead zones as there are regions covered by both the small and the large sectors. The four multilayers are supported by the Spacer-frame structure.

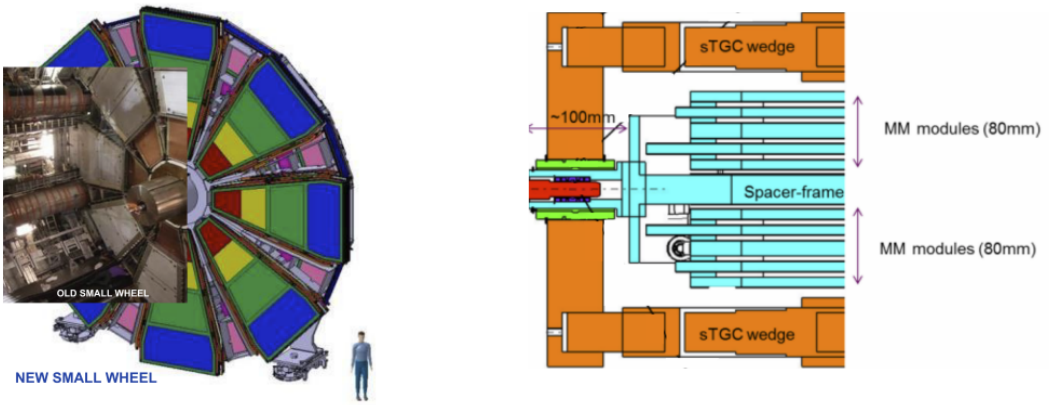

Figure 1.16: Left: Sketch of the NSW structure compared to the current SW. Right: Cross section of a NSW sector integrated with its mechanical support structure. [45]

For the Micromegas, where this diploma thesis is focused on, each layer was produced in two modules. For each size of sector, two different modules were made. Therefore, four different module types were made, two for the Small Sectors (SM1, SM2) and two for the Large Sectors (LM1, LM2). Each Micromegas layer is also split into eight PCB areas. Module one includes PCBs 1 through 5 and module two includes PCBs 6 through 8 (shown in Figure 1.18). Also, the numbering of the PCBs starts from the inner radius at PCB 1 and finishes at PCB 8 at the outer radius. Each PCB and therefore each sector has two sides, named lowering and rising, taken after the numbering order of the sector, meaning the side that "sees" a lower numbered sector is the lowering side and the side that "sees" a higher numbered sector is the rising side.

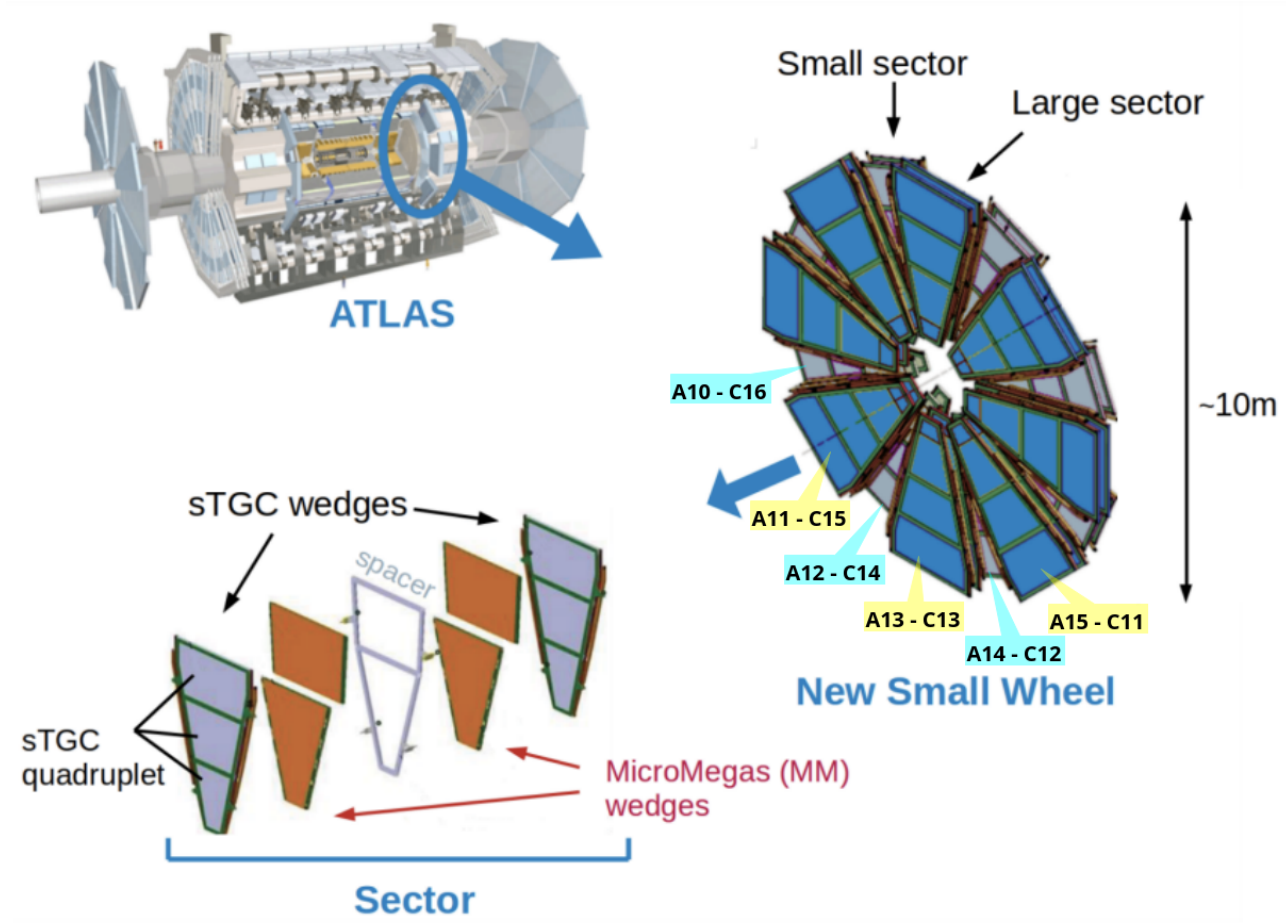

Figure 1.17: NSW detector layout. The exploded diagram shows the different constructions that male a full NSW Sector. [47]

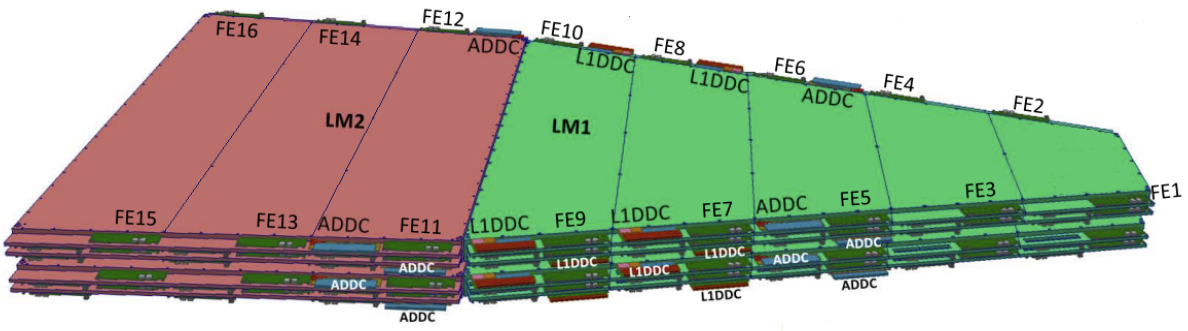

Figure 1.18: Layout of the electronics of one wedge of the MicroMegas Detector. [46]

Each PCB is read by two Front-Ends, one on the lowering and one on the rising side. The MicroMegas Front End Boards (MMFE8) use eight of the specialised ASICS, the Venetios MicroMegas (VMM). Each VMM has 64 channels. This leads to 512 channels per MMFE8 and in turn 1024 channels per PCB. Therefore the total number of Micromegas channels can be calculated as:

$$number\ of\ channels\ per\ PCB\ x\ PCBs\ per\ layer\ x\ layers\ per\ sector\ x\ sectors\ x\ wheels\ = 1024\ x\ 8\ x\ 8\ x\ 16\ x\ 2\ =\ 2,097,152\ channels$$

The outstanding number of channels the MicroMegas detectors offer, ensure the granularity the future runs require.

The sTGCs electronic channels work in a similar fashion, but they are significantly fewer than those of the MicroMegas, 333,744 to be exact.

2: Electronics Chains of the New Small Wheel

In this chapter, we will start to get a grasp of the upgraded electronics system of the New Small Wheel. Each part was developed to meet the new Triggering and Data Acquisition (DAQ) requirements in the end-cap region. These upgrades will improve the triggering capabilities of the forward region of the Spectrometer while maintaining excellent muon track detection capabilities in the increased radiation and data flow circumstances of Run3 and Run4.

To read the vast number of channels (strips) of the NSW (2.1 m for MM and 331k for sTGC as mentioned above) in high data rates of (21 KHz/cm^2 at Phase-II), radiation levels (1700 Gy) and magnetic fields (0.4 T) several new-era electronics needed to be developed by the CERN and ATLAS R&D teams. Commercial off-the-shelf (COTS) electronics are not up to spec in these harsh conditions. In addition to the specifications mentioned previously, these electronic parts should also meet strict spatial and energy consumption needs and should also take into consideration that said parts will be difficult to access once installed.

Considering the triggering demands, Phase-I L1 rates should be at 100 KHz while For phase-II there are two schemas in consideration. A one level 1 MHz trigger schema and a two level schema which includes a Level-0 accept rate of 1 MHz and Level-1 accept rate of 400 KHz. Said schemas are planned to be able to take full advantage of the planned High-Luminosity LHC upgrade during LS3.

The NSW electronics paths are split in three. The MicroMegas electronic paths, one for trigger and one for readout and the sTGC trigger path. The paths are described in Figure 2.1.

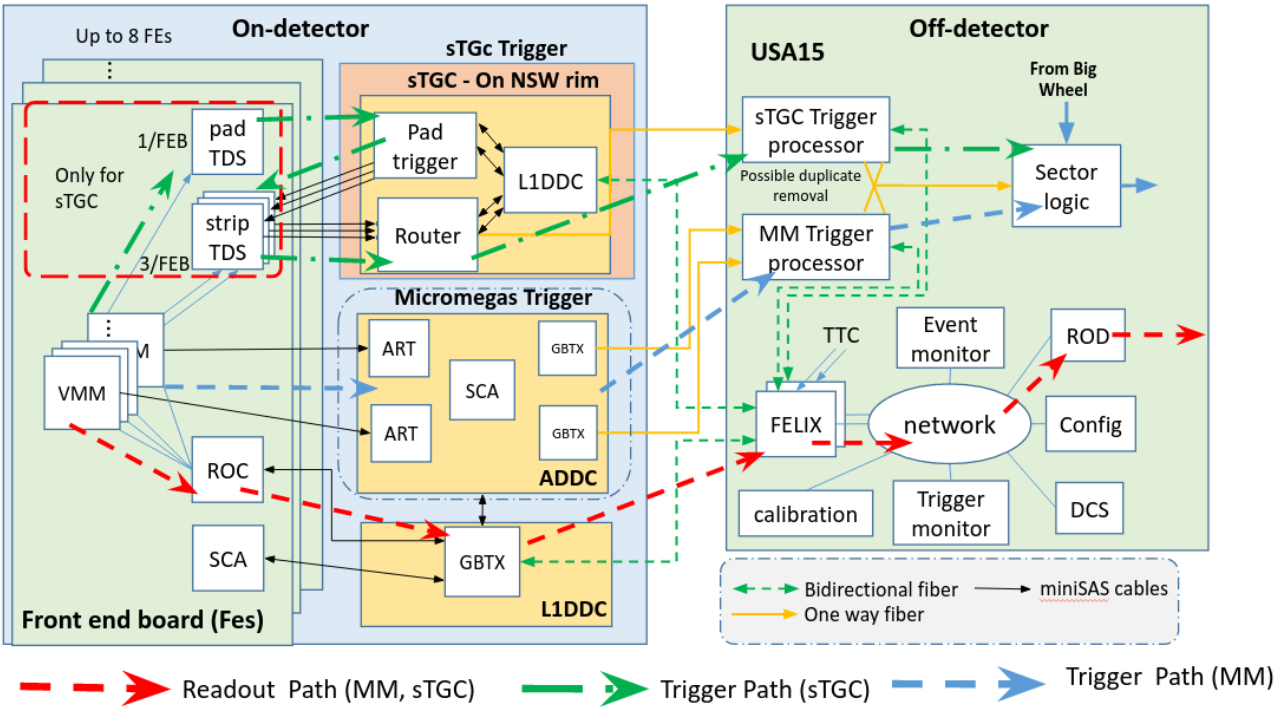

Figure 2.1: Trigger and Readout paths of the MM and sTGC Detectors.

On the left part of Figure 2.1, the On-detector electronics are presented. These electronics have to withstand enormous amounts of radiation and magnetic fields. These cards include the Front Ends boards, the Level-1 Data Driver Card (L1DDC) [48], the Address in Real Time (ART) Data Driver Card (ART DDC - ADDC), The Pad trigger and Router all of which are made of radiation hardened Application Specific Integrated Circuits (ASICs). The communication is done

through a custom serial attached Small Computer System Interface (SCSI) with the use of miniSAS connectors and twinax cables.

On the right side of Figure 2.1, we can see the off-detector electronics. The FELIX (which was described in Subsection 1.3.3), the Trigger processor, the Sector logic and more vital services that can run on commercial Computing Systems such as the Read Out Drivers (ROD), the Detector Control Systems (DCS), the event monitoring, the configuration, the trigger monitor and the calibration. These systems are located in the Underground Service ATLAS (USA15) room which is near the ATLAS detector itself but free of magnetic fields and radiation. This room hosts most of the electronic systems of ATLAS.

To summarize, the MicroMegas Front Ends use the VMM ASICs and specifically eight of them (6 for the sTGC front end). Each VMM has 64 analog inputs that correspond to strips of the detectors. Each MMFE8 has 512 analog channels and each Sector needs a total of 128 MMFE8s. Given that the two wheels are populated by a total of 32 sectors, 4096 MMFE8s are currently in place on the New Small Wheels. The sTGC Front Ends also use the VMM ASICs. Therefore, the VMM fulfils two purposes. It sends data through the two trigger paths in order to recognise a Level-1 Accept signal and after receiving this signal it sends data through the L1DDC [49] which, among other duties, sends data to the off-detector electronics, specifically through the FELIX.

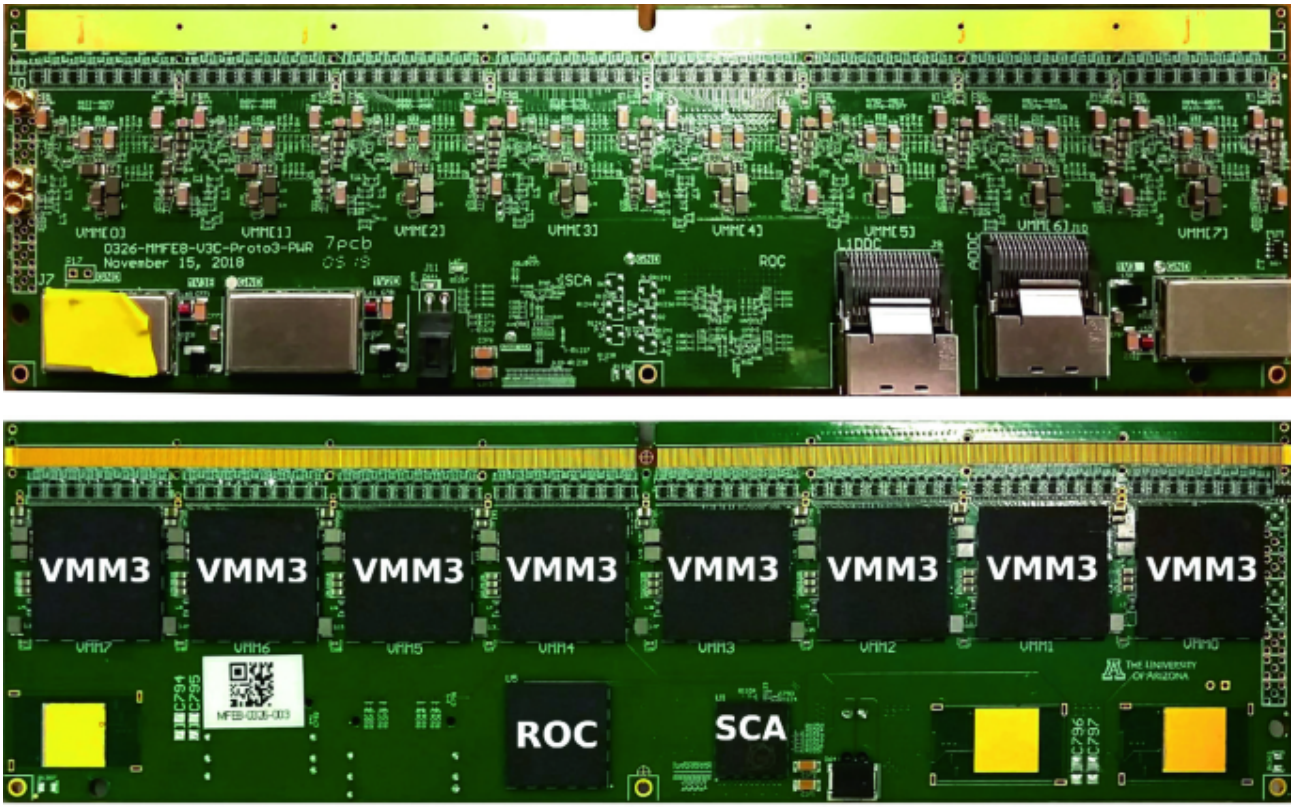

Figure 2.2: The MMFE8 board (front and back).

Each front end also features a Readout Controller ASIC (ROC) [50]. For the case of the MMFE8, the ROC is responsible for accepting all 512 analog signals and performing a series of multiplexing and modulation and serialisation procedures on the data in order to transfer them through the miniSAS twinax cables to the L1DDC at a rate of 320 Mb/s.

Both front end types also feature a Slow Control Adapter ASIC (SCA). The SCA is responsible for configuring and monitoring the front end boards and all of the ASICs. It's through the SCA that temperature, voltage and current data are read to monitor the state of the detectors through the DCS [51].

Additionally to the ASICs mentioned above, the sTGC front end boards also include the pad and the strip Trigger Data Serialiser (pad-TDS, strip-TDS) ASICs [52]. These ASICs are used to find trigger signals through the pads and strips of the sTGC detectors.

The two trigger paths work independently and the data from each one are combined before they are sent to the next trigger module. In total, the sTGC trigger path included the pad/wire Front Ends and the strip Front Ends, which then connect to the pad Trigger board, the Router and the L1DDC and at the end of the chain the sTGC Trigger Processor is located at the off-detector electronics side. Concerning the trigger path of the MicroMegas, the chain included the MMFE8s, the ADDCs and the MicroMegas Trigger processor.

For the MicroMegas Trigger path, the VMM ASICs of each MMFE8 send the address of the channel that detected an energy deposition (hit) higher than the threshold set by the ART, to the ADDC. Each ADDC can connect to 8 MMFE8s which means 64 VMMs. Each ADDC hosts two ART ASICs [53] that receive an ART signal from the VMMs every 25ns. The two ART ASICs multiplex the ART data and select in real time which data will be sent to the GBTX ASICs [54] and in turn will be sent by fibre optics to the off-detector MicroMegas Trigger Processor. The ADDC is also connected to the L1DDC which sends configuration data through the FELIX [55] which provides timing data. In total, 512 MicroMegas ADDCs and 512 sTGC ADDCs are installed on the New Small Wheel (16 per sector per detector technology).

Due to the physical differences and the use of different types of electronics, the MicroMegas and sTGC detector technologies of the New Small Wheel use different Trigger Processors with specialised trigger algorithms for the reconstruction of track candidates in each Bunch Crossing (BC). This trigger data is sent to the Sector Logic boards [56] which in turn correlate the data with track candidates of the Big Wheel system in order to define the final Level-1 Accept signal. The Level-1 Accept signal is transferred through fibre to the FELIX which in turn sends it to the L1DDC. The L1DDC is connected to eight MMFE8s and sends the Level-1 Accept signal to the ROC ASICs in order to start the data-taking procedure.

As previously mentioned the electronics chain that is used for the readout of the data of the sTGC and Micromegas is common. The VMMs export the amplitude of a recorded pulse in the strips, the electric charge and consequently the energy of the particle and also the time of appearance of the charge correlated to the Bunch Crossing Clock. The VMMs execute a selection algorithm when they receive a Level-0 Accept from the ROC and send selected data to the ROC. The ROC stores the Level-0 Accept trigger data until it receives a Level-1 Accept signal in which case it selects which data will be driven to the L1DDC, and then in turn to the FELIX at a rate of 4.8 Gbps through fibre. The FELIX will in turn send the data to the ReadOut Devices (ROD).

In total 1024 L1DDC are installed on the NSW, 512 for the MicroMegas and 512 for the sTGC. In the following chapter, the necessary services to run the New Small Wheel detectors and their electronics will be described. These services are present on and off the detectors.

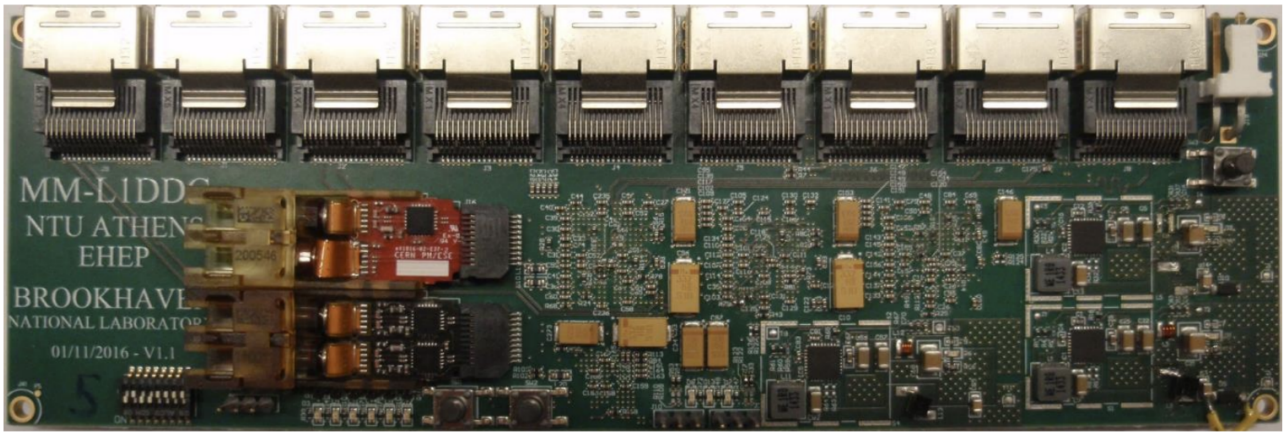

Figure 2.3: The MicroMegas Level-1 Data Driver Card (L1DDC).

3: New Small Wheel Services

Here is a brief description of the NSW services (cooling, gas, grounding, LV, HV, T-sensors) followed by the problems and day-to-day challenges that came up and the solutions that were implemented.

Along with the detectors and their peripheral electronics, several side services were necessary for the proper function of the New Small Wheel. These services include:

- The T-sensors to monitor the temperatures on various spots on each PCB
- The cooling system with its subsystems which is responsible for cooling down the electronics
- The gas system with its respective subsystems
- The power scheme including the Intermediate Conversion Stage (ICS) power supplies, the branch controllers and the New Generation Power Supplu (NGPS) generators
- Fibre infrastructure

3.1: T-Sensors

Starting with the T-sensors they are some resistive sensors whose resistance depends on the applied temperature. They are located on several spots on each wedge's surface as well as on the input and output of the cooling pipes of each layer. In total, each sector has twenty-six (26) T-sensors on the MicroMegas split by thirteen (13) on each side (IP and HO). Nine (9) out of thirteen (13) on each side are spread out on the surface of the MM detectors, while the remaining four (4) sensors are connected to the input and output on both Rising and Lowering sides.

The T-sensors are connected to the DCS through the ELMBs (Embedded Local Monitor Board) so it is able to monitor the temperatures in real time (also used for the MDT DCS). Also, the DCS saves each measurement of each T-sensor so any user can see past values of the temperatures. An ELMB is shown in Figure 3.1.

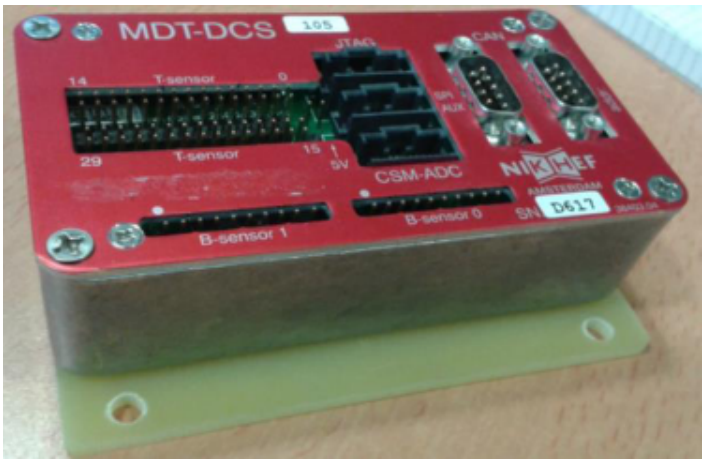

Figure 3.1: The ELMB board.

A user is able to monitor the temperatures of each T-sensor through the FSM GUI. This is a graphical tool through which someone can monitor or control the vital functions of the New Small Wheel. While commissioning there was available only a fraction of the functions it offers to the control and monitoring of the New Small wheel generally so at that point through the FSM GUI one could:

- Monitor and control the NGPS Generators status
- Monitor and control the LV elements of the MM and sTGC sectors
- Monitor and control the HV elements of the MM and sTGC sectors
- Monitor the T-sensors

Below is an example of how a sector's T-sensor values look like through the FSM GUI (Figure 3.2). You can see a snapshot of the values of the T-sensors on Side A's Sector 1 as well as their topological position on the sector's surface. The two sector instances are shown, one for each side. "Z2" stands for IP side while "Z3" stands for HO side. Outside of the surface, you can see the temperatures on the input and the output channels of the Rising and Lowering sides. The values in FIgure 3.2 are shown in mllidegrees Celcius. In a later software it was updated to show degrees Celcius.

Finally, you can notice that one value is null and in a red background. This is due to a problem with that sensor's communication with the monitoring system. Such problems will be described extensively in the Troubleshooting chapter.

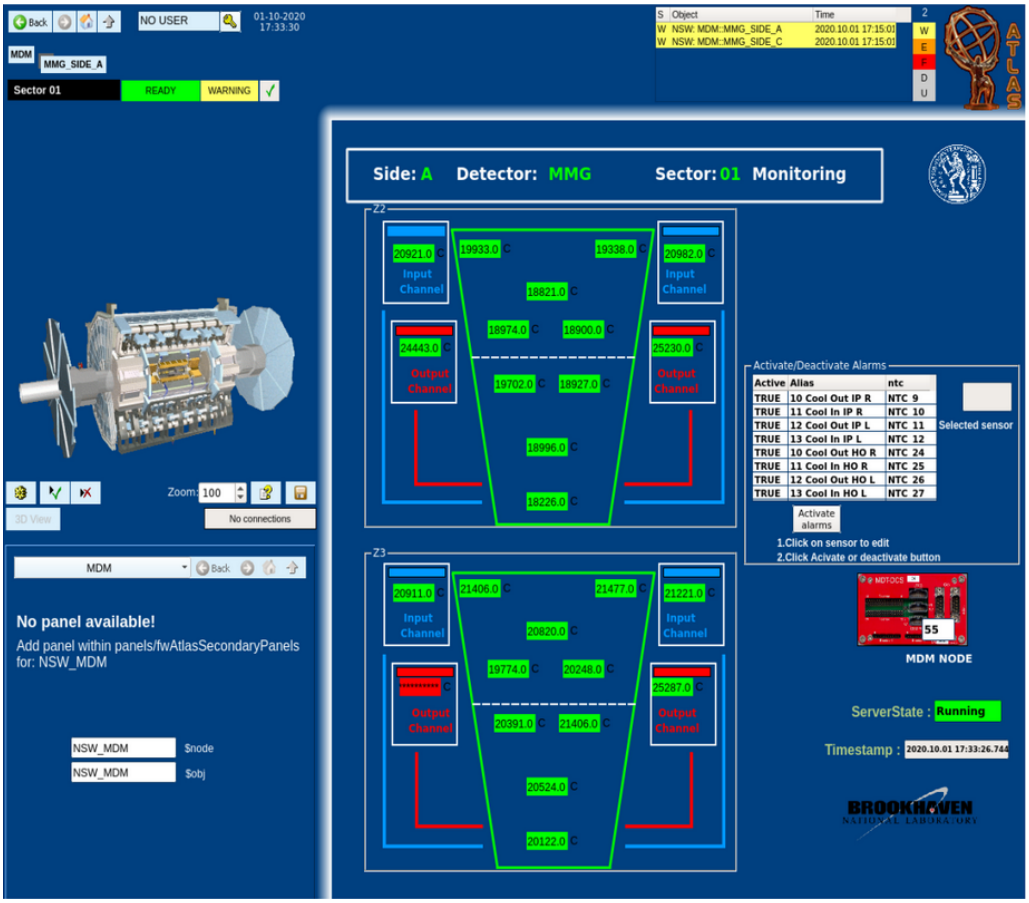

Figure 3.2: T-sensors Temperatures Through FSM GUI.

3.2: Cooling System

Concerning the cooling it is a water cooling system which consists of cooling pipes and an active cooling station also called "the chiller". The pipe network goes through the various subsystems of the New Small Wheel. It is mainly split on a main pipe for the upper part of the wheel and another one for the bottom part of the wheel as you can see in Figure 3.3 below:

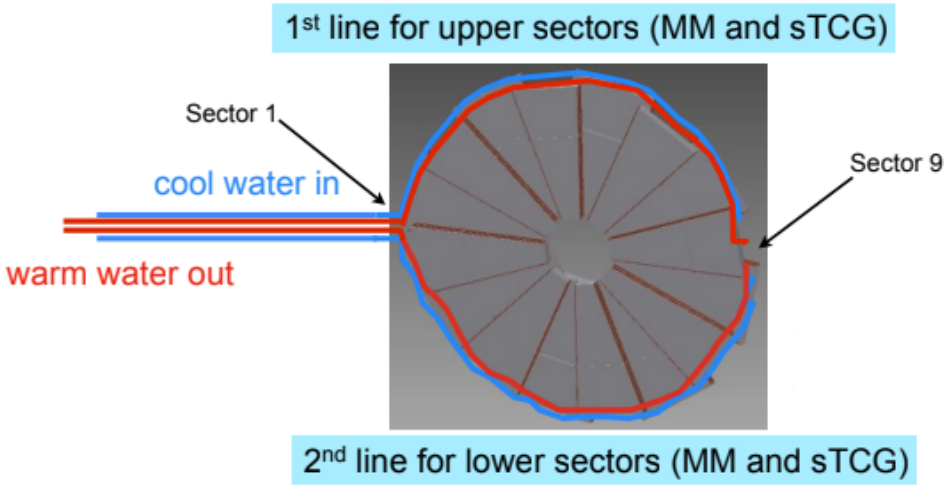

Figure 3.3: NSW Upper and Lower Cooling Loops. [57]

For each part of the wheel, the main cold branch is split into three sub-branches which are the MM, sTGC and the Rim ELX branches. From that point, each of these sub-branches are split further to serve the elementary parts of their instances. For example, the MM sub-branch is split on each sector's MM detectors, the sTGC sub-branch splits to each sector's sTGC detectors and the Rim ELX branch splits to each RIM crate and 2 ICSs per 1 Small and 1 Large NSW sector. After this point, each subsystem is joined back together and then all the subsystems are joined again to form the main hot pipe of the loop.

As for the cooling station, it is the system that actively cools down the water. This system introduced some noise problems while commissioning and it will also be described in the Troubleshooting chapter. In Figure 3.4 you can see a visual representation of what was described above.

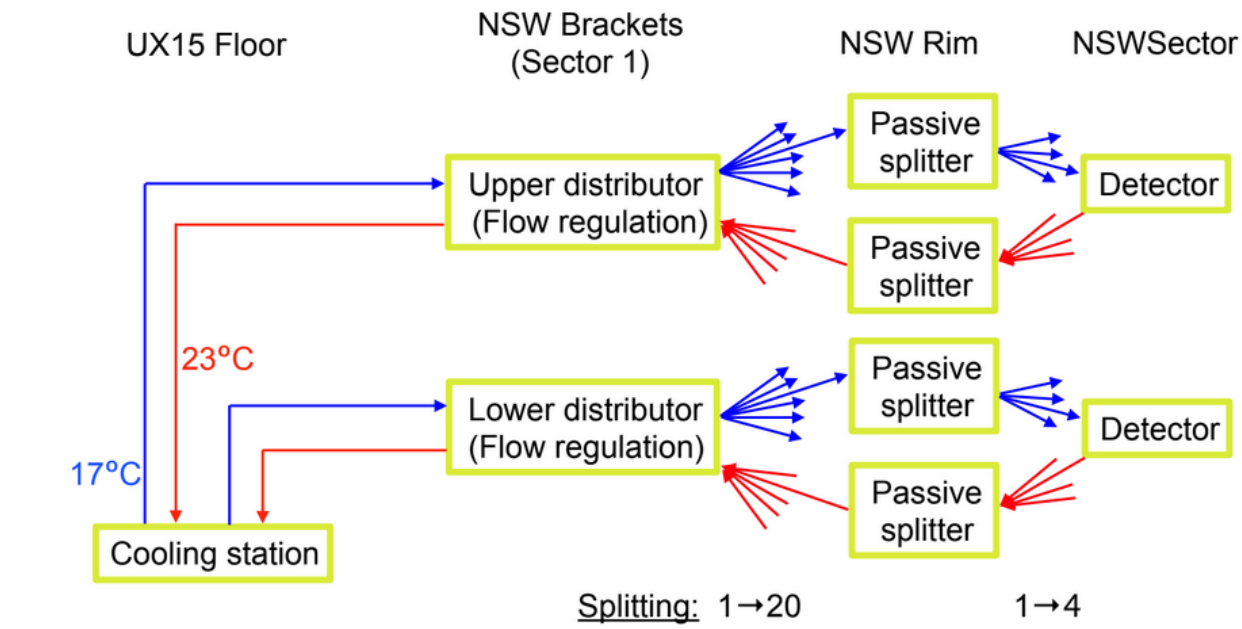

(a)

(b)

Figure 3.4: New Small Wheel Main Cooling Loops.
(a): Cooling Scheme Splitting. [58]
(b): Upper Cooling Loop Topology. [57]

3.3: Gas System

The Gas System of the New Small Wheel uses a mixture of ArCO2 for keeping a stable environment inside the sector. This gas mainly controls the humidity inside the sectors, which should remain as low as possible.

The gas system for the Micromegas utilises 16 channels per wheel with each channel supplying and returning from either the IP or HO side of 2 adjacent sectors. For example, 1 channel feeds the IP side of sectors 2 and 4 which are adjacent small sectors, while another feeds the HO side of sectors 7 and 9, which are adjacent large sectors. All channels complete a loop to either IP or HO side and either small or large sectors.

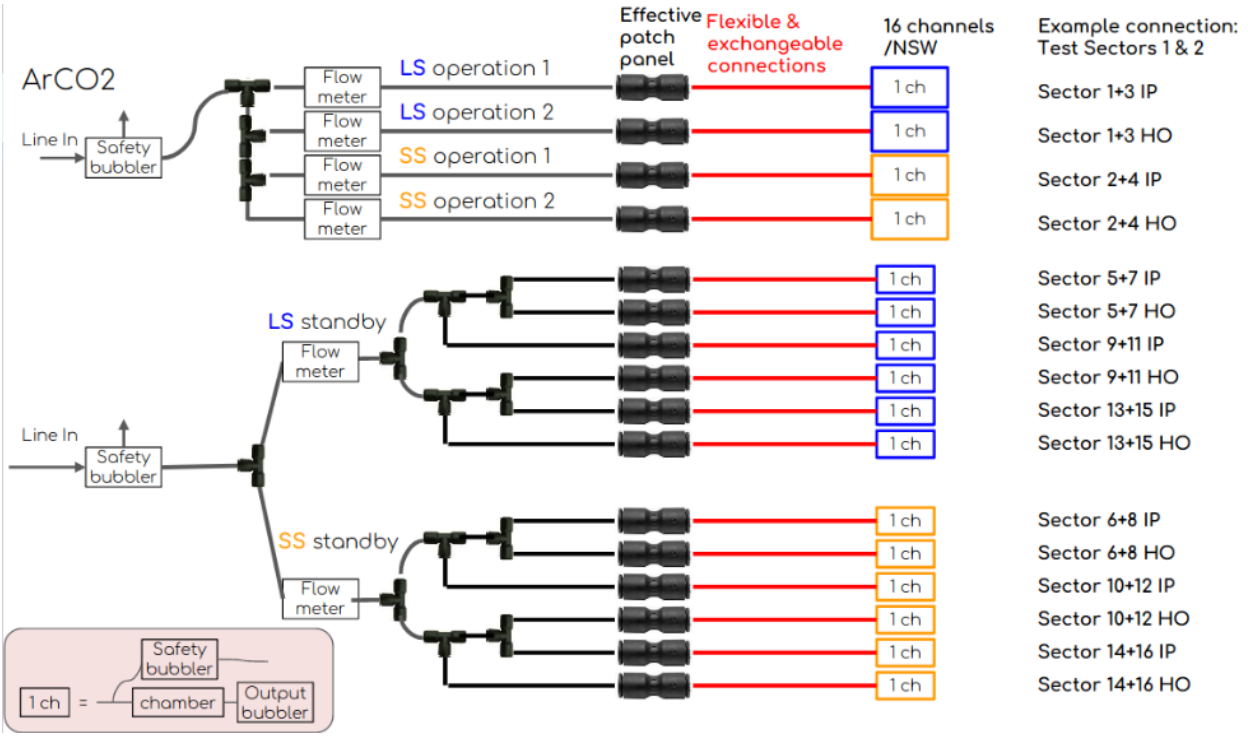

Figure 3.5: The Gas System Scheme of the Micromegas Detectors. [59]

The gas supply system for the Micromegas that was used at the commissioning site comprised a gas mixer, a gas manifold, a gas bracket and the gas pipes that were routed on the wheel and were on hold to be connected with the chambers. The mixer was supplied via pressure-regulating valves with Argon and Carbon Dioxide from tanks outside the building. The output of the mixer 93% Argon and 7% CO2 supplied the gas manifold, where the flow to up to 6 different manifold channels was individually regulated. Of these, 2 channels were standby channels with lower pressure used in a one-to-many setup with the detector gas channels to keep gas flowing through detector channels which were not being tested for leaks or HV stability, the other 4 main channels were used in a one-to-one setup with higher flow through each detector channel. The main channels were used for leak tests, and for keeping the humidity low when applying HV. Each of the manifold supply channels was connected in parallel to a safety bubbler which set a maximum input pressure of approximately 70 mbar relative overpressure in order to indicate a possible flow problem and limit damage to a sector. The return lines for each detector channel were connected in series to a gas bubbler which imposed a 3 mbar relative over-pressure working point on the Micromegas chambers, and in parallel to a second safety bubbler that was regulated at 5 mbar. The

pressure inside the chambers could be measured on the output lines only since a set of impedances was installed on the input lines to ensure a homogeneous gas flow through the chamber volumes [60].

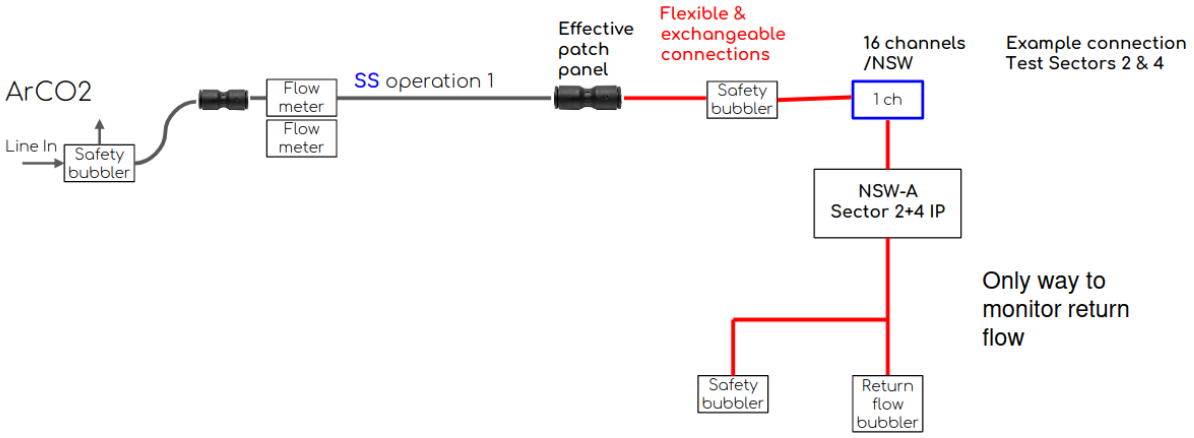

Figure 3.6: Visual Representation of a Single Gas Channel. [59]

3.4 Power Scheme of the New Small Wheel LV

The New Small Wheel LV systems require significant amounts of power. They need around 100kW of electrical power per wheel- ~75% for the MM Detectors and ~25% for the sTGC Detectors. This power comes out from the NGPS Generators which generate 300 VDC. This voltage travels the furthest distance, from the ATLAS Server Room up to the patch panel at Sector 13 and from there it is distributed across ICS power supplies on the Wheel, which provides the 12 VDC needed by the majority of the electronics of the Detectors. From the ICS the power is distributed to the LVDBs which in turn distribute the power among the Digital and Analog electronics of each sector.

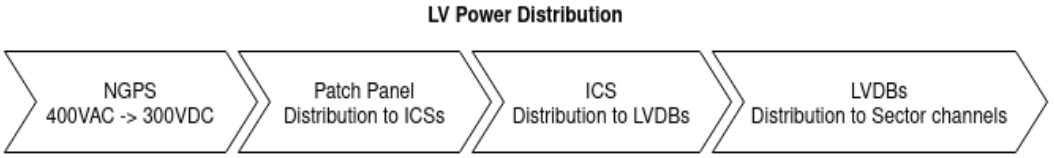

Figure 3.7: Low Voltage Power Stages.

Figure 3.8: NGPS Front View.

On the front side of the NGPS unit are placed: a circuit breaker, a colour graphic display with a navigation switch for the local control of the module, three communication sockets (2 SFPs and one Ethernet port), four status LEDs and one USB device connector. [61]

Figure 3.9: NGPS Rear View.

On the rear side of the unit are placed: a three-phase input connector, an earth connection terminal, output terminals, the D-Sub 15 Female Pin I/O connector and a connector for the voltage remote sensing. [61]

The patch panel has a pair of connectors for each pair of ICS - one “big” and one “small” connector. The “big” connectors are connected as “High Voltage” inputs to the 5 “MM” modules with a cable using a plug on each ICS crate. On the other side, these connectors are connected to the NGPS Generators as inputs.

The ICS modules are controlled by the branch controllers, which are also hosted in the Server Room. Through software (GUI FSM), each NGPS and each ICS channel can be controlled and monitored. The ICS has been designed to work under extreme radiation while its power and control units can be in a safe, radiation-free environment.

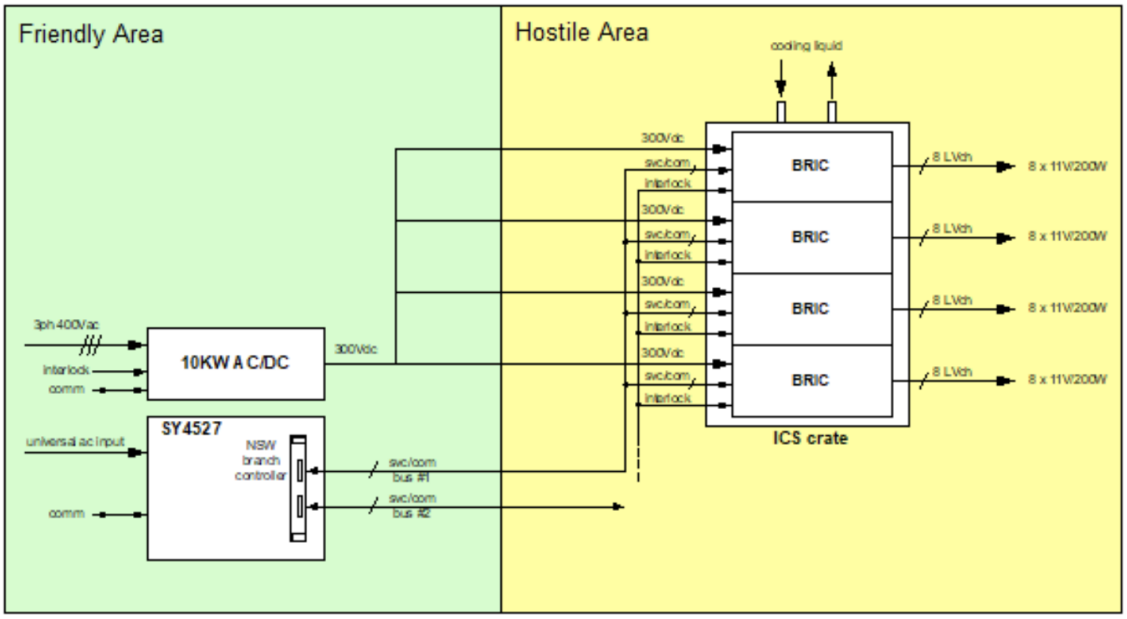

Figure 3.10: ICS Connectivity Chart. [62]

An ICS crate (seen in Figure 3.11) contains 4 modules. Each module is made from the front panel and two power boards (a powerboard can be seen at the bottom of Figure 3.11). Each module has a 300VDC input and 8 10-12VDC programmable outputs. Also, each module has a D-SUB15 terminal for the Branch Controller cable plug for the control and monitoring of each channel. Every pair of sectors - a small and a large - needs one pair of ICSs to work, summing 8 modules and 64 channels per pair. From each pair of ICS crates, 5 modules are used to power up the MM Detectors of one pair of sectors and the rest 3 modules are used by the sTGC Detectors. Those channels are then distributed to the LVDBs.

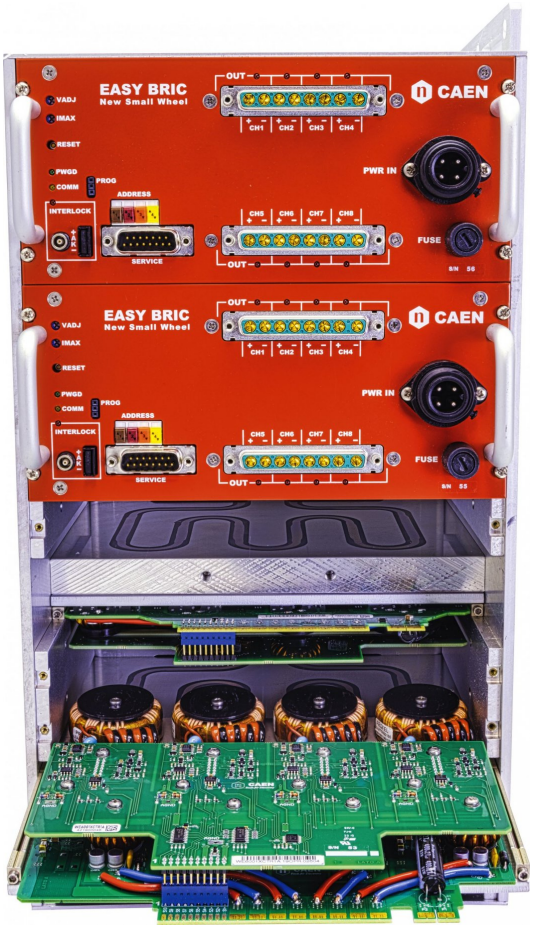

Figure 3.11: ICS Crate. [63]

An LVDB (seen in Figure 3.12) is split into two parts, the left part that distributes power to the Analog cards of the Detector with 8 outputs and the part that distributes power to the Digital cards of the detector on the right with 4 outputs, so that electronic interference to the front-ends can be cut-off. Each LVDB board is responsible for distributing the Low Voltage power to two half-layers, meaning 2 layers of 4 PCBs. Each MM Detector requires 16 LVDBs of which only 8 use both the Digital and Analog parts. In total there are 20 channels for each sector's MM detectors, regardless if it is large or small, summing up to 40 channels in total. For any sector, 16 channels are used for the Analog Cards and 4 channels are used for the Digital Cards which are split to 8. This is done because a single Digital LVDB draws little power. As mentioned above the residual 24 channels are reserved by the sTGCs.

Figure 3.12: The LVDB.

3.5 Fibre Infrastructure - MicroMegas

One of the most vital services of the New Small Wheel is the Fibre infrastructure, passing through vast amounts of data to end from the front-end electronics and Felix Servers. In normal operation of the Detector when an L1 accept signal is sent, data is transferred through the L1DDCs to the Felix Servers. In Figure 3.13 the MM and sTGC Fibre Infrastructure is illustrated. In this section, we will only describe the MicroMegas Fibre Infrastructure**.**

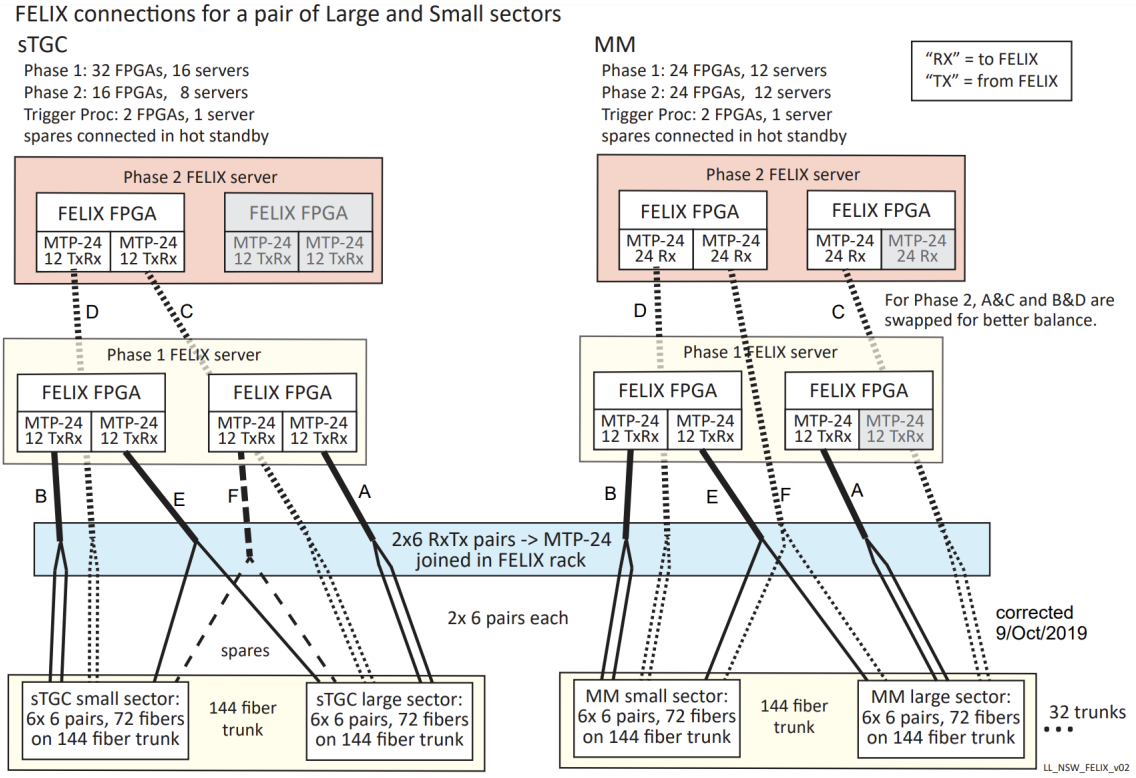

Figure 3.13: Felix - NSW Communication Fibre Infrastructure.

Each MM Sector has 16 L1DDCs and 16 ADDCs. The L1DDC provides 2 pairs of fibres, labelled as LTX and LTT. LTX fibres are used for the Phase-1 upgrade for the NSW and the LTT fibres will be used in the future Phase-2 upgrade of the Wheel. The ADDC provides one fibre pair of two one-way paths to the MM trigger processor. This means that the MM sector uses 48 fibre pairs. These pairs are split into three separate Small Fibre Boxes (SFB). These SFBs contain 3 of Fibernet's MTP12 to LC Star Modules.

Figure 3.14: The Fibernet MTP12 to LC Star Module. [64]

This means that each SFB can host 18 fibre pairs, leaving 2 pairs as spare. The fibres are split in this way: Lowering Side Readout Fibres, Rising Side Readout Fibres and ADDC trigger Fibres (from both sides). Each L1DDC and ADDC uses LC fibres of a specified length, depending on its position

on the Double Wedge. This is due to the timing of the NSW electronics needing to be very precise and it is crucial to know the exact time it takes for data to go from one point to another since we have to track phenomena that happen at the speed of light.

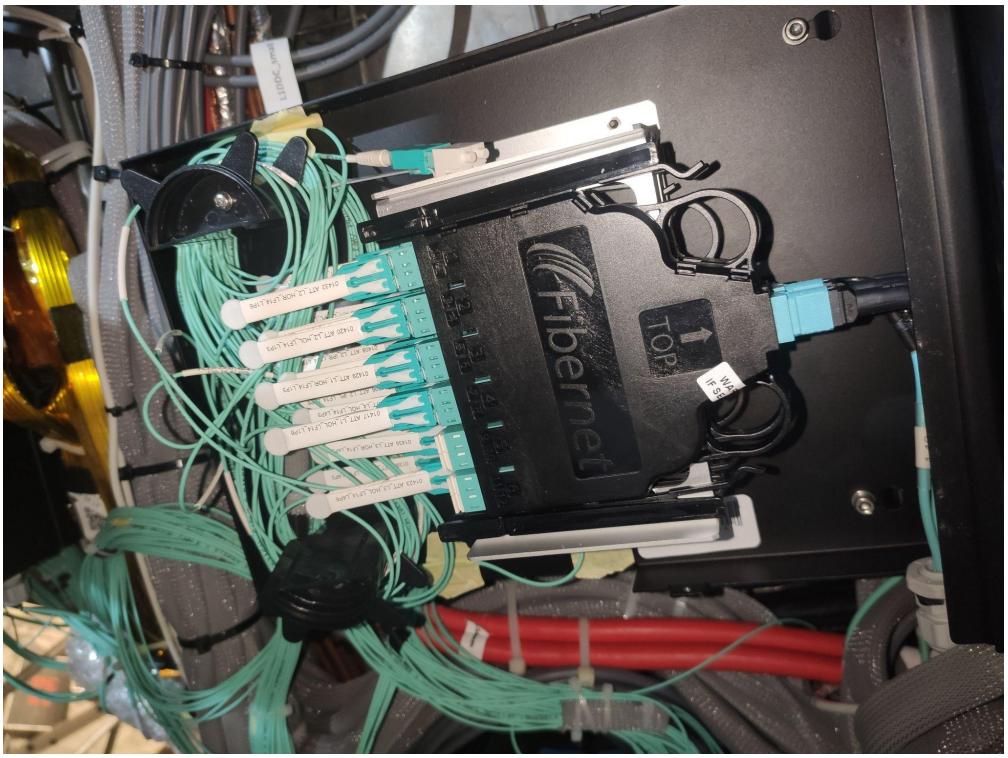

Figure 3.15: Example of an SFB consisting of 3 Star Modules one on top of the other.

A 3xMTP12 to MTP36 cable comes out from every SFB and is led to the Large Fibre Box (LFB). This means each MM sector uses three MTP36 cables, one for the readout of the rising side, one for the readout of the lowering side, and one for the trigger for the whole sector. Each Wheel uses two LFBs for both MM and sTGC Detectors. Each LFB hosts half of the MM Detectors and half of the sTGC Detectors. The LFB is simply made of MTP couplers and its objective is to group all the fibres of the NSW to two single points, from which another set of fibre cables is used to connect the Wheels to the corresponding Felix machines and Trigger Processors. This prevents difficult fibre replacements in case of damage (splits the problem into two smaller problems) and made the installation of the NSWs from B191 to Point 1 more practical since the Trigger and Readout Fibres didn't have to be rerouted upon installation from either side. When the NSWs were in their final position, it was only a matter of connecting the Fibre Bundles coming from the Server Room through the flexible chain, to the LFB directly.

Figure 3.16: The Large Fibre Box.

4: Commissioning Workflow and Sector Validation

For the assembly of the New Small Wheel, Micromegas wedges were transferred from building BB5 to building 191. In BB5 the Micromegas wedges were put together, all the electronics were installed and some preliminary checks like LV HV and Readout were done. In 191, as soon as the wedges arrived they would be put in "parking". There, they were tested in several aspects.

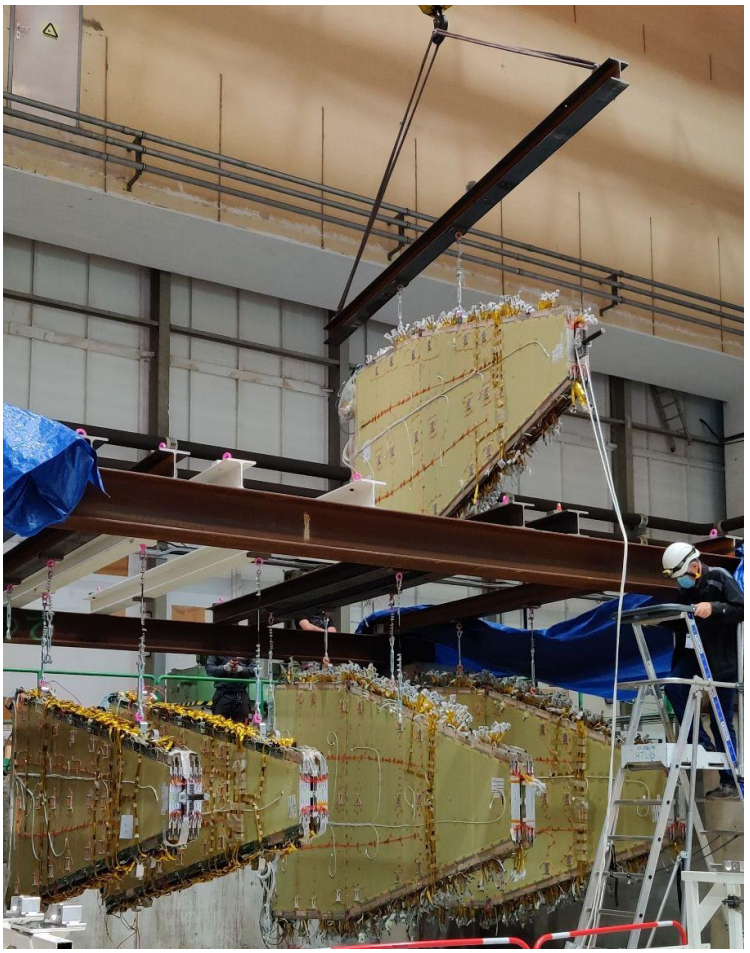

Figure 4.1: Arrival of MicroMegas sector in "parking".

4.1 Commissioning Workflow

Starting from the "table" tests where the LV extension cables were checked for polarity, continuity and labelling. Then these cables would be installed on the detectors.

After the table tests were the "balcony" tests. These tests started with the T-sensor checks. These checks would have to take place before the sTGC installation since after that point, any problematic T-sensor wouldn't be replaceable. All T-sensors would be tested for impedance and if any problem would be found, either the connector or the sensor itself would be replaced. Fibres were then checked visually for any obvious strips, in which case they would be replaced or fixed, depending on the damage.

After checking the fibres, High Voltage REDEL connectors were checked for possibly missing parts since during transportation they could be damaged. Then there were the grounding checks and specifically the impedance between MM wedges and the Spacer Frame and also

between each MM wedge. In addition, after sTGC installation, the impedance between MM and sTGC wedges was also checked.

The last test in this category was the presence of the external impedances of the gas pipes. In parallel with the balcony tests, there were three preliminary on-wheel tests. The first one was checking whether the fibre boxes and their corresponding fibre cables were in place. The second test was checking that all the cables from the corresponding ICS module were properly mapped and their polarity was correct. The last one was the polarity, continuity and voltage of the NGPS module, which provides 300V to the ICS.

Following the preliminary checks, the detector would be installed on the wheel by the service team and then the impedance between the sTGC and MM detectors would be checked again. If it was too low (below 2 kOhm) that would mean that there are unwanted connections between them, such as copper gas pipes or shorted cables. Then, the MM detectors and the JD, which is the NSW frame, would have to be isolated. If not, the issue would be investigated and mitigated. When such problems would be resolved, the detectors would be connected to the NSW ground.

With all these checks done, all connections would be made. Starting from the fibre connections, followed by the NGPS to ICS connections and then there were the LV connections - connecting each LVDB with its corresponding ICS channel. Following, there would be the High Voltage connections, right after the splitter boxes were configured, and the REDEL connectors from the power supply side would be tested. Then, cooling, gas and T-sensors would be the final connections to be made.

Since all connections are done, on-wheel testing starts. The first test would be to make sure that the cooling has no leaks or air pockets and that the flow is sufficient to cool down the electronics and the power supplies (ICSs). This could need more adjustments after any sector was turned on and it was decided by monitoring the temperatures of the sector's and ICS's electronics. With the cooling checks done, the electronics commissioning could now start. First of all, there was the LVDB channel checking which was signalling whether there was any faulty channel and if so, an investigation would be done to see if it was a connector or an LVDB or FE fault.

After validating that all the electronics are properly powered, the communication part of the detector would have to be commissioned. The fibre links from the L1DDCs to the FELIX would be the first thing to validate. If both Tx and Rx paths had light continuity and the optical power was above a certain threshold, then the link would be considered okay. But, if it was not okay, the faulty part would have to be pointed out, for example, if it was the LC fibre from the L1DDC to the splitter box or from that point towards the FELIX, and then it would be replaced or a spare pair would be used.

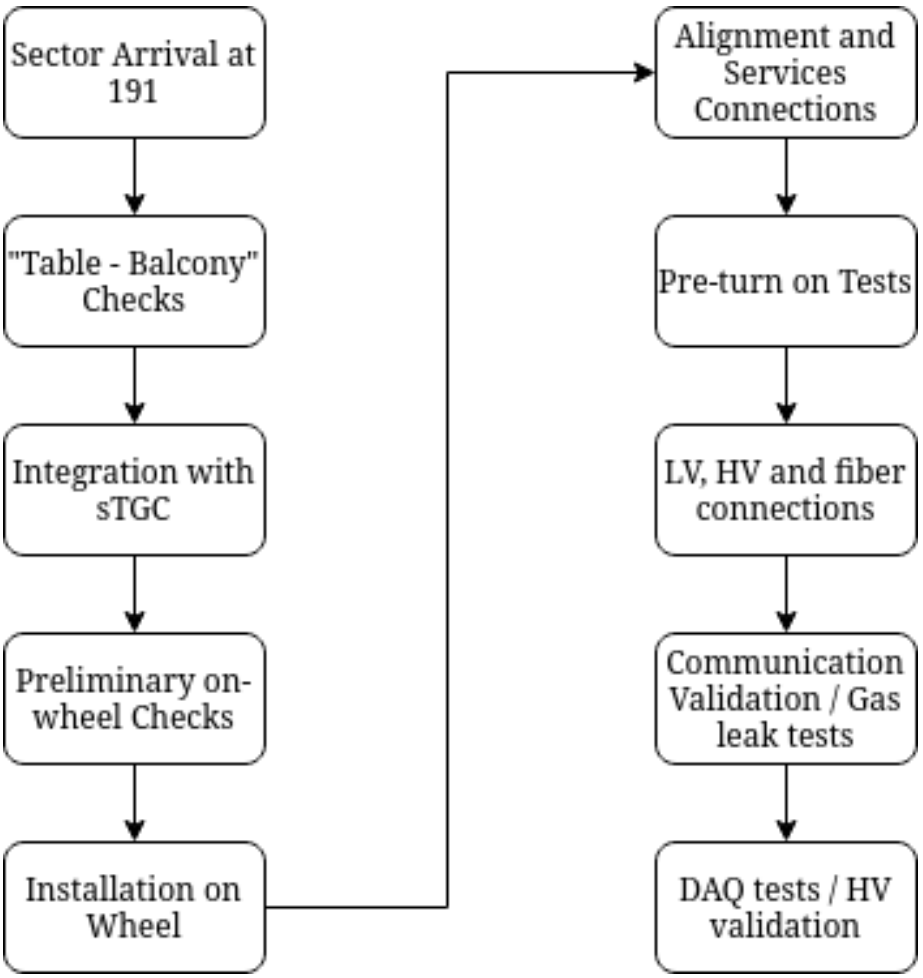

Figure 4.2: Commissioning workflow.

The next part would be the communication between the L1DDC and the MMFE8s which is done electrically and not optically. For the test, the L1DDCs would be configured to communicate with the FELIX. Then the OPC server script would be run to see if communication with all the FEs could be established. If not, the faulty channel would be reported by the script and then it could be investigated which would usually mean that there was a loose connection to be secured or less commonly, the twinax cable would have to be replaced. When every part of the communication was operating properly, the noise and data acquisition (DAQ) tests could start.

In parallel, the gas leak tests would start to determine the leak rate of the detector. If it was in accordance with the BB5 results then the corresponding detector would be considered validated in terms of gas. Then it would be flushed with ArCo2 to make sure the humidity is as low as possible so that the High Voltage validation could start. This procedure would take at least 24 hours and when all PCBs would reach the highest possible voltage with an acceptable spark rate, then the detector would be considered validated in terms of HV. In certain cases, some PCBs would be very unstable so the whole PCB would remain unpowered to ensure the stability of the detector.

Since the detector works properly and passed all the previous checks, the next thing to do is to start validating the sector's idle noise levels, hit on track efficiency, and the number of dead channels on each layer.

4.2 Noise studies - DAQ

The noise and DAQ tests are the first activities in the commissioning workflow where the status of each MM sector's layer is studied to be classified as operational or requiring actions to be taken to obtain the highest efficiency possible. It is worth mentioning that the noise tests concern 8192 readout channels per MM layer or 65535 readout channels for each MM sector (Subsection 1.4.3).

There are four types of tests described in the following paragraphs performed in this order;

A. The "baseline runs" that identify the noise level of each readout channel
B. The "trimmers runs" where successive baseline runs are performed to set the noise threshold of each readout channel,
C. The "noise runs" that validate the readout channels after applying their noise threshold and
D. The "pulse runs" used to calibrate the readout channels and the trigger path.

4.2.1 Baselines

The first test was the baselines test. The baseline runs were used to classify the Readout channels into 4 categories: normal channels, noisy channels, not connected and dead channels. A baseline run measures the noise level of every channel many times (samples) to identify the electronic noise of each resistive strip. In our case, 200 samples per channel were collected in order to have a sufficient amount of samples for a whole sector, while the duration of the test was less than 15 minutes (each sampling takes 10 minutes and the post-processing 5 minutes). The sampling takes this long since for the baseline runs each VMM channel is read out continuously through the Slow Control Adapter (SCA).

The VMMs take a number of samples as mentioned above for each channel (strip) in ADC values which are then translated to mVolts. A baseline run expressed in mV is illustrated in Figure 4.3. The colouring of the graph labelled as entries refer to the number of samples having the same value.

$$Mean(mV) = \mu = \frac{\sum_{i=1}^{N} \chi_i}{N} \tag{4.1}$$

$$RMS(mV) = \sigma = \sqrt{\frac{\sum_{i=1}^{N} (x_i - \mu)^2}{N}} \tag{4.2}$$

To better understand the noise levels of the sector we need to present the given data in a different manner. For this reason, we present the noise levels in Electron Noise Charge (ENC). The RMS ENC is calculated by dividing the RMS in mVolts by the Gain setting of the VMM's amplifier. This unit conversion provides a better visual representation of the standard deviation of the noise around its mean value:

$$RMS\ ENC = \frac{RMS(mV)}{G(\frac{mV}{fC})} = (\frac{RMS}{9} \times 6240)e^{-} \tag{4.3}$$

A baseline run expressed in ENC for each readout channel of one layer is illustrated in Figure 4.4.

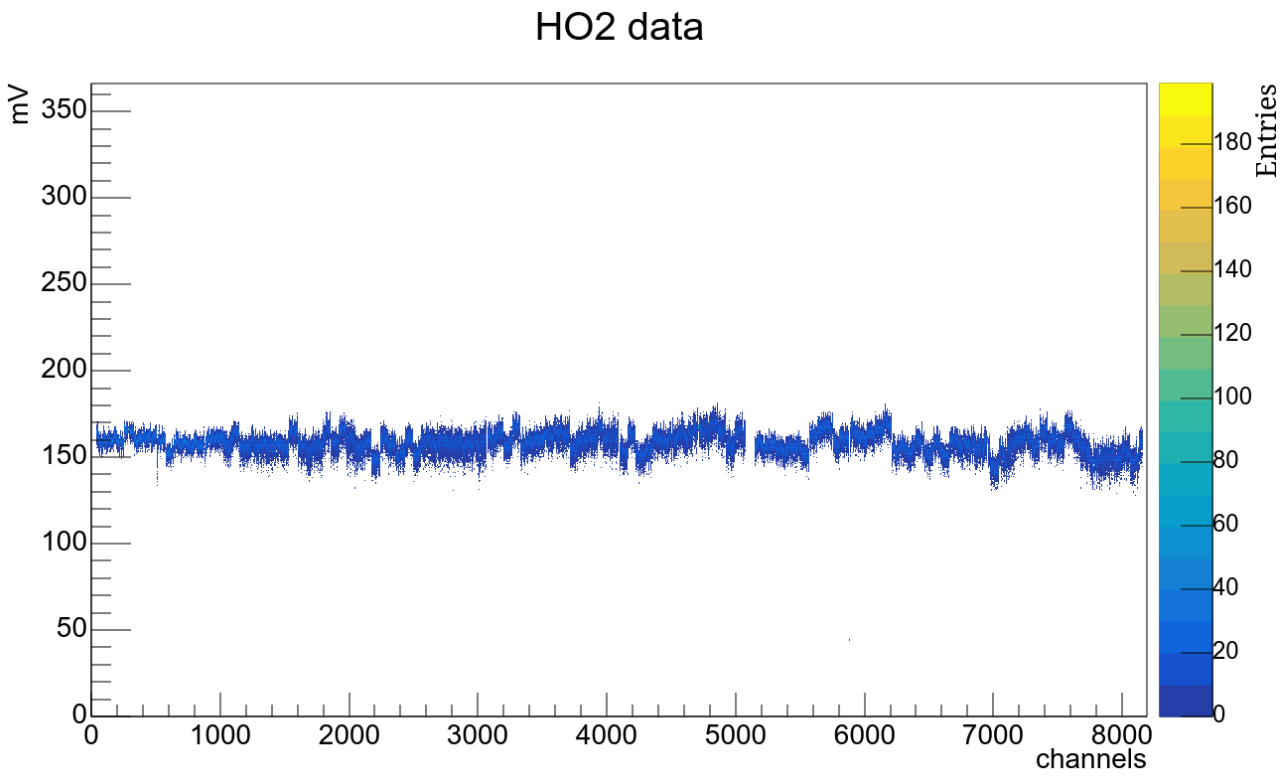

Figure 4.3: The values of the noise in mV across 1 out of the 8 layers of a single sector.

Based on the distribution of the noise values, in ENC, upper and lower thresholds defining the aforementioned categories are set for each PCB separately. This classification can be easily seen in Figure 4.4 by observing the red lines which represent the classification thresholds and the purple dots that each one corresponds uniquely to a sample. For each PCB, any point above its upper red line is considered noisy and respectively any point below the lower red line is regarded as a dead channel. The points that are between the two lines are the normal channels.

There are also a number of electronic channels that are not connected to any strips, as the geometry of the detector makes it impossible for some of its parts to have strips. An example of these channels can be seen in Figure 4.5. It can be noticed that as the strip number increases, there is also a trend for the noise to increase. This is because as the strip number increases the length of the strip also increases, and as a result, it picks up more noise, as it can be understood in antennae terms.

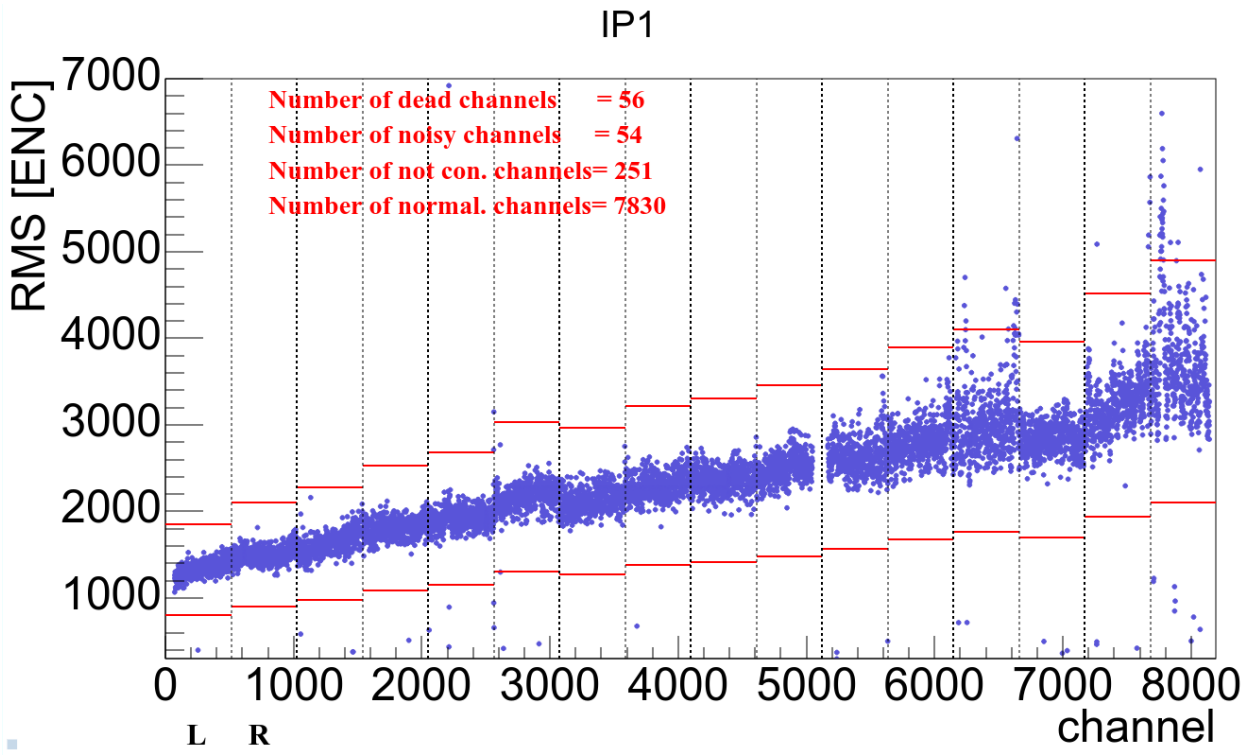

Figure 4.4: Baseline diagram.

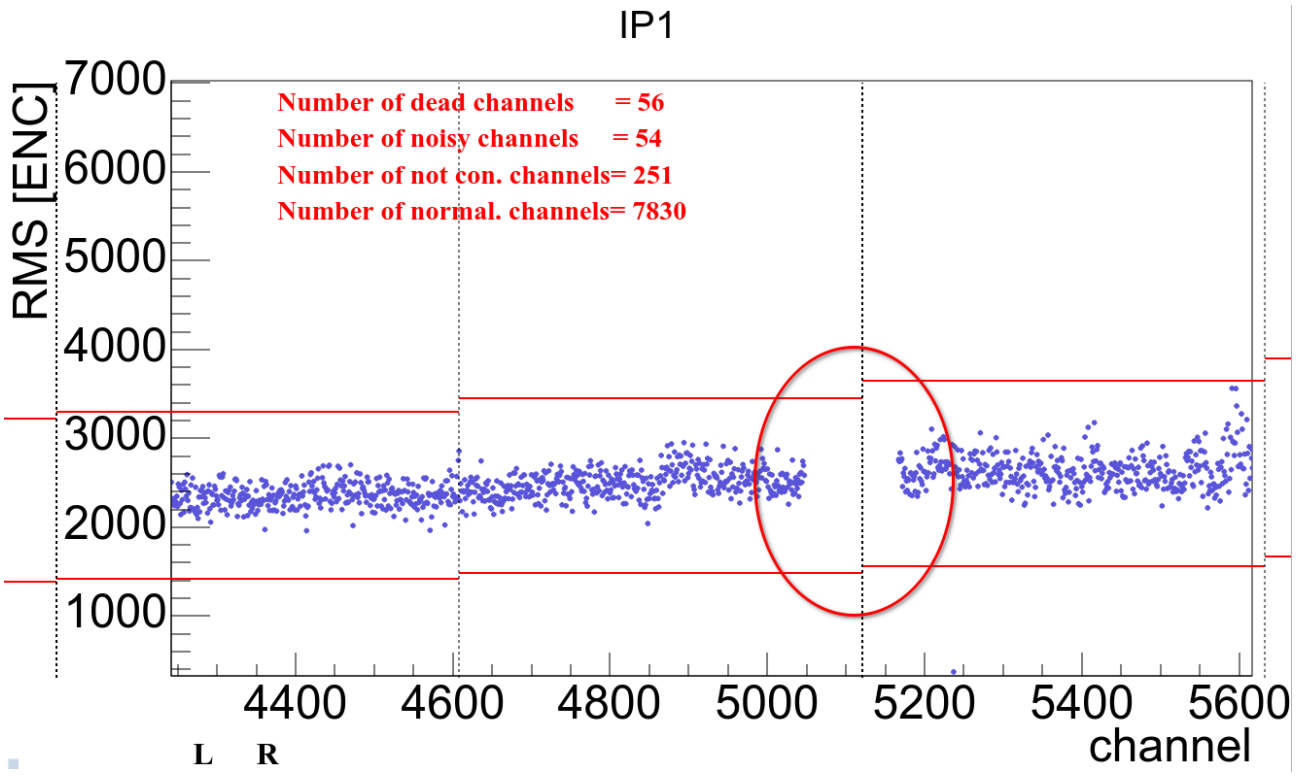

Figure 4.5: An example of not connected channels.

For a better perspective, in Figure 4.6 there's a side-to-side comparison between a baseline (ENC graph) and a normal mVolt graph. It is really interesting how a conversion of the units from mVolts to ENC makes a huge visual difference. The standard deviation around the mean value is visible also in the RMS in such a bad case like this but (orange regions) the baseline graph makes it

crystal clear to observe and has more sensitivity in its units. In the region highlighted by the green mark you can see that when the standard deviation is lower the RMS ENC value is also much lower.

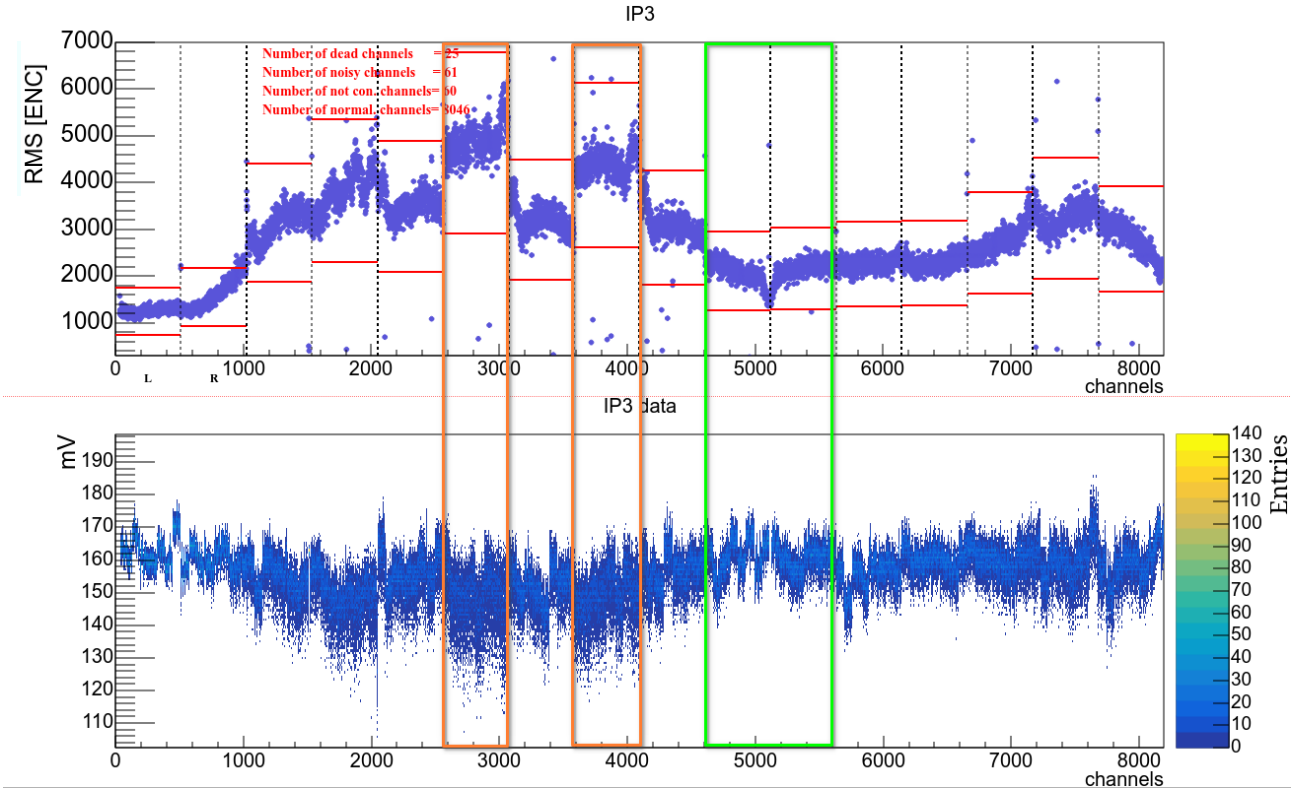

Figure 4.6: Comparison of a baseline graph expressed in ENC (top) and in mV (bottom).

For further understanding of the baseline graph pay attention to the fact that it is divided into regions separated by vertical dotted lines. These regions indicate whether we observe a Rising [R] or Lowering [L] side of each PCB. The distinction between which region corresponds to the Rising or the Lowering side is marked just below the two first regions. In baseline figures, under the first region, there's an L meaning that this is the Lowering side of PCB1 while the second region is indicated with an R standing for the Rising side of the same PCB. The same logic is implied for every pair of columns respectively. Each pair is matched with a PCB while the PCB number increases by one for every next pair of regions. Note that the L and R regions aren't always shown in that order. Half of the graphs start with L as the first region while the other half starts with an R, so pay attention to that when looking at a baseline graph. Said information can be correlated with the Sector layout described in Subsection 1.4.3

Concerning the baseline runs, it is worth mentioning the use of the difference graph. That graph is used when there's the need to compare two baseline plots, setting one of them as the reference run and the other as the graph we want to compare to it. Take the following case as an example. A reference run before a modification on the sector is selected. Then a modification is performed and we use the difference analysis to observe the effects of said modification.

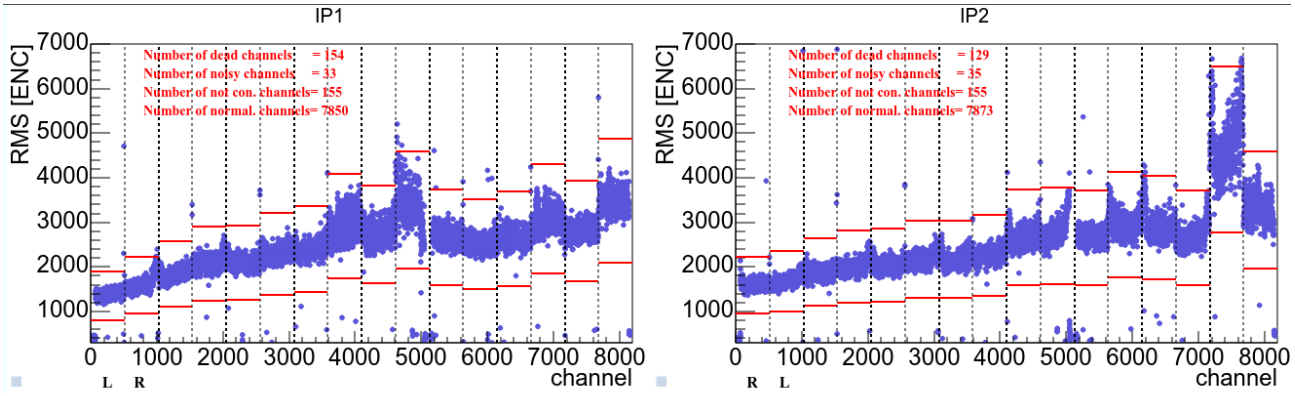

Figure 4.7: The reference run.

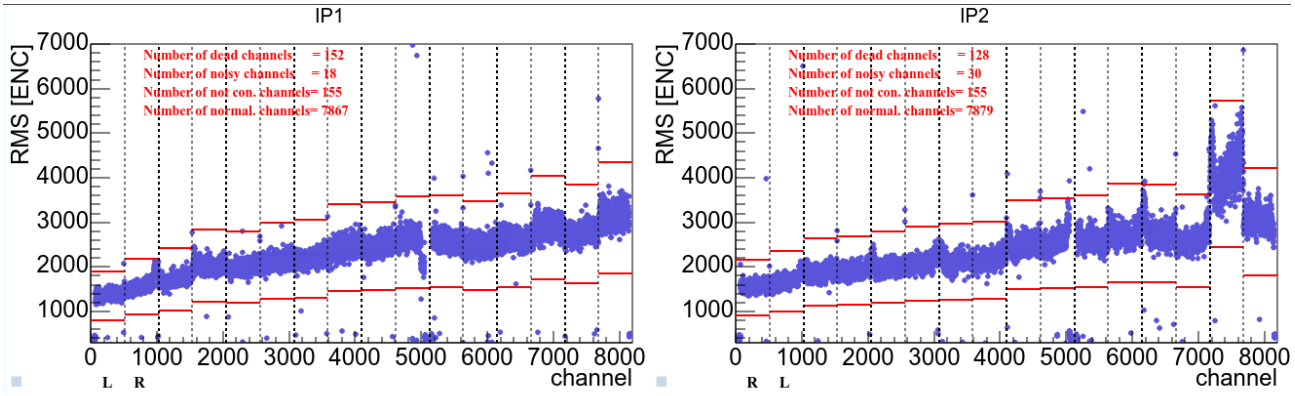

Figure 4.8: The comparison run.

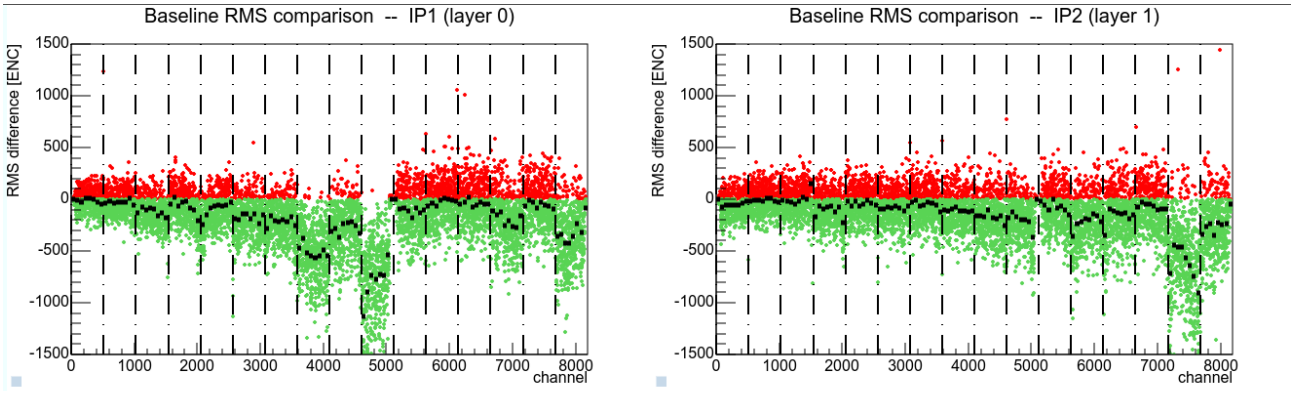

Figure 4.9: The difference graph between the runs.

This graph is basically the result of the subtraction of the baseline we want to compare to the reference graph. The red region describes the deviation of the channels where the reference run had lower noise and the green region the deviation of the samples where the reference run had higher noise. The dark points are the average of this operation. As it can be understood where this line is below 0 the modification has a beneficial effect and where this line is above 0 the modification has a detrimental effect. It can be observed that this way the differences in noise are very easy to pinpoint. This helps draw conclusions on modifications and makes a visual representation of the effects of these modifications clearer in a *"green good, red bad"* manner.

4.2.2 Trimmers

The second test is the "trimmers" run - also called thresholding. This test has the purpose of balancing the noise levels of all the VMMs of an MMFE8 by adjusting the gain of each VMM. This is done by taking successive baseline runs in order to validate the accuracy of the trimming process in multiple turns.

In detail the process starts by taking a normal baseline (seen in black in Figure 4.10) and then by setting the threshold initially to the mean noise value of each VMM plus an arbitrary of 9 to 12 times the RMS value of the noise of each VMM. This is called the untrimmed threshold and it can be seen as the blue points in Figure 4.10 where we see the calculated threshold of a single MMFE8.

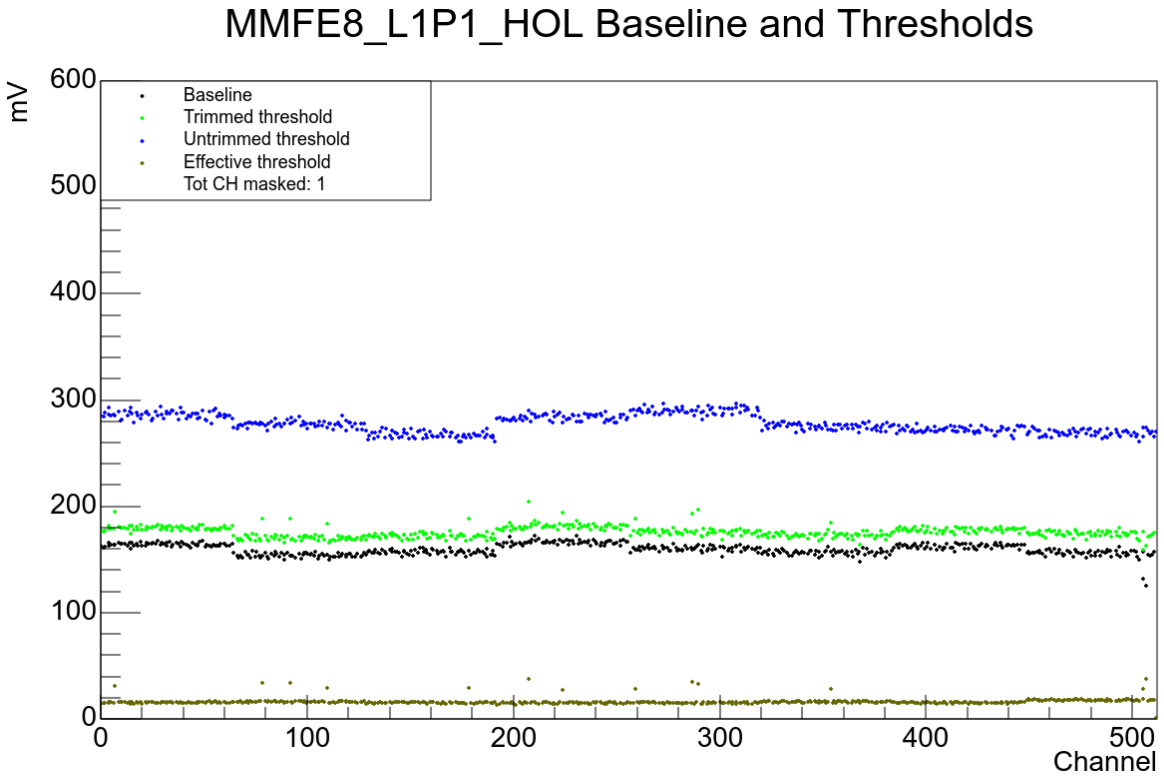

Figure 4.10: A thresholds diagram.

This can then be fine-tuned with the so-called trimming. Each strip can be trimmed by up to 30 out of a total of 1024 ADC counts. This trimming process can only decrease the threshold of a single strip. The goal of this process is to balance all the strips to be on the same level in the best way possible. The result of this process can be seen in Figure 4.10 as the trimmed threshold, coloured green. Then the effective threshold is calculated by subtracting the trimmed threshold from the baseline. It is represented by the olive-coloured dots.

Some strips though are too noisy and cannot be trimmed to fit this requirement. In this case, these strips are excluded from the process in order to maintain the rest of the channels of such a VMM operational. These channels can be masked by the procedure described in the next subsection.

As a result, the trimmers optimise the threshold of each channel in the most specialised manner since it takes into account each channel's true condition and sets the best possible threshold using this information.

4.2.3 Noise Runs

The third test called the noise runs are performed to validate which channels (strips) would have to be masked which means such channels would not be taken into consideration when trying to take real data. The noise run also validates the high rate communication electronics which will be used at the HL-LHC, such as the Read-Out Controller (ROC).

After applying the thresholds for each channel, a very high number of random triggers - spanning from hundreds of thousands to millions - are performed and the VMMs outputs are readout through the MM readout path on each layer individually. The random trigger causes an event also referred to as a sample. Ideally, the channels are expected to have no hits. The number of hits/event/channel is calculated and plotted.

These channels are sorted from the least eventful channel to the most eventful channel. Having the channels sorted in this way we start summing them in that particular order. When or if the number of hit/layer/event value exceeds 2 then the rest of the sorted channels are masked out as noisy. The number of 2 hits/layer/event was selected through trials and it was found to mask the channels that the trimmers could not filter and as a result not trigger the Data Acquisition system just for a small number of noisy channels. You can see the masking point in Figure 4.11 thinking of an imaginary straight line parallel to the x-axis which divides the graph in two regions.

This masking point can differ from layer to layer as it can be understood from the way the noisy channels are masked. Any channel over that imaginary line is masked out as noisy and marked red while every other channel below this line is marked blue and is not considered noisy, though some of them could be dead channels that cannot be identified using the noise runs and they can be found only by the baseline runs.

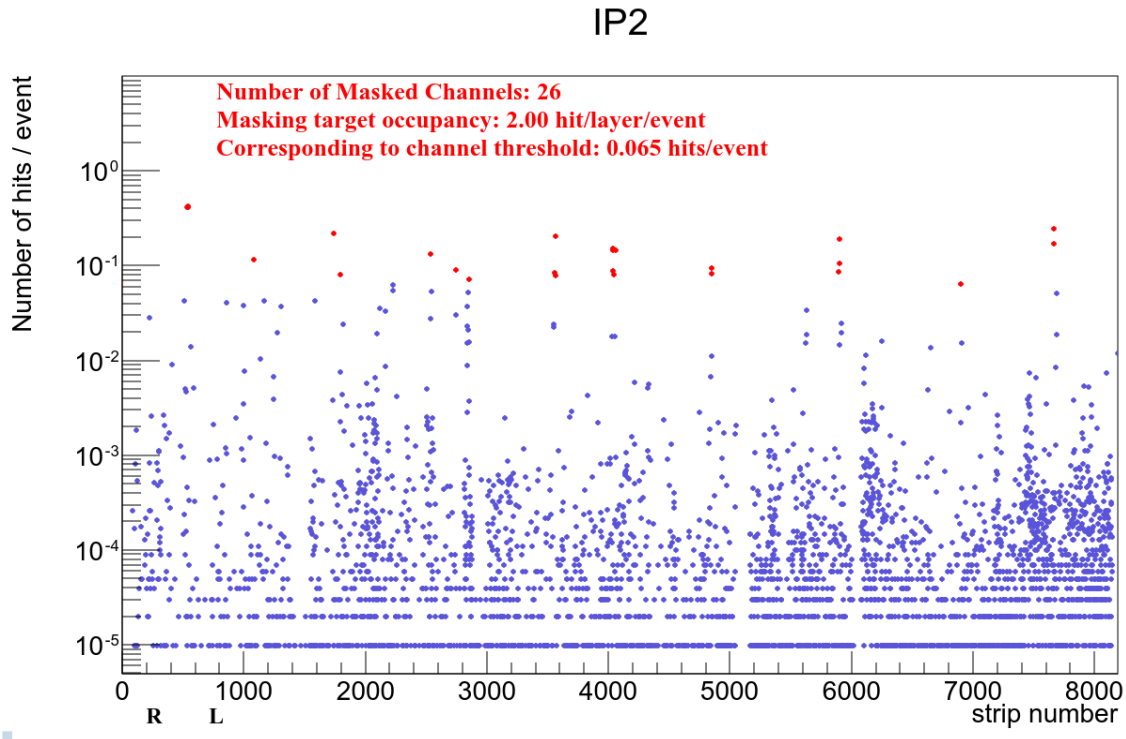

Figure 4.11: A noise run diagram of C11 IP2.

The cumulative distribution in Figure 4.12 describes the procedure we mentioned above. The horizontal line is set to 2 on the Y-axis. The vertical line can land on a different point of the distribution depending on the noise profile of a single layer.

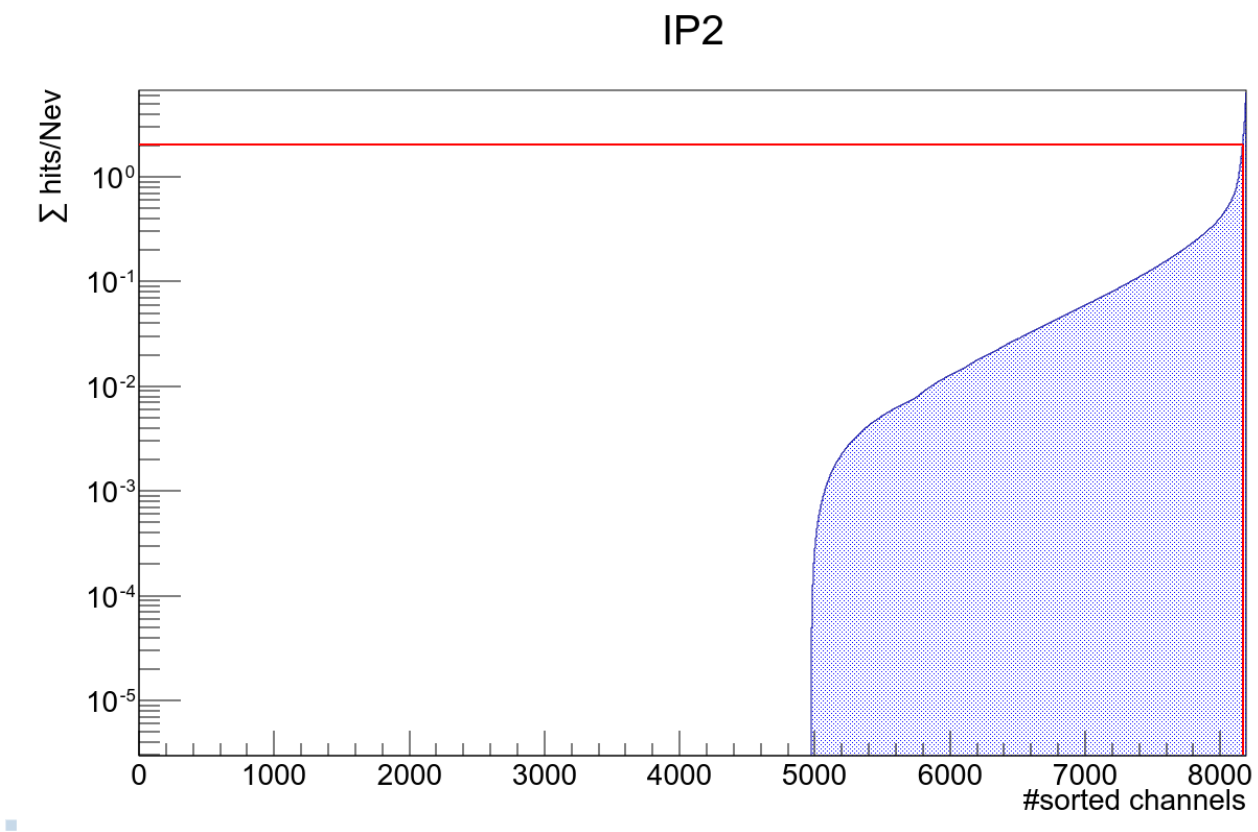

Figure 4.12: Cumulative distribution of channels having specific hits/number of events on layer IP2 of sector C11.

4.2.4 Pulse Runs

The final test is the pulse run. The pulse runs are used to calibrate the readout channels and validate the trigger path. A predefined number of test pulses is sent to all the front ends of all MM layers simultaneously. All those pulses should be identically read out by the VMMs, thus each channel has to have the same hit occupancy. The occupancy defines the number of hits divided by the number of pulses sent. So this number is always ≤1. Ideally, it's 1 across all strips.

The actual calibration process would involve a few different heightened pulses - let's say 5 - to be sent to the readout channels so we would know their response on them. This whole process wasn't implemented though during the commissioning and is work left for the future.

In Figure 4.13 there is a typical pulse run test output where one can see that most of the channels' occupancy is very close to 1 except for a few channels which can be classified as underperforming or dead. In this Figure, the channels are labelled as strips. As explained in Chapter 1.4.3, strips are the physical strips of the MM detector and channels correspond to the analog readout channels of the Front-End electronics. There is a 1:1 correspondence between these two terms.

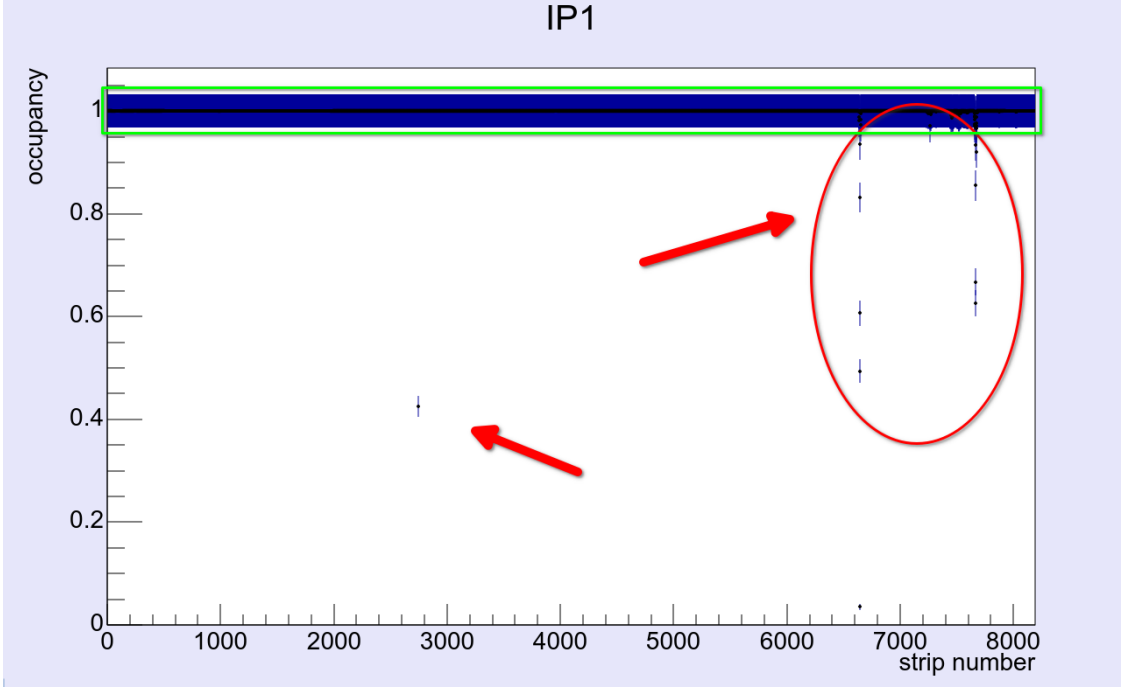

Figure 4.13: Pulse run diagram describing the occupancy of a single layer of a single sector.

Inside the green rectangle are the channels considered good as their occupancy is really close to 1. The red arrows indicate the bad channels.

The reason that we observe only a few bad channels while on the baseline runs the dead channels appear to be many more is because we just compare two different things. Pulse runs, as stated above, validate the calibration of the electronics of the readout channels while the baselines also involve the actual strips of the detector in their run.

During commissioning, when there was a concentrated cluster of dead channels, the commissioning team would check if any twin-ax connector was loose. If there was no problem with these connections at all, these channels would be considered non-fixable.

After all of the described tests were successful the Sector would be considered fully commissioned and this procedure would be repeated for every single Sector. This was rarely the case, as most Sectors would have a lot of troubleshooting involved, explained extensively in the next Chapter.

5: Troubleshooting

In this chapter several issues of the NSW detector will be described, and what steps were taken to mitigate them. Please note that most of the issues were present during the NSW A commissioning and for this reason, all the examples focus on its sectors.

5.1 Noise Related Problems

One of the most prominent issues has been the noise levels across the MM detectors. The noise problems were found to be caused by two main causes. The grounding issues and the Noise coming from the ICS power supplies. Here is a demonstration of how these problems were discovered and what approaches and methodologies were applied to decrease the very high level of noise that appeared on the detectors.

5.1.1 Grounding Issues

The MM wedges were fabricated in many parts of the world and from many different teams. With that said, it is safe to suggest that not all of them were made the same, even though they have been built with the same specifications. Fabrication tolerances and micro-damages in transport caused many sectors to have different behaviour in terms of noise than other sectors. It was discovered that many sectors had minor cracks on the ground plain, causing them to have insufficient grounding. To repair this kind of damage was impossible, given the timeframe in which this issue was found. So a solution was found that could be applied, even when the sectors were already on the wheel, which was the case for wheel A.

As stated in Chapter 4, the main tool for deciding the noise profile of a sector is the baseline graph. With that being stated let's demonstrate how the baseline graphs are presented in this subsection for checking how each modification affected the noise levels of each sector:

A full sector baseline is presented in two quadruplets. In the case of a full sector baseline, the top quadrant shows the IP layers and the bottom quadrant shows the HO layers. In some cases the Difference baseline graph is used to have a close look on the differences of the noise levels using in all cases the older sector configuration - the one before the modification happened - so the graphs that are presented always show the impact of the modification on the noise levels compared to the previous configuration.

Let's take Sector 10 from side A wheel as case study. Sector 10 is selected since its commissioning stumbled upon many of the noise problems that generally appeared.

Starting with the reference baseline run in 191 building after the sector is fully assembled - meaning that sTGC wedges are placed on top of the Micromegas ones and all the connections are made - and the HV part of the sector is powered on, one can see that there are serious noise problems in some layers such as IP3 and IP4 without that implying that there is no room for improvement on the general noise profile for the whole sector. So, the initial Sector 10 noise profile on the wheel is illustrated in Figure 5.1.

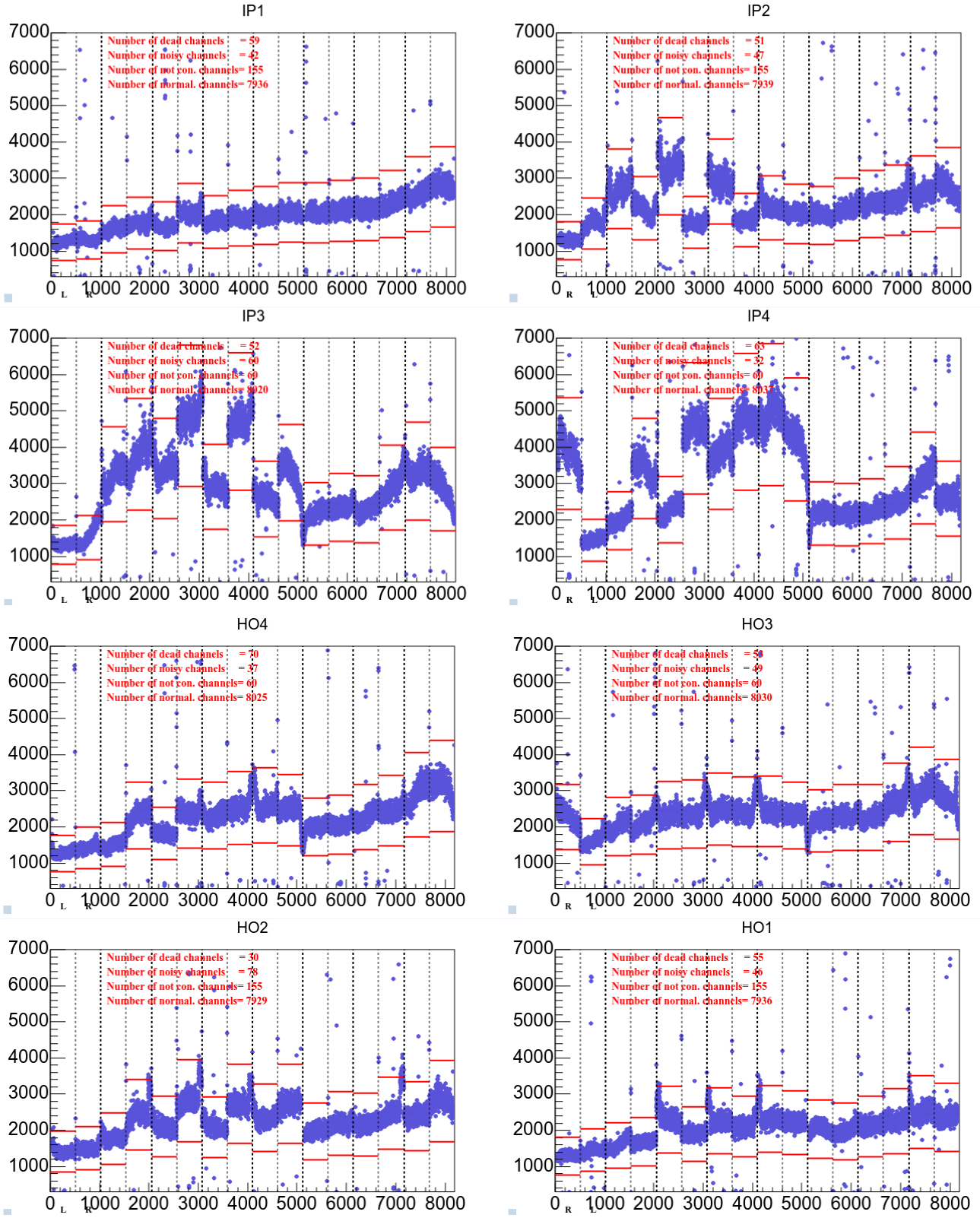

Figure 5.1: Sector A10 initial noise levels. Vertical units are ENC, horizontal units are channel numbers.

The goal was to make all layers have very low levels of noise, similar to what the noise levels were before the MM wedges left the BB5 building where their integration phase took place. The sectors were baselined also during the integration phase so the commissioning team had available data on that and they are demonstrated in Figure 5.2:

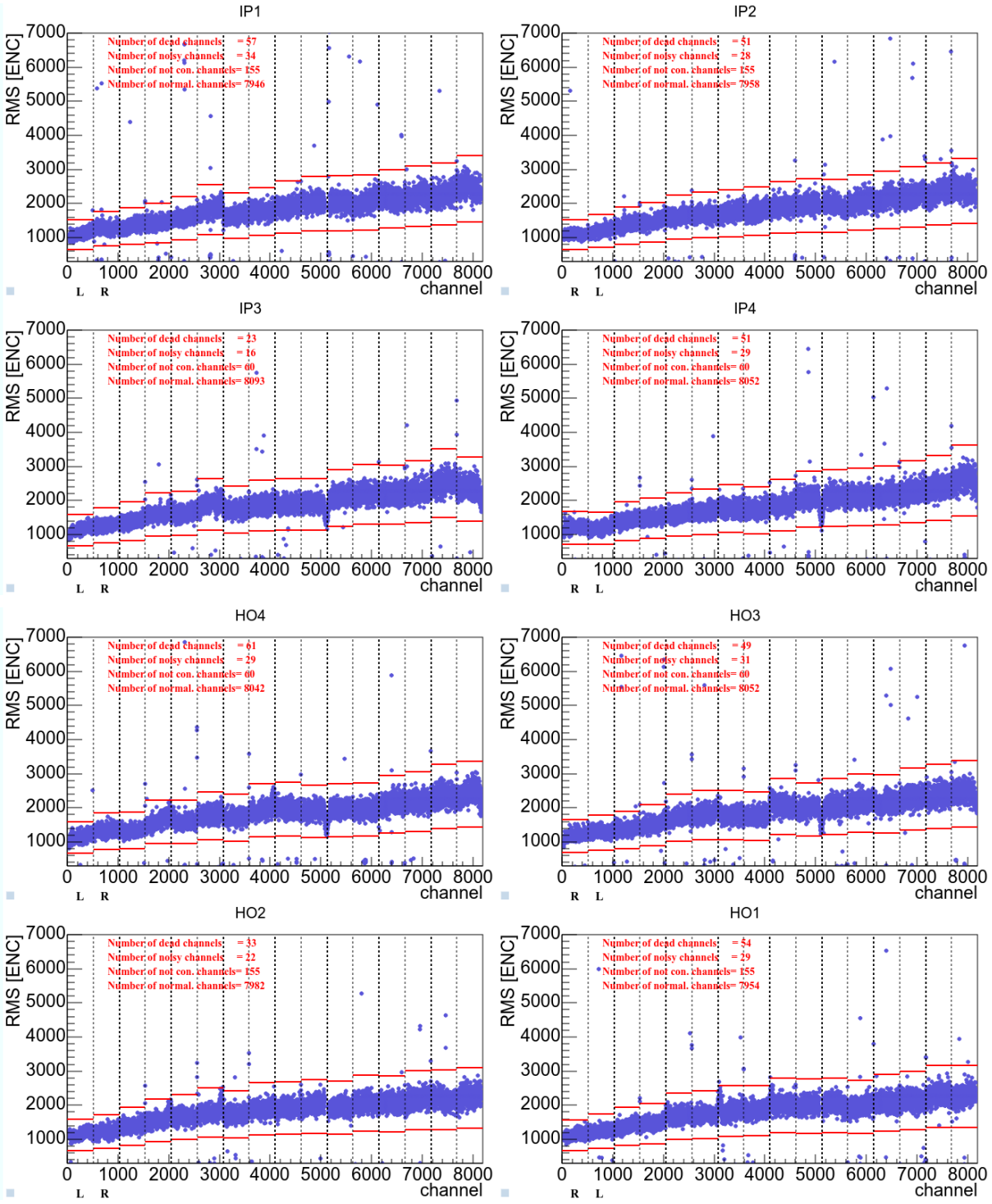

Figure 5.2: Sector A10 BB5 reference baseline.

The approach that was taken to find where the noise was coming from focused on eliminating subsystems as part of the problem. Thus the first thing the commissioning team tried was turning off HV power supplies but keeping them connected and running a baseline run again to see if anything changed. The results of that are presented in Figure 5.3:

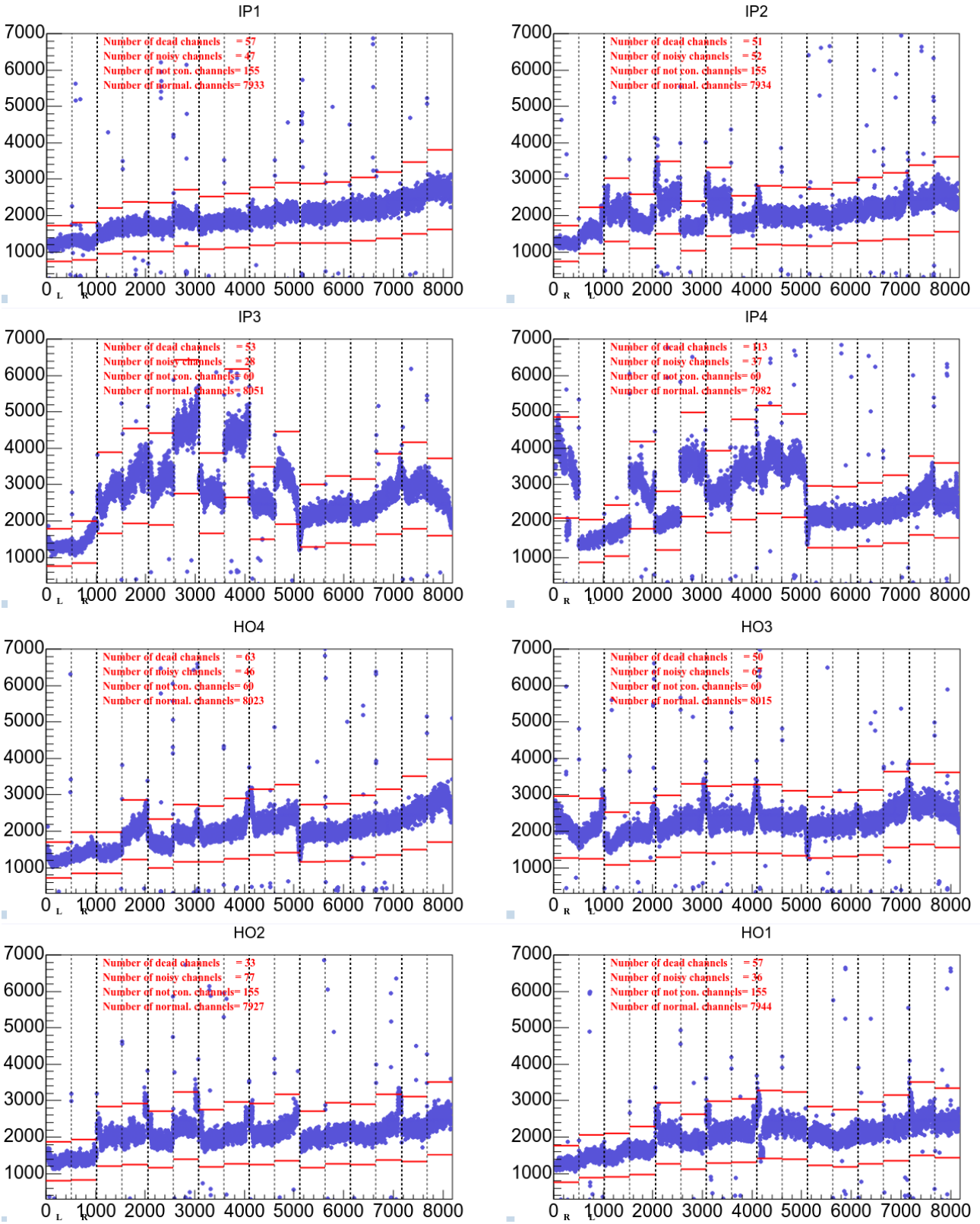

Figure 5.3: Baseline of sector A10 with HV part off. Vertical units are ENC, horizontal units are channel numbers.

The noise levels got better, especially on the IP side, but still were extremely high compared to the requirements and this fact was an indication of bad grounding between the sector's layers. This is what was investigated after those observations.

The first thing which was tested to improve the sector's grounding was the application of metallic tape between the layers IPL2 & IPL4 at PCBs 2, 3 & 4 since that on that side were the big noise problems as you can see in Figure 5.3. The metallic tape caused better grounding between these layers while it was also attached to the spacer frame which obviously is a grounding point:

Figure 5.4: Application of metallic tape between the layers of sector A10. [65]

The result of this test showed that this approach was in the right direction as the noise levels got better as seen in Figure 5.5. Since the HO layers aren't so problematic as the IP ones, from now on, the baseline graphs of A10 will be showing only the IP Layers.

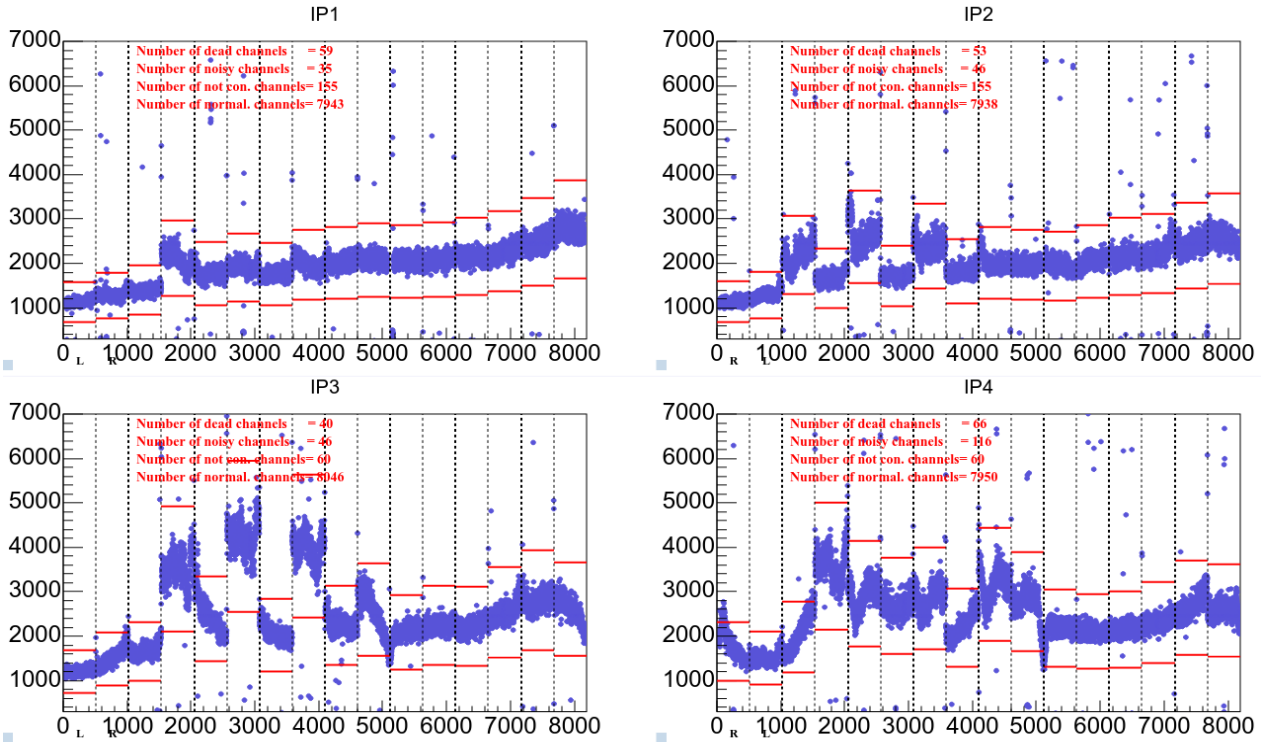

Figure 5.5: Effect of the metallic tape on noise levels of sector A10 - lowering side application. Vertical units are ENC, horizontal units are channel numbers.

The noise levels significantly improved in the lowering layers - exactly where the metallic tape was applied. This was a confirmation that the conclusion of bad sector grounding was valid. Subsequently, metallic tape was also applied between IP3, IP4 and the Spacer Frame on the Rising side as well giving the following results:

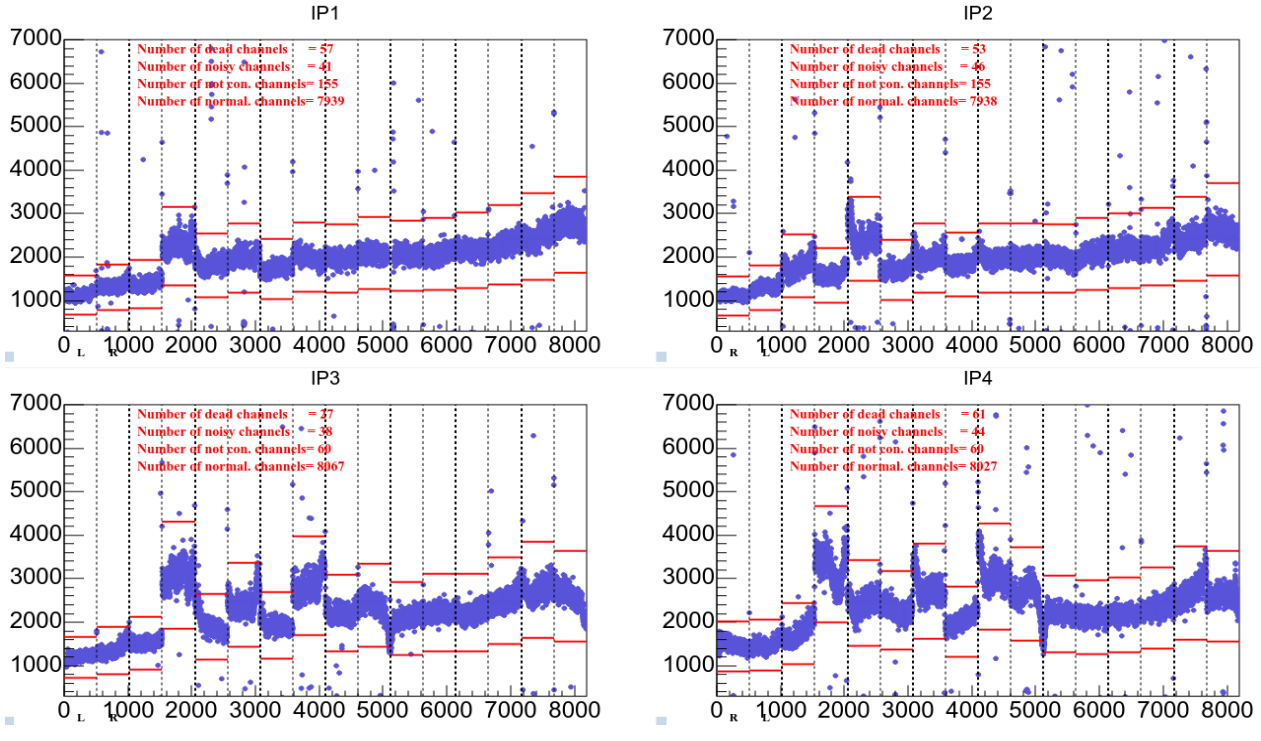

Figure 5.6: Effect of the metallic tape on noise levels of sector A10 - rising side application. Vertical units are ENC, horizontal units are channel numbers.

The improvement is visible through the naked eye! There is no need for a diff graph to understand how better the situation got using the metallic tape as short between these layers of ground and the Spacer Frame.

Although the metallic tape was revealed to be the solution to this problem it couldn't be a permanent solution for obvious reasons, so the commissioning team searched for a permanent way to bridge all those layers and as a result, the idea was to use cables that used crocodiles on one end and SF screws on the other. Shortly after that, the commissioning team replaced the cables with copper braids. The braids were selected due to their inductance characteristics which made them a filter too. The physical setup of a braid with the SF screw on one side and a crocodile terminal on the other can be seen in Figure 5.7:

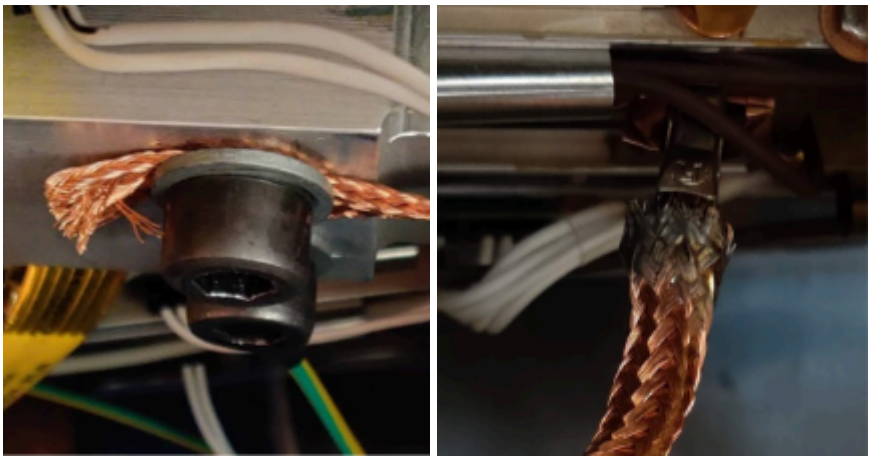

Figure 5.7: Screw and crocodile ends of a braid. [66]

The braids were added from the Spacer Frame to the cooling pipe of IP3 and IP4 and from IP1 PCB2 to the Spacer Frame all on the Rising side. Running a baseline with this configuration gave the following results as shown in Figure 5.8:

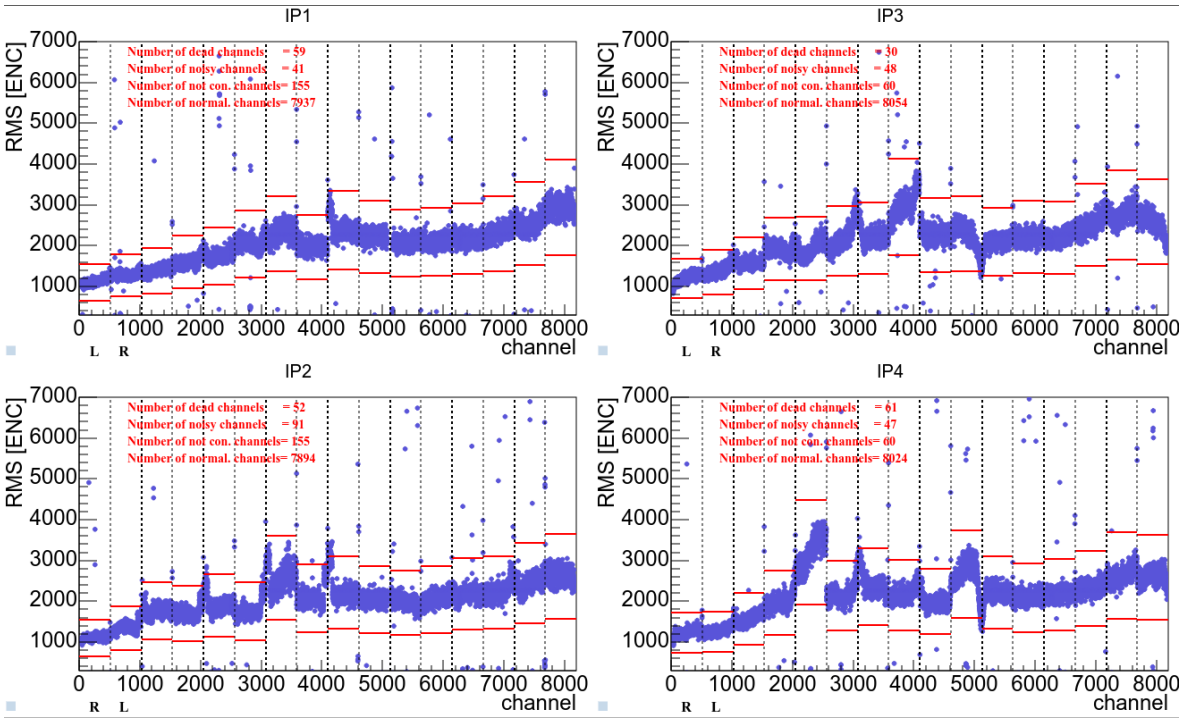

Figure 5.8: Effect of braids applied on IP1, IP2 and IP3 layers of A10 rising side.

Replacing all the metallic tapes with braids worsened the situation of the noise profile as presented in Figure 5.9:

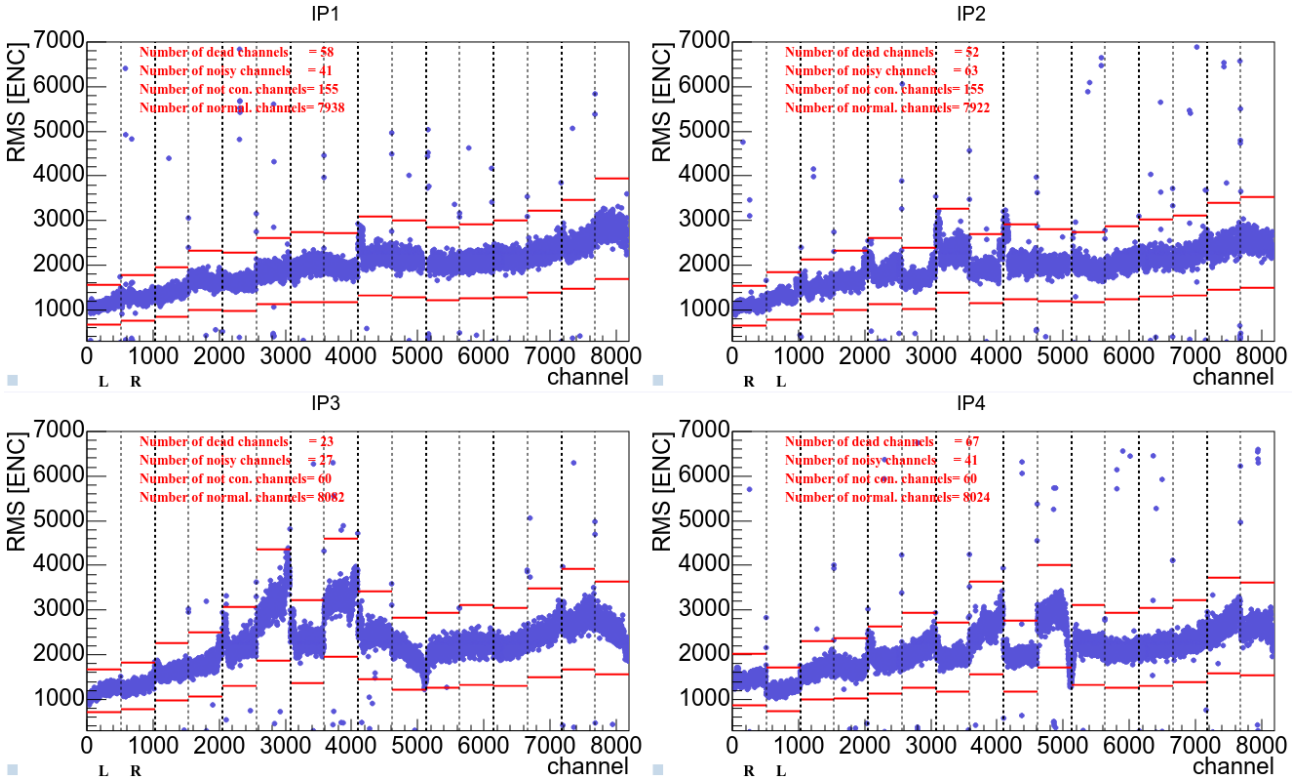

Figure 5.9: Baseline after replacing all the metallic tapes with braids on A10.

This noise profile for the IP3 and IP4 Layers isn't satisfactory. At this point, the braids on themselves had partially solved the problem and compared to the metallic tape they gave similar if not slightly better results on some points in terms of noise reduction.

At this point, the use of a baseline difference graph could help to see the difference between the metallic tape and the braids where the reference run is the metallic tape one:

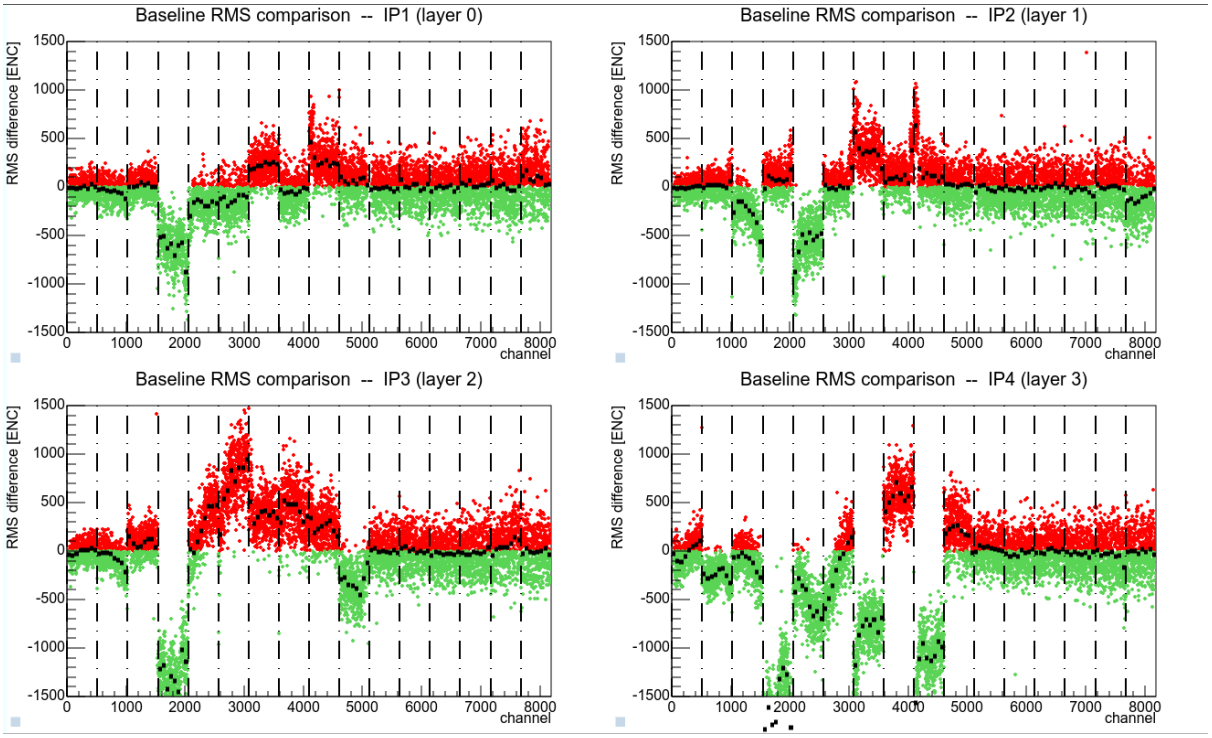

Figure 5.10: A10 baseline difference graph. Comparing noise using tapes vs noise using braids.

The installation has delivered good results but there's still enough room for improvement. At this point, the crocodile and screw terminals were abandoned and Cu plates were preferred for better mechanical support and better surface contact which also means better conductivity. Although on Sector 10 they proved to have identical results in the matters of noise after the baseline run.

Figure 5.11: Metallic plate ends of the braids.

To suppress the rest of the annoying noise levels more braids with Cu plates were used on the regions of the sector that still had high levels of noise such as the IP3 and IP4 Lowering side as well as on all layers of PCB2 and on 8 layers per side for PCB5 & PCB6. The results were really impressive as it can be seen in Figure 5.12:

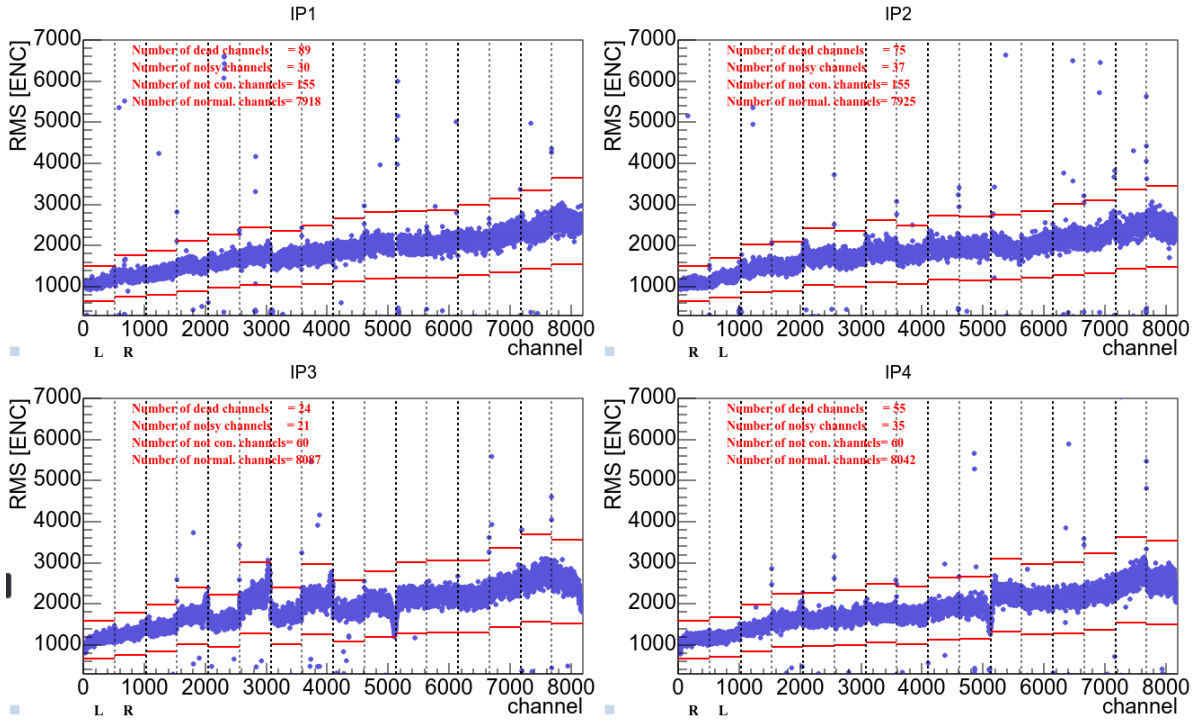

Figure 5.12: A10 baseline graph using even more braids.

All these copper braids were also covered by heat shrink tubes for safety reasons and to prevent any unwanted short circuits. The copper plate mountings were used only on wheel A because at the time this fix was implemented the MM wedges were already integrated and a more solid mounting method would be impossible. Although, for wheel C, it was possible to solder the copper braids on the wedges, instead of connecting them via copper plates, since this solution was discovered before the integration of wheel C detectors.

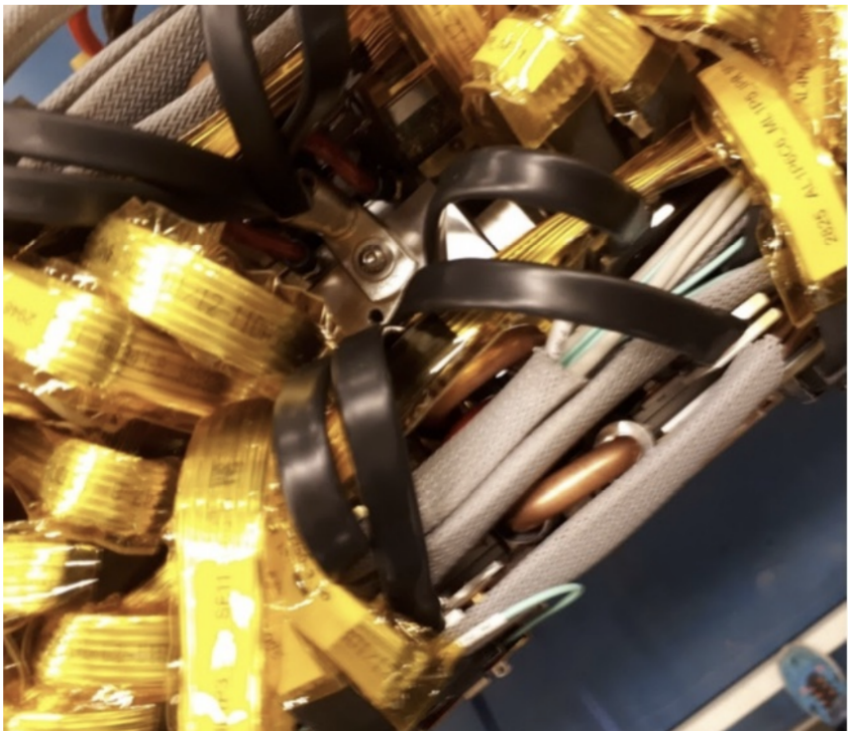

Figure 5.13: The copper braids connecting the PCBs to the spacer frame.

After several tests, among many sectors, this fix was found to be helpful for certain sectors that probably suffered from more damage than others. In other sectors, it was found to make no difference, and in some rare cases, it was actually increasing the noise due to ground loops. In total, this fix significantly reduces the noise in many sectors across many PCBs and as a result, the efficiency of the MM detectors was improved.

5.1.2 ICS Noise

While searching for the noise source, the ICS power supply was investigated. Step by step, parts of the ICS that were prone to noise were fixed. The branch controller cable was neither shielded nor grounded and was refurbished by using metallic tape to shield the flat cable, that was then soldered on the shielding of the connectors and then capton tape was used to electrically insulate the cable and also make it more robust. This way all the connectors were grounded and no noise could be introduced from this cable. Also, a termination was added to these cables to stop them from picking up external noise. Parts of the ICS, like the handles and some parts of the cover, were not properly grounded, because they were covered in non-conductive paint. As a result, the non-grounded parts were picking up noise that was transferred to the LV outputs and were also an electric shock hazard.

Figure 5.14: The refurbished branch controller flat cable.

Another substantial problem related to the noise was a noise spike around 5MHz which was present in all sectors, affecting the whole sector but it was increasing as moving from the inner radius to the outer radius, so the biggest problem was on PCB 8. The source noise turned out to be the ICS module, as it was measured with an oscilloscope without load and the noise signal was crystal clear. For fixing this problem, a filter was designed and installed on every ICS channel output, with capacitors selected specifically to maximise the filtering around 5 MHz, resulting in a much smoother output and, eventually solving this problem. The impact of this improvement is demonstrated through sector A10 in Figures 5.17, 5.18, and 5.19.

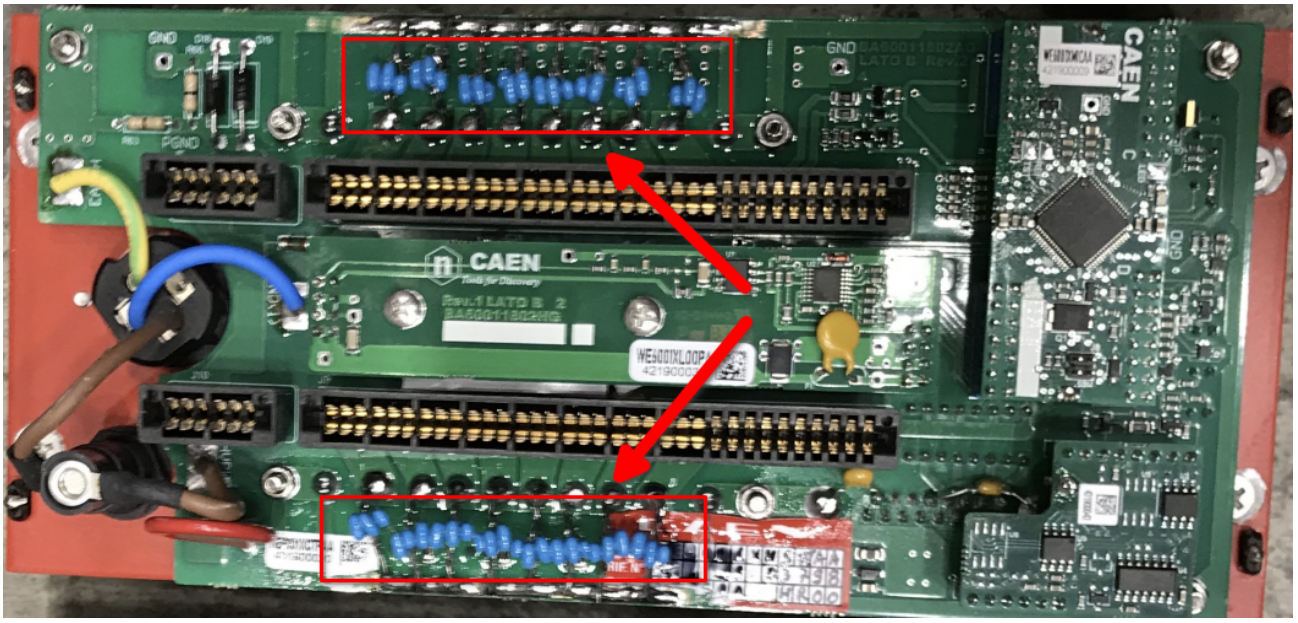

Figure 5.15: The ICS filter prototype that was initially developed with the combination of three through-hole capacitors, valued at 1.0 μF||0.680 μF||0.470 μF.

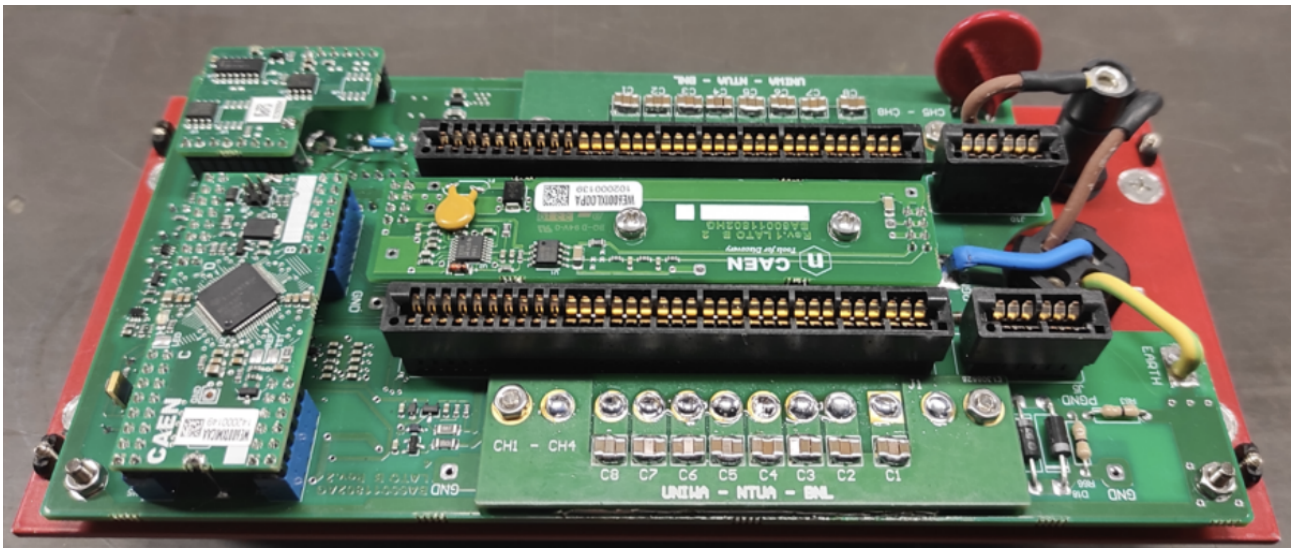

Figure 5.16: The ICS Output Filters. The mezzanine board was developed later, using 2.2 μF||1.5 μF||1.0 μF capacitors.

Picking up A10 from where we've left it off, all the front panels of the ICSs that power up sectors A10 and A11 were modified by adding this filter on every output. A baseline test as usual shows the impact of this intervention on the noise levels of sector A10, as shown in Figures 5.17 and 5.18 for the IP and HO sides, respectively.

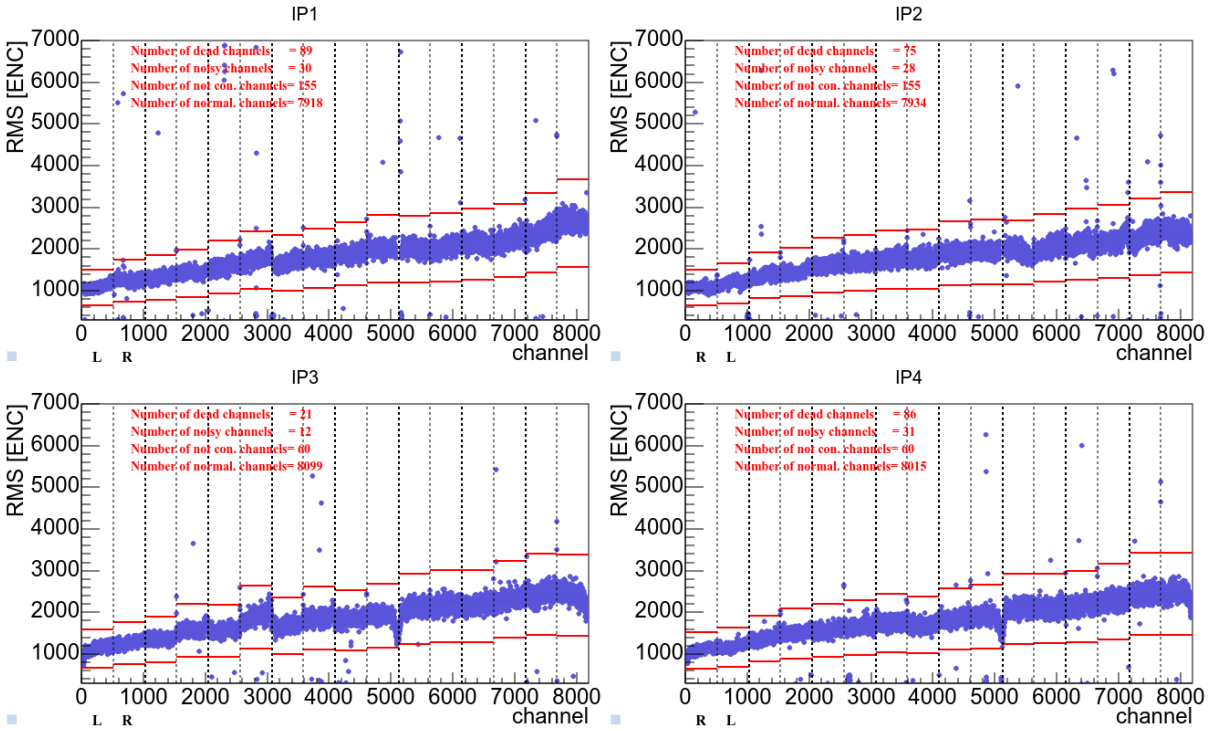

Figure 5.17: Effect of modified ICS on sector A10 IP side.

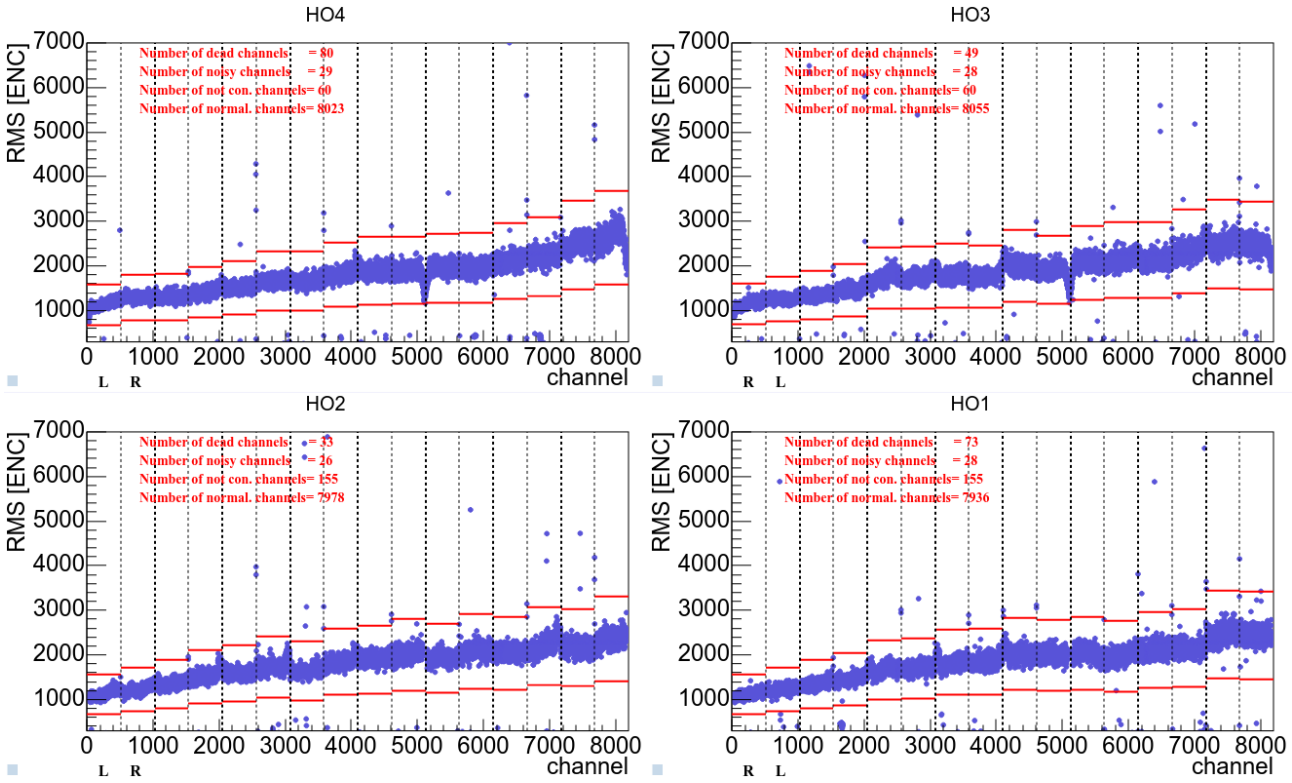

Figure 5.18: Effect of modified ICS on sector A10 HO side.

As seen in Figures 5.17 and 5.18 the noise levels got to a very satisfactory level where the noise levels approached the levels the MM wedges had during their integration before leaving the BB5 building. With the help of a baseline Difference graph, we will compare the effect of the ICS filters on the noise levels of the IP layers on top of the final braid configuration as seen in Figure 5.19.

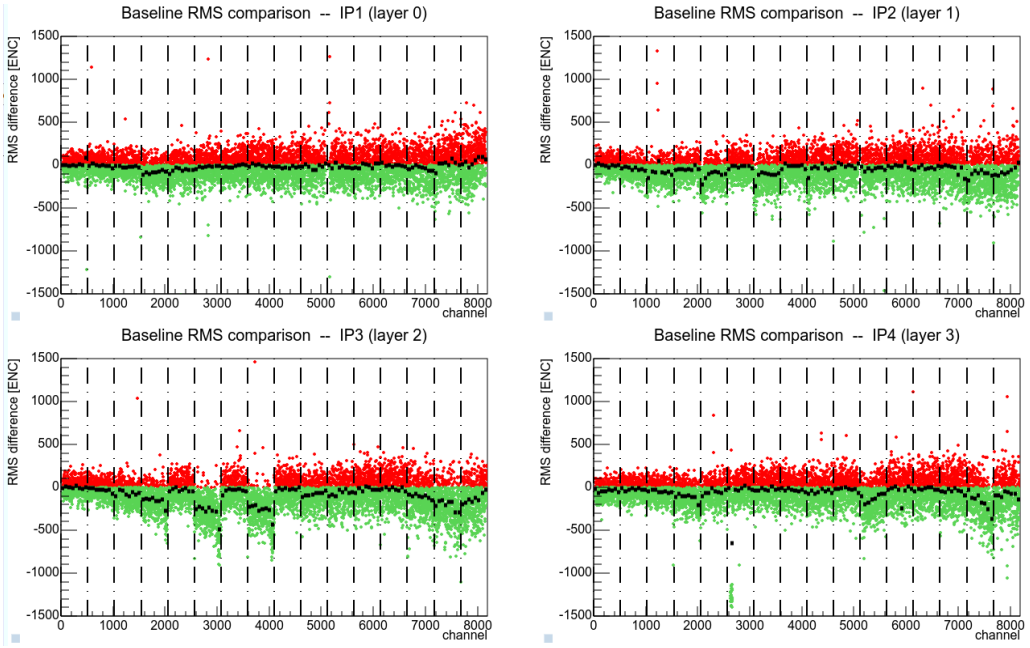

Figure 5.19: A10 difference graph. Effect of modified ICS on top of final braid configuration. IP side.

The ICS filter improved, even more, the situation on sector A10 bringing the noise levels to the pre-commissioning situation when the MM wedges were being integrated at the BB5 building. The next baseline run in Figure 5.20 compares the sector condition at the time compared to the BB5 noise levels on all layers, both IP and HO. Their situation is almost identical, having slightly better or slightly worse noise levels at some points.

Sector A10 now can be considered fully commissioned since it is on the wheel and capable of working under the best possible condition. Of course, the noise levels were not the only challenges the team faced during the commissioning but since it was one of the most prominent issues it was the biggest headache and one of the most important things to troubleshoot so that the sector could work properly.

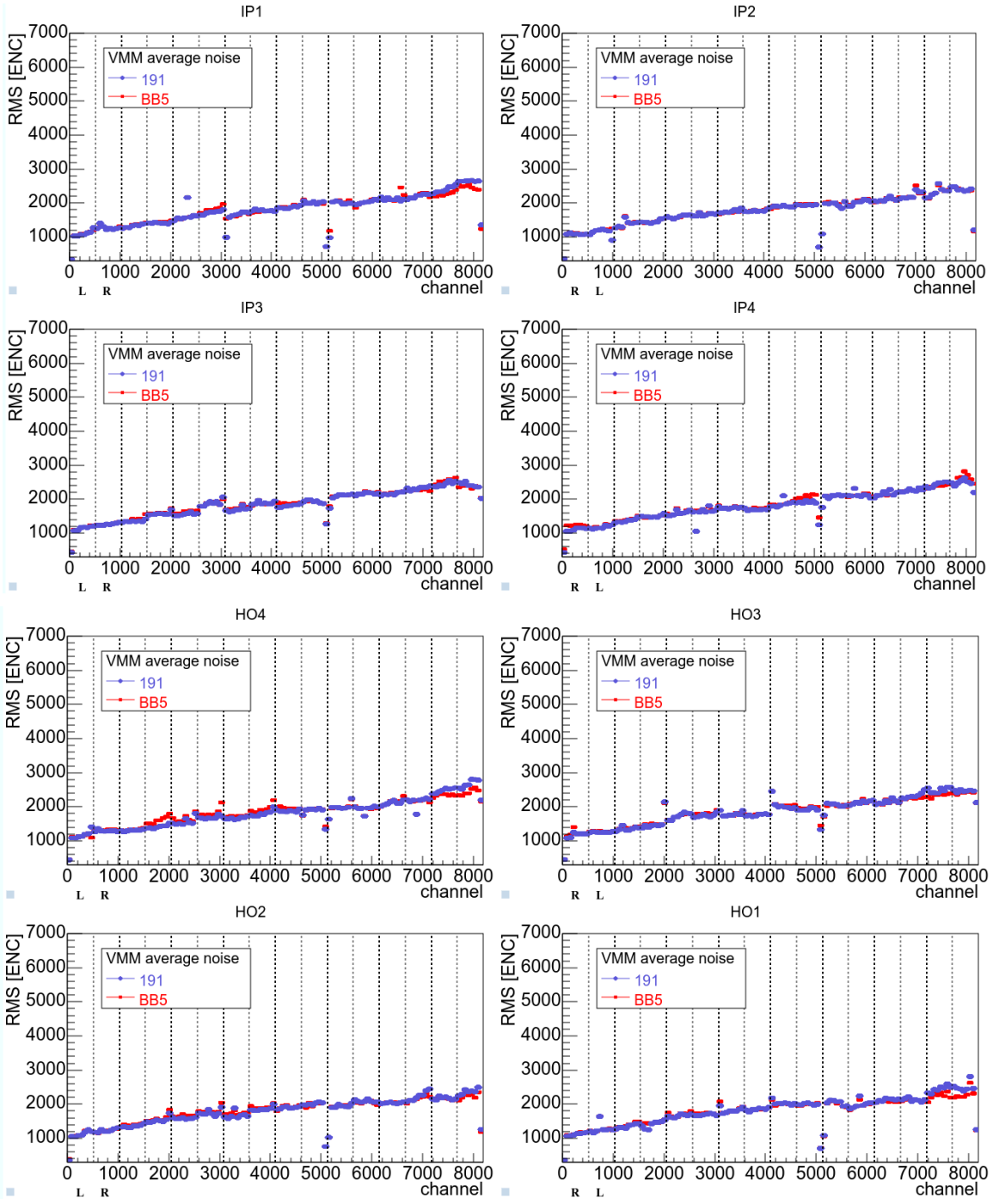

Figure 5.20: Baseline of fully commissioned A10 noise levels vs BB5 reference noise levels.

5.1.3 T-sensor - ELMB related Noise Issues

Certain sectors showed even more increased noise, especially on PCB 8, where this noise could not be appointed to the ICS or the grounding. In some of these cases, it was caused by the temperature monitoring systems. Some sectors showed increased noise when the ELMB power was ON. A good example of this case is Sector A02. Its baseline revealing the problem is shown in Figure 5.21:

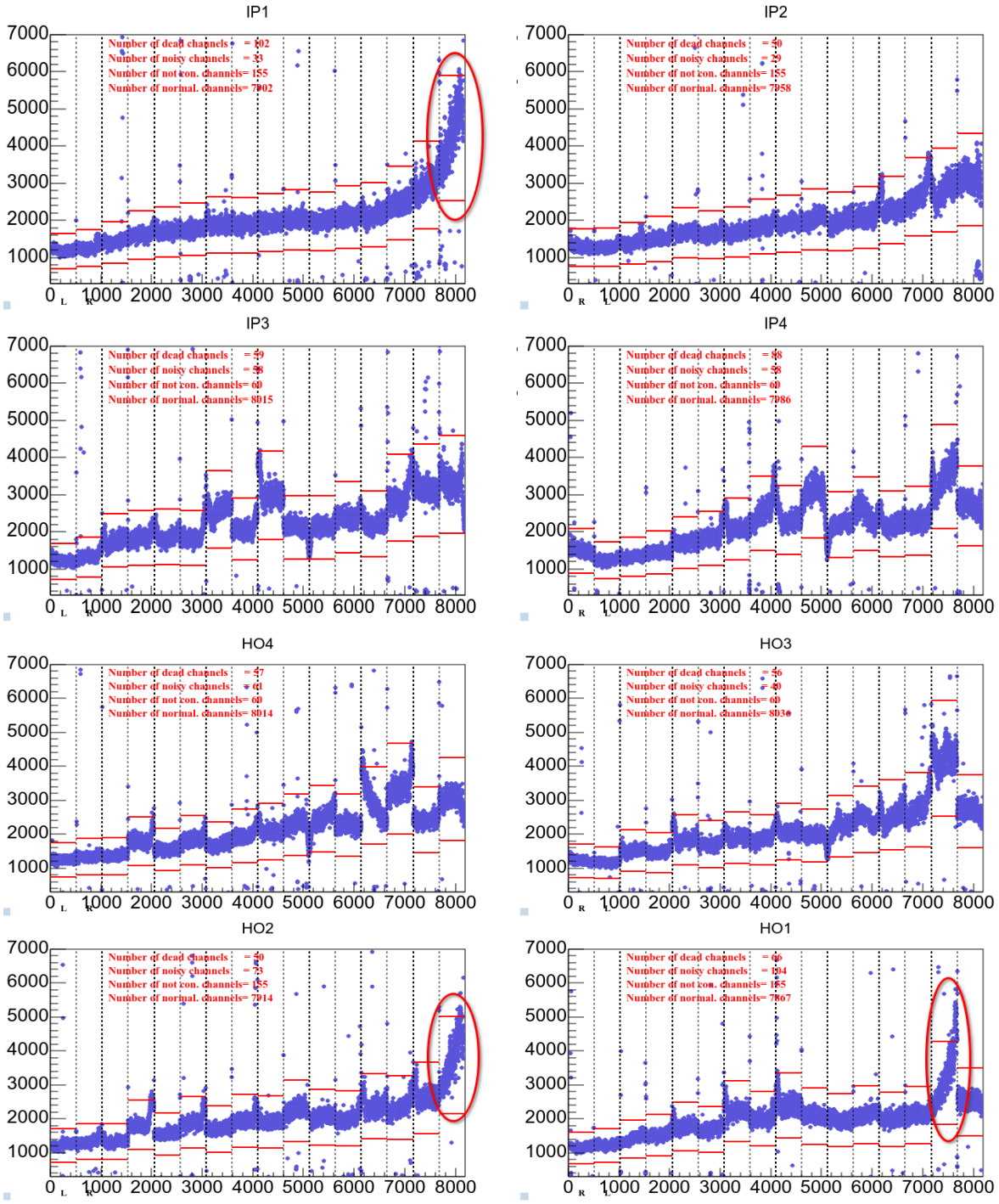

Figure 5.21: Noise spikes on A02 after powering on the T-sensors. Vertical units are ENC, horizontal units are channel numbers.

The problem on PCB8 is obvious in IP1, HO1, and HO2. When turning OFF the ELMB of sector A02 and retaking baselines the noise was not visible anymore, meaning that the ELMB is the source of that noise.

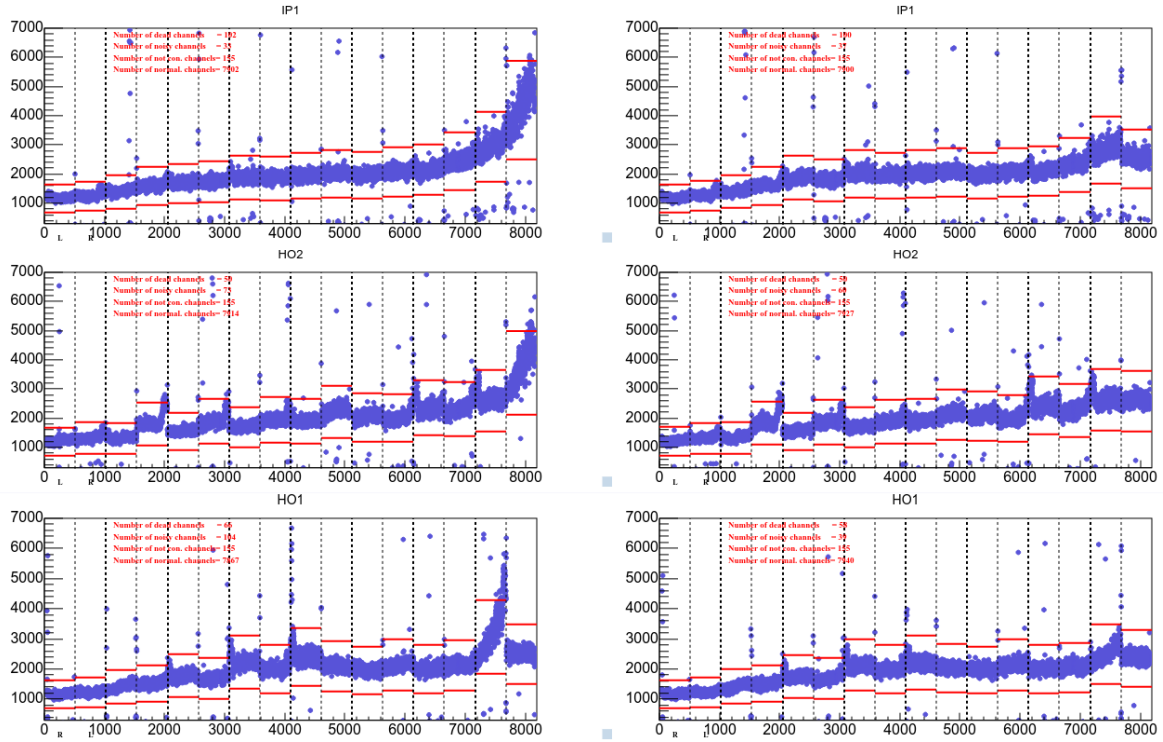

Figure 5.22: Side-by-side comparison of IP1, HO1, and HO2 noise having ELMB turned on VS ELMB turned off on A02. Vertical units are ENC, horizontal units are channel numbers.

While trying to solve this problem, another power supply was used to examine if the noise levels change. That power supply was from A10 ELMB and as seen in Figure 5.23 the noise profile is almost identical to how the noise looked when the power supplyof the A02 ELMB was turned off.

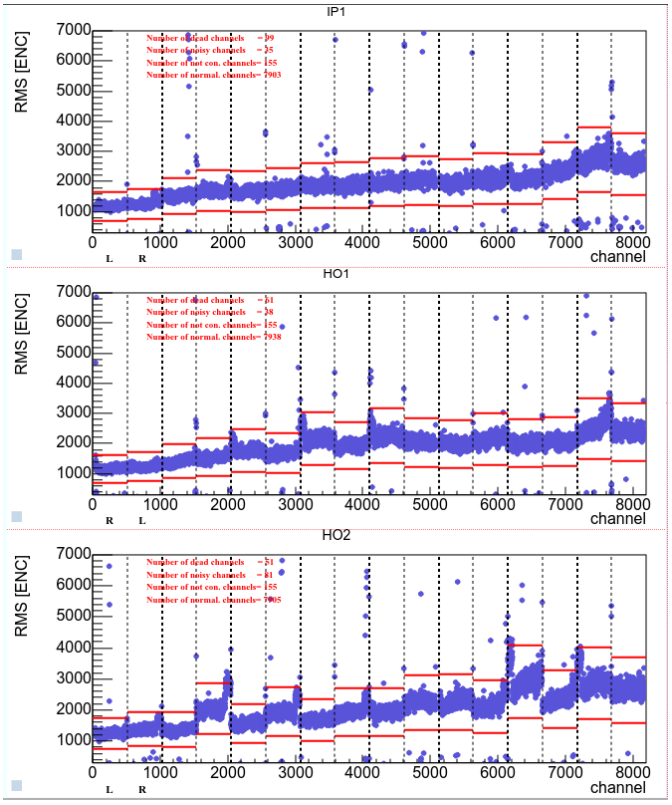

Figure 5.23: Sector A02 noise using ELMB from sector A10.

After close inspection, it was seen that some of the ELMB power supplies needed to have filters added to their outputs, as they were generating noise. In addition, a shielded CAN bus cable was used. After this intervention, this type of noise was reduced but did not disappear. Compared to the A10 ELMB power supply the interventions on the A02 ELMB power supply didn't deliver the same results but the noise profile was improved compared to the previous one, before those interventions. The noise levels were brought to desirable levels after all the aforementioned interventions described in Subsection 5.1.1 and Subsection 5.1.2.

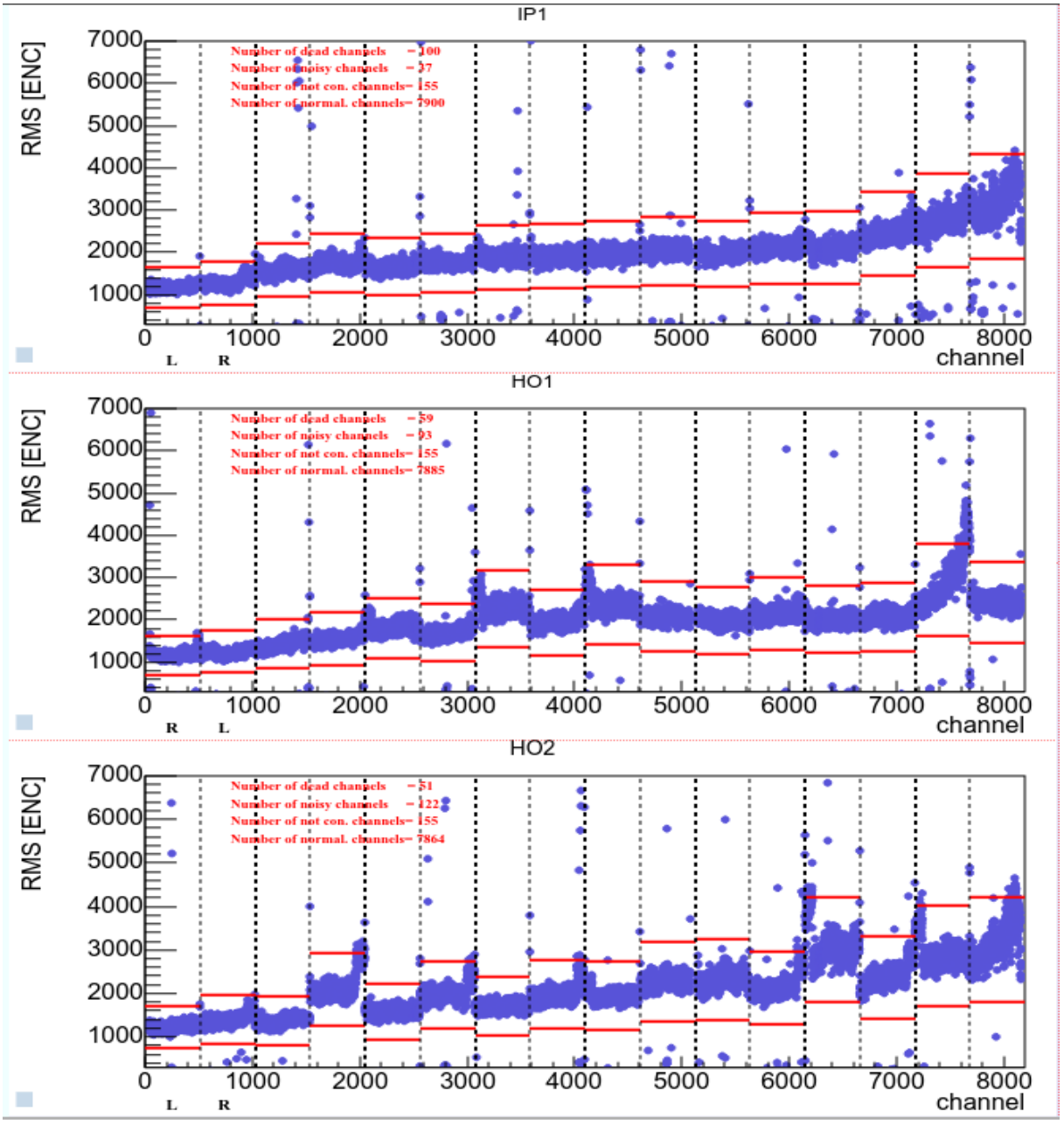

Figure 5.24: A02 noise using modified ELMB power supply..

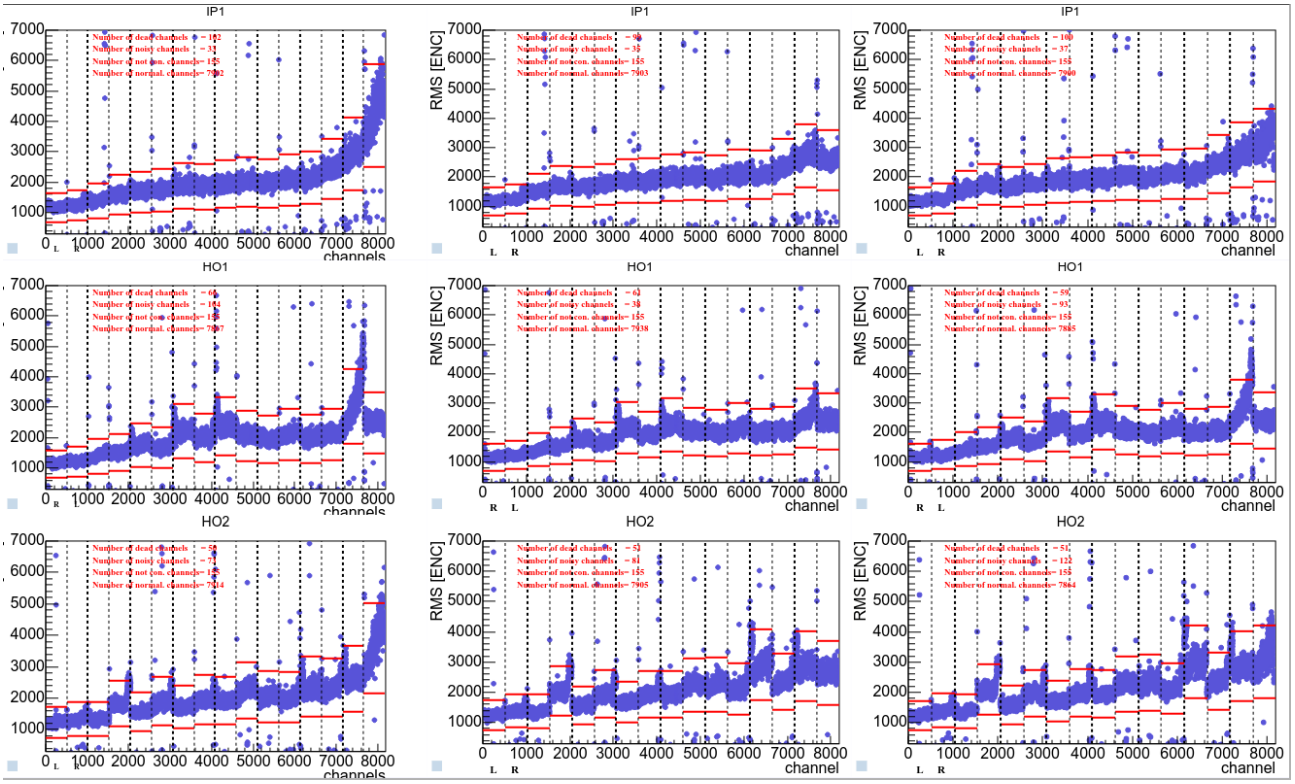

Figure 5.25: Noise levels of A02 initially VS using A10 power supply VS using A02 modified power supply.

In Figure 5.25 there are the three layers placed per row. In the first column, the reference noise levels are shown for these layers while using the unmodified power supply of the Sector A02 T-sensors. In the middle column are the noise levels of those layers while using the A10 MDM power supply while in the last column, the final noise levels are presented using the modified MDM power supply.

5.1.4: Noise caused by the Cooling System Chiller

One more major noise source in some sectors of wheel A was the chiller of the water cooling system. This problem occurred after a new auxiliary chiller was installed in order for the old chiller to be serviced and in turn to increase the cooling capacity and be able to commission more sectors in parallel. The new chiller introduced a lot of noise mostly on the high-numbered PCBs of sector A15 due to high-frequency harmonics produced by the chiller's inverter. In Figure 5.26 we can see the noise situation of Sector A15 after the modified ICS front panels were installed and before said chiller implementation.

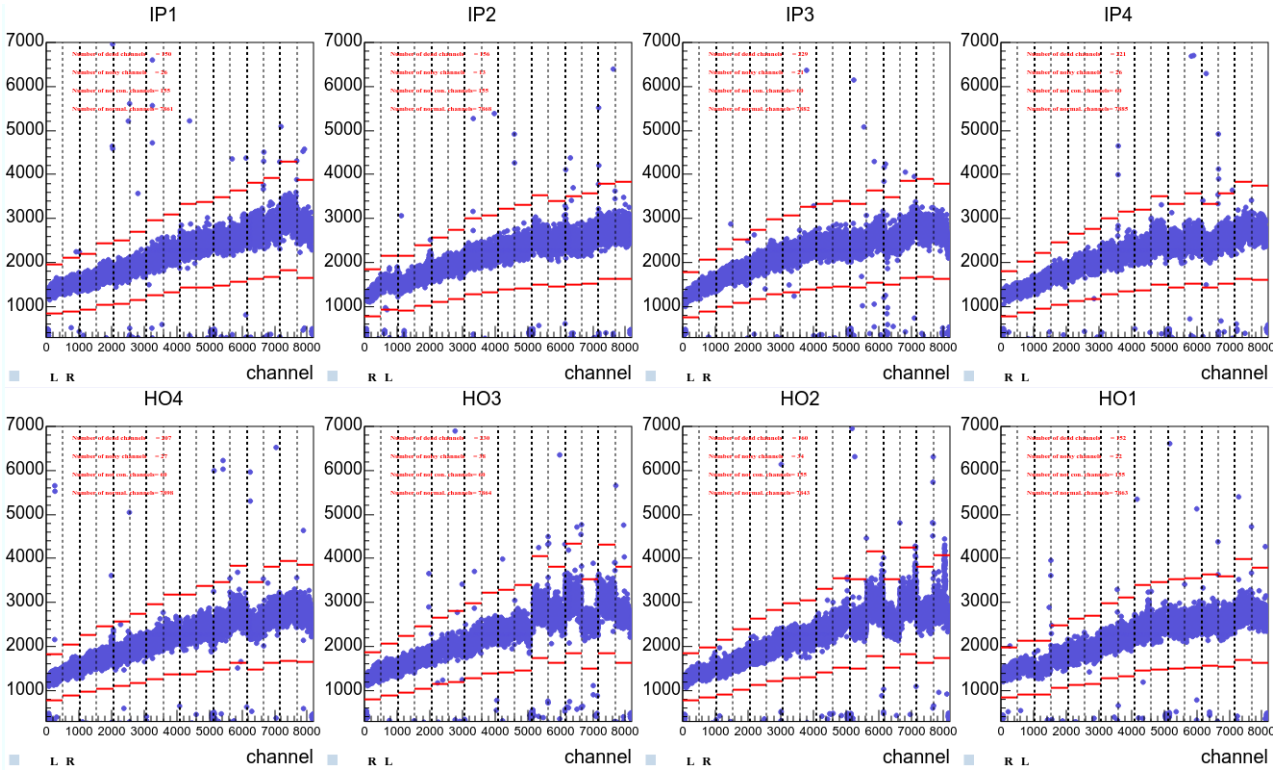

Figure 5.26: Sector A15 baseline on final ICS configuration. Vertical units are ENC.

After the installation of the new chiller the noise across most layers was increased and especially in layers IP1 and HO1 this increase was quite dramatic as can be seen in Figure 5.27. Initially, the grounding points were investigated and also the activity of the neighbouring sectors was monitored but none of that seemed to be the issue.

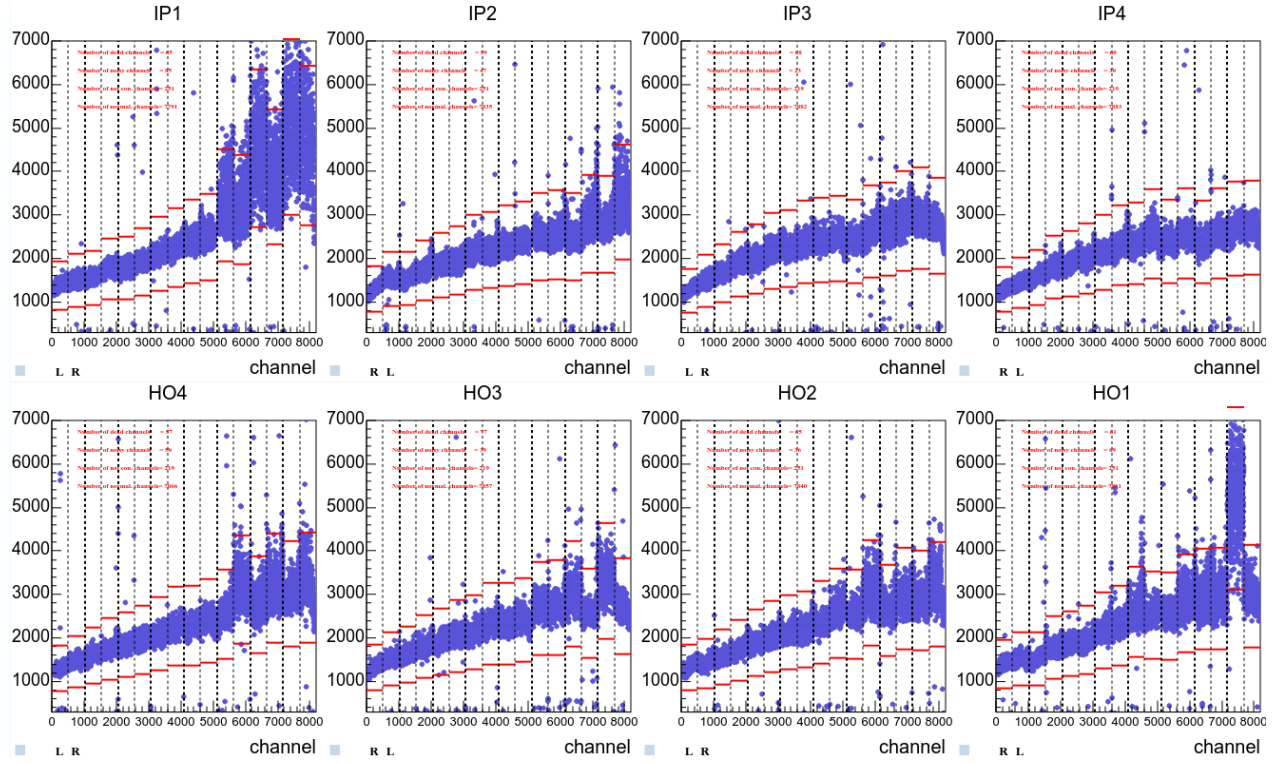

Figure 5.27: Effect of new chiller on noise levels of sector A15. Vertical units are ENC.

It was realised that the only addition to building 191 before the noise levels of Sector A15 started worsening was the addition of the new chiller, it was the next point of investigation. With the chiller turned off, a baseline was taken immediately after turning on the sector since the sector electronics could be operated for about 20 minutes without cooling. This baseline has shown very low noise levels so it could be concluded that the chiller was the cause of the noise observed.

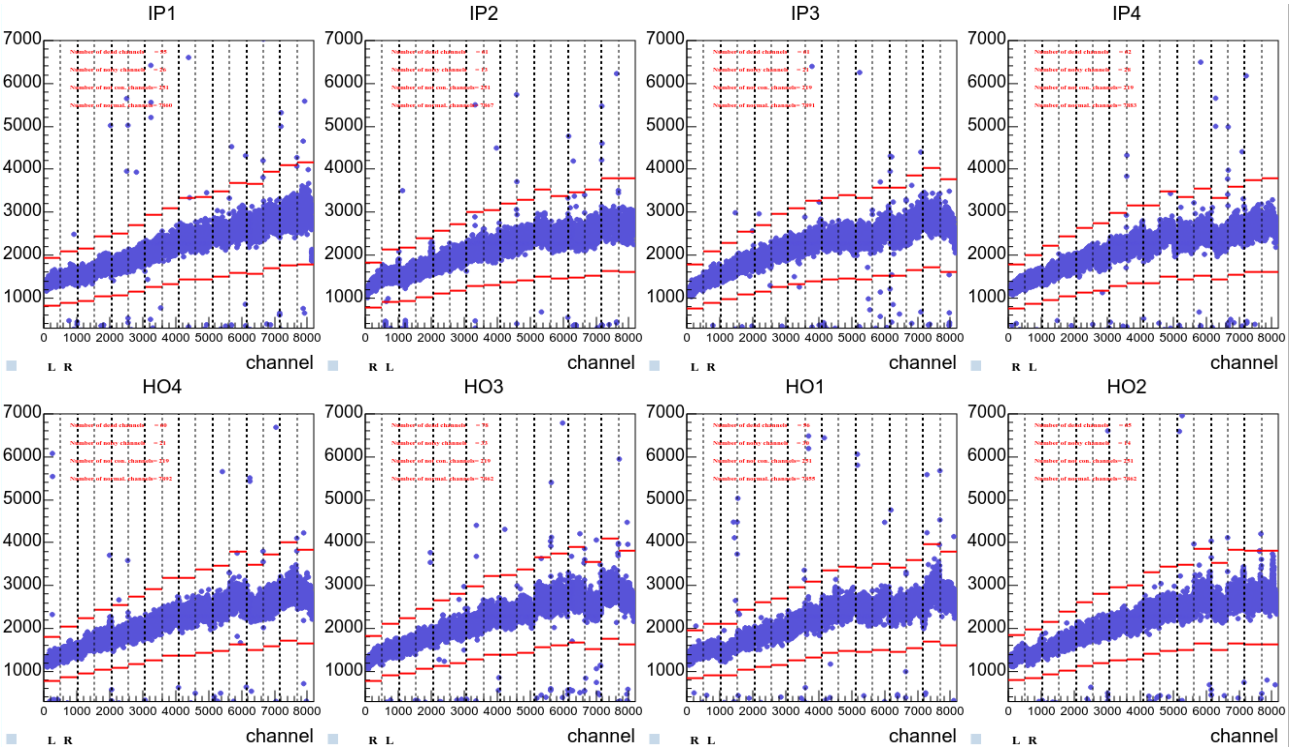

Figure 5.28: Baseline of sector A15 with chiller turned off. Vertical units are ENC.

Since the new chiller was the culprit a way to reduce its noise effect had to be found. It was observed that the chiller's grounding point was near that of Sector 15. In order to mitigate the issue the grounding point of the chiller was moved away from the sector ground. As a result in Figure 5.29 we can see the noise was a little bit higher than when the chiller was completely shut off but it has still greatly improved to when the chiller was on and grounded near the sector.

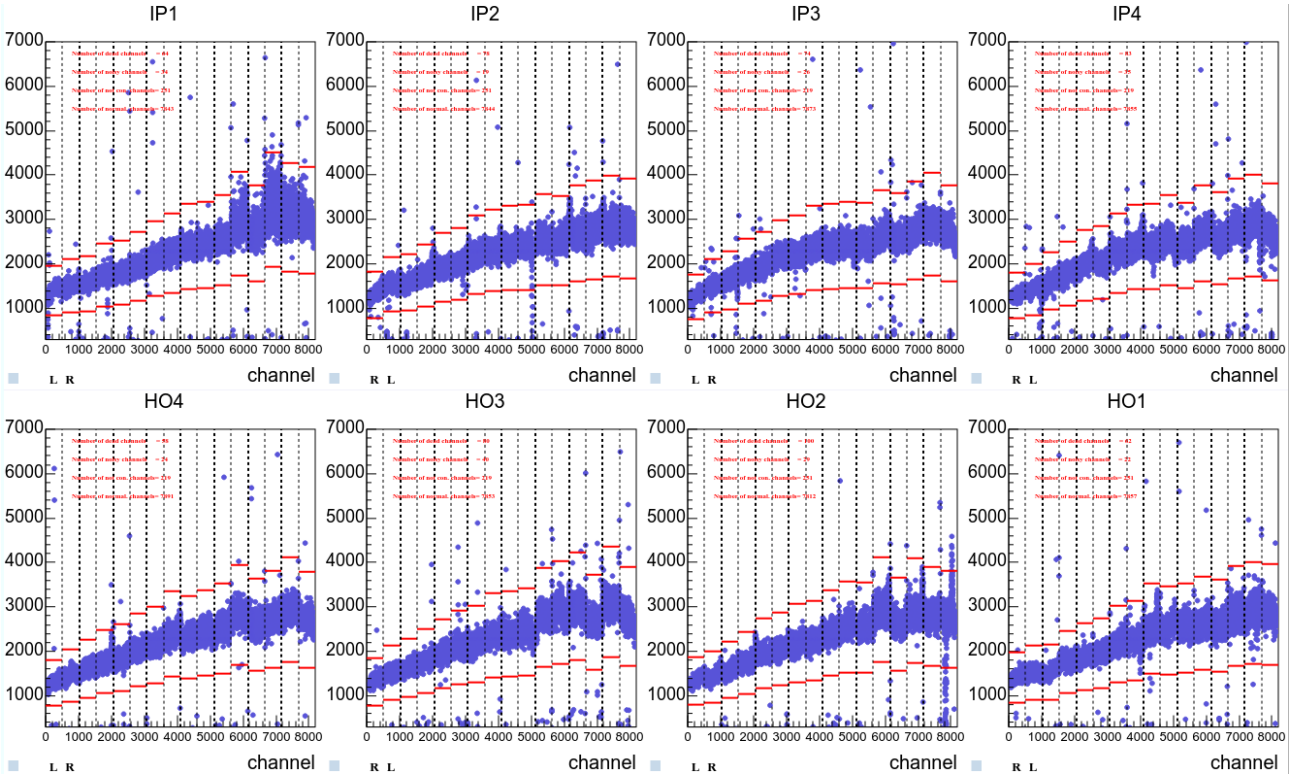

Figure 5.29: Sector A15 noise after the chiller ground moved away from the sector ground. Vertical units are ENC.

Hereafter this problem is not present when the NSWs are installed in Point 1 since the cooling systems there are designed not to interfere with the electronics of any detector, so finding a solution to this issue was only important for the purposes of the commissioning.

5.2 Low Voltage Related Problems

This section contains the description of polarity, continuity and mapping checks, reasons behind LVDB failures and their mitigation and also a description of a problem related to increased temperatures on some LVDB connectors and its solution.

5.2.1 Polarity, Continuity and Mapping Checks

Throughout the surface commissioning phase, numerous problems related to powering the LV electronics occurred. As described in the workflow every LV channel would be connected to the corresponding LVDB. But before connecting any LVDB, all the Low Voltage connectors would be checked for mapping, continuity and polarity, the last test being the most important one.

The mapping describes which ICS channel should power a corresponding LVDB and consequently the corresponding group of electronics. In certain cases, there were 2 or more channels that would be out of place. Since there is a certain amount of LV channels allocated for use by the MicroMegas detectors mapping discrepancies could only be swaps. When such an issue was found, it would either be a mismatch in the placement of the 4-channel connector on the ICS, or a mistake in the connector itself. In this case, either the commissioning team or the service team would remake the connector.

S12-MM-LV-L1P8-IPL-D-SL1 S12-MM-LV-L1P8-IPR-D-SL2	S12-MM-LV-L4P8-IPL-D-SL2 S12-MM-LV-L4P8-IPR-D-SL1	S12-MM-LV-L4P8-HOL-D-SL1 S12-MM-LV-L4P8-HOR-D-SL2	S12-MM-LV-L1P8-HOL-D-SL2 S12-MM-LV-L1P8-HOR-D-SL1
S12-MM-LV-L1P2-IPL-A	S12-MM-LV-L4P2-IPL-A	S12-MM-LV-L4P2-HOL-A	S12-MM-LV-L1P2-HOL-A
S12-MM-LV-L1P2-IPR-A	S12-MM-LV-L4P2-IPR-A	S12-MM-LV-L4P2-HOR-A	S12-MM-LV-L1P2-HOR-A
S12-MM-LV-L1P8-IPL-A	S12-MM-LV-L4P8-IPL-A	S12-MM-LV-L4P8-HOL-A	S12-MM-LV-L1P8-HOL-A
S12-MM-LV-L1P8-IPR-A	S12-MM-LV-L4P8-IPR-A	S12-MM-LV-L4P8-HOR-A	S12-MM-LV-L1P8-HOR-A
S13-MM-LV-L4P8-IPL-D-SL2 S13-MM-LV-L4P8-IPR-D-SL1	S13-MM-LV-L4P8-IPL-A	S13-MM-LV-L4P2-HOL-A	S13-MM-LV-L4P8-HOR-A
S13-MM-LV-L4P2-IPL-A	S13-MM-LV-L4P8-IPR-A	S13-MM-LV-L4P2-HOR-A	S13-MM-LV-L1P8-HOL-D-SL2 S13-MM-LV-L1P8-HOR-D-SL1
S13-MM-LV-L4P2-IPR-A	S13-MM-LV-L4P8-HOL-D-SL1 S13-MM-LV-L4P8-HOR-D-SL2	S13-MM-LV-L4P8-HOL-A	S13-MM-LV-L1P2-HOL-A

(a)

S13-MM-LV-L1P8-IPL-D-SL1 S13-MM-LV-L1P8-IPR-D-SL2	SD-S12-L1234	SD-S12-L5678	SD-S13-L5678
S13-MM-LV-L1P2-IPL-A	S12-ST-LV-L1-IPR	S12-ST-LV-L3-IPR	S12-ST-LV-L5-HOL
S13-MM-LV-L1P2-IPR-A	S12-ST-LV-L2-IPR	S12-ST-LV-L4-IPR	S12-ST-LV-L6-HOL
S13-MM-LV-L1P8-IPL-A	SPARE	SPARE	SPARE
S13-MM-LV-L1P8-IPR-A	S13-ST-LV-L1-IPL	SD-S13-L1234	S13-ST-LV-L5-HOR
S13-MM-LV-L1P2-HOR-A	S13-ST-LV-L2-IPL	S13-ST-LV-L3-IPL	S13-ST-LV-L6-HOR
S13-MM-LV-L1P8-HOL-A	S12-ST-LV-L7-HOL	S13-ST-LV-L4-IPL	S13-ST-LV-L7-HOR
S13-MM-LV-L1P8-HOR-A	S12-ST-LV-L8-HOL	SPARE	S13-ST-LV-L8-HOR

(b)

Figure 5.30: The ICS mapping. describing how two full NSW Sectors connect to two ICS crates. (a) is the lowering side ICS mapping and (b) is the rising side ICS mapping.

To fully explain how the mapping works we have to explain it in separate ways. Figure 5.30 (a) describes the mapping of the lowering ICS while (b) describes the mapping of the rising ICS. The Micromegas LV channels are labelled in blue (deep blue for the digital channels) while the sTGC channels are labelled in yellow. Each column describes a separate power module of each ICS and each row describes a separate LV channel for each power module. The coding for MicroMegas describes the position of the LVDBs and goes as follows:

S(AA)-MM-LV-L(B)P(C)-(DD)(E)-(F)-SL(G)

- AA is the sector number
- B is the layer number and C is the PCB number
- DD is either the IP or the HO side
- E is either the lowering (L) or the rising side (R)
- F is either analog (A) or digital (D)
- G is the slot number and is only valid for digital channels (2 digital LVDBs per LV channel)

When doing the mapping tests there could be certain channels that could not output any voltage. In this case, the first step would be to check the ICS itself. If the CAEN GECO software reported no voltage output even when the module was turned on, then the Power Board or the Front Panel could be at fault, and they would need to be fixed or replaced. If voltage is registered in the software then we should be able to read it with a multimeter, directly on the ICS output. In most cases where the voltage was detected on the ICS but could be read on the detector side, the connector was not properly connected on the ICS side. And actually, there was never a case where a cable was at fault and needed to be replaced. It was always the connector's fault on one side or the other, and it was just a matter of connecting them properly or remaking them in some cases.

Even when the correct mapping and continuity were ensured there was one final step before connecting and powering the LV electronics, and that was to make sure the polarity was correct. Due to human error, certain channels could have been connected with the wrong polarity. In most

cases, issues like this were found before powering on the Sector and were fixed. Unfortunately, there were times when these issues were not detected, resulting in a major issue during the commissioning phase of the New Small Wheel upgrade.

5.2.2 Burnt LVDBs

A wrong polarity would result in burning the reverse-polarity-protection SMD fuses of the LVDB. This rendered the LVDB unusable, and an on-wheel refurbishment of the LVDB was impossible, so this LVDB would have to be removed and replaced to be cast usable again. This design choice protected the much more valuable front-end electronics from power issues but made it very hard to swap the LVDB in case it was burnt.

In the early stages of the commissioning phase, this issue was serious but rather possible to fix. But considering that LVDBs are present on PCB2 and PCB8, once larger sectors were being installed, covering the small ones, a burnt LVDB would become a much more complicated issue. A PCB2 LVDB of a Small Sector being covered by two Large Sectors would be impossible to fix by removing these Large Sectors. Unfortunately, this was the case for a Small Sector in Wheel A, when an ICS connector was refurbished, and connected with the wrong polarity missing the usual check.

But this issue's cause was not only reversed polarities. In certain cases, during normal day-to-day commissioning activities, some LVDBs were burnt for no apparent reason. To this day, the only unconfirmed explanation that was given is that sometimes when immediately turning an LV Channel off and on again, a high peak current could go through the LVDB, burning its fuses. Another speculation made by the authors is that the fuses that were selected for the LVDB were unsuitable for this use since during connector temperature tests, these fuses were getting quite hot under normal operation. But to change the fuses used, at this point of commissioning on all the LVDBs would be impossible.

Nevertheless, this issue affects 5 LVDBs on both wheels, out of the 512 LVDBs on both wheels, resulting in a small percentage of lost channels.

5.2.3 Overheating Connectors

The LV connectors used on the LVDBs and Extension Cables have certain specifications that need to be met in order to function without issues. At the early and mid stages of the commissioning, these specifications were not fully met, leading to issues in continuity and overheating, which in turn led to current being wasted on a bad connection and front-end electronics not being powered properly.

Concerning the Extension Cables, it was rather easy to refurbish them. Instead of using the original connectors, Supersabre connectors were used in order to connect the ICS side end of the extension cable and the Extension Cable end of the ICS to the "Extension Cable" cable. The switch to Supersabre connectors was quick and easy since they were already being used from the sTGC Low Voltage chain.

The solution for the LVDB connector on the LVDB itself was not as straightforward, since changing the design of the LVDB during the commissioning stage to use a different connector, would set back the NSW Upgrade even further. In order to keep these connectors from being damaged and overheating, the conductors of the connector would have to be kept straight for at least 5 cm. So a 3D-printed bracket was designed to keep those conductors neat and straight. After

all the male connectors were refurbished, these brackets were installed which resulted in the issue being completely mitigated.

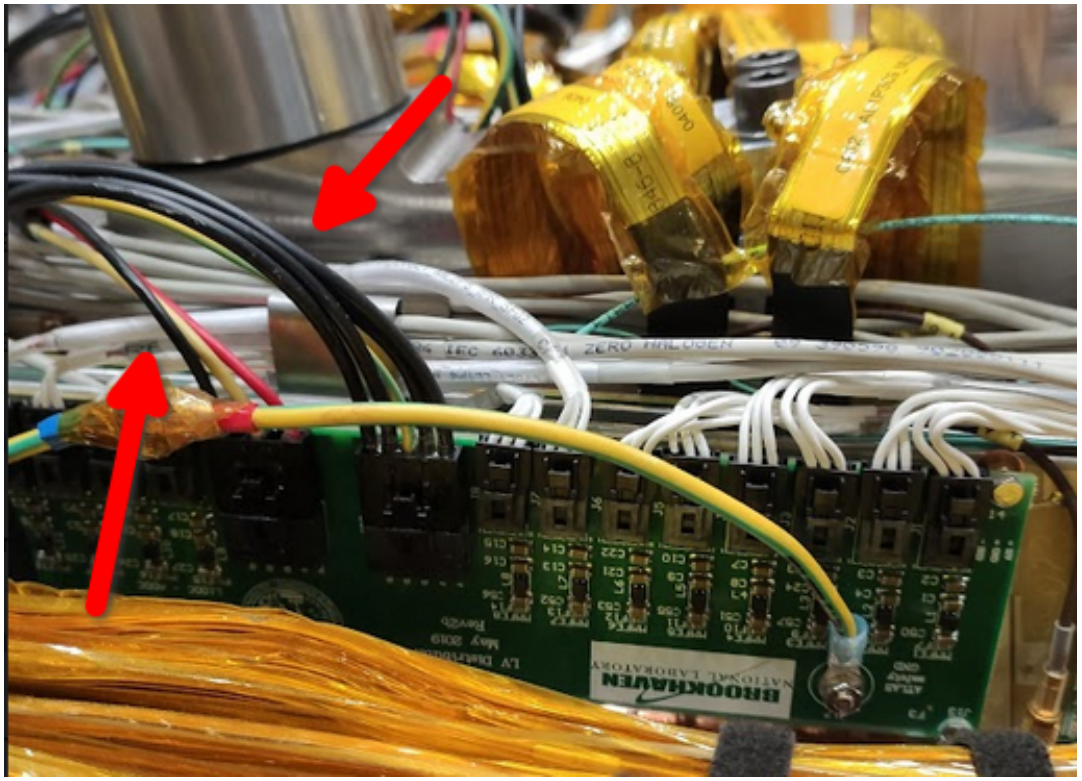

Figure 5.31: Example of "Bad" placement of the LVDB main input connectors.

6: Installation at Point 1

The ATLAS Experiment is located at Point 1. When each Wheel was fully assembled and commissioned, they were transported to their position in the ATLAS detector and later re-commissioned to determine their performance in the cavern and their condition after transportation.

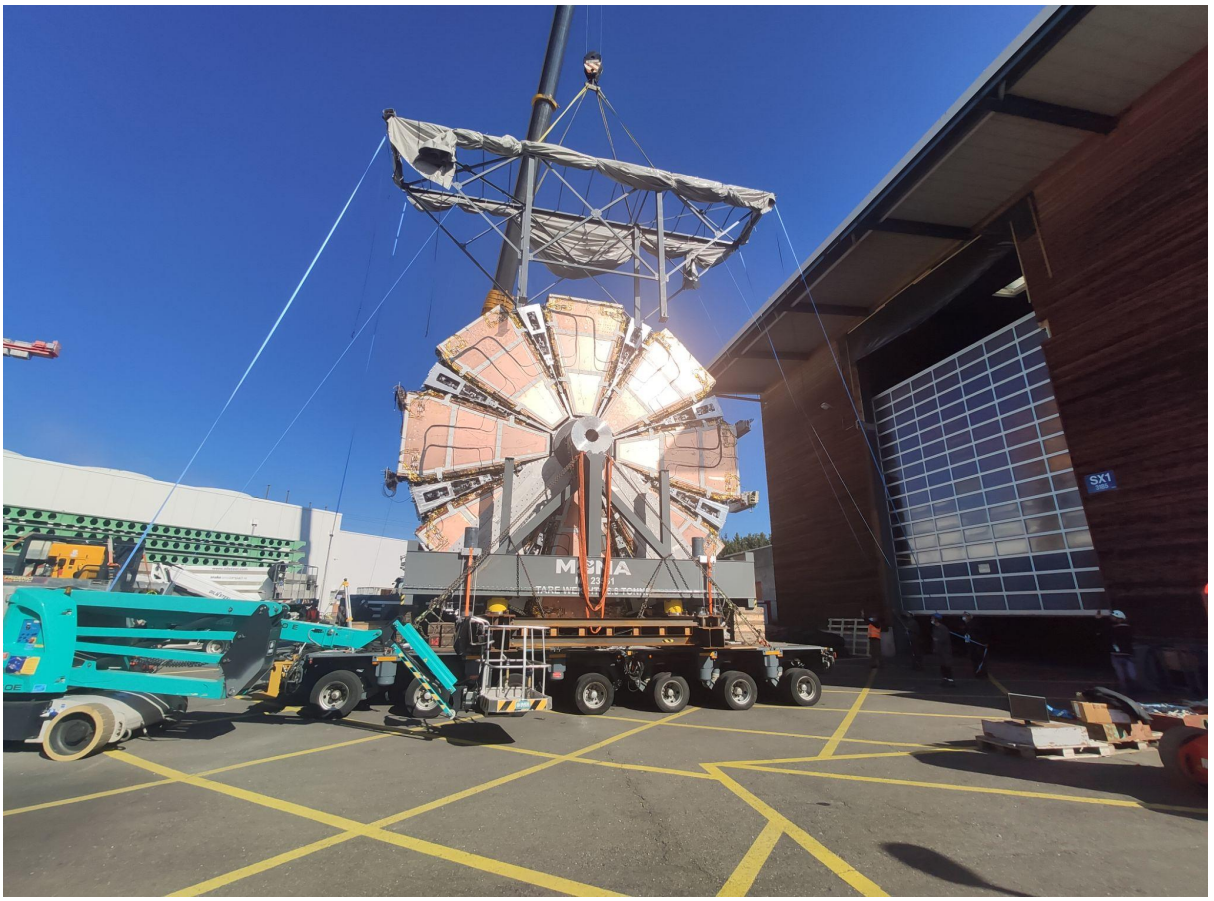

Figure 6.1: Arrival of NSW-C at Point 1.

The NSWs were transported from building 191 to Point 1 with the use of trucks and special mobile support structures. It was crucial for the wheels to be properly levelled on said structures and this is why extra attention was taken when placing the wheels on them. The transportation procedure took a lot of manpower and also coordination with local authorities, as traffic had to be stopped for the procedure to take place. This procedure of course happened on two occasions, first for Wheel A on the 6th of July 2021 and for Wheel C on the 14th of October 2021.

Figure 6.2: NSW-C in its transport protective contraption.

The wheels' placement in ATLAS was an entirely different procedure, as a combination of different cranes and sliders had to be used. The two wheels had to be lowered around 100 metres below ground level and then be put on their respective positions at the end-cap toroids.

Figure 6.3: Entrance point of ATLAS apparatus.

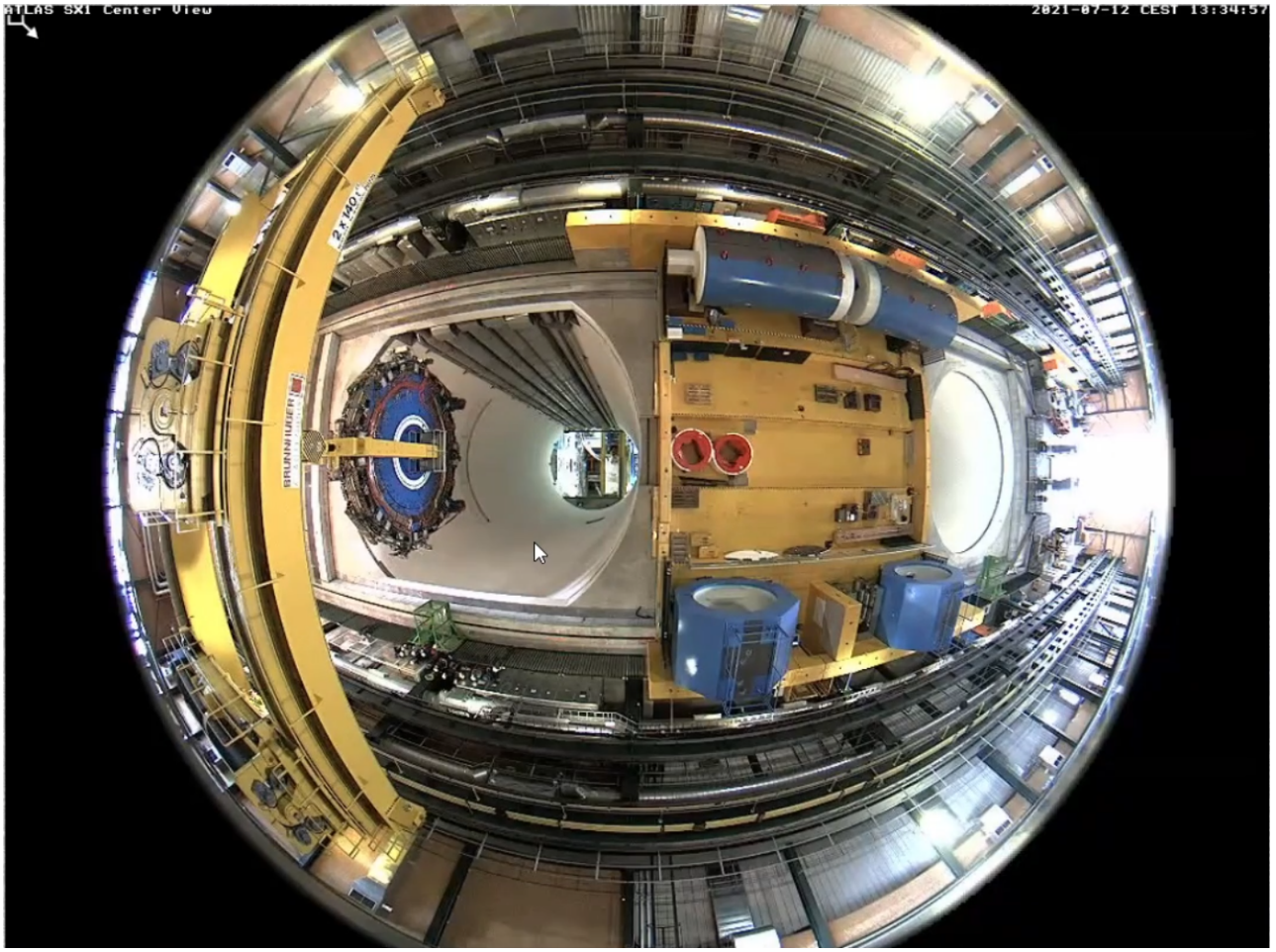

Figure 6.4: Lowering of NSW-A from ground level.

Once placed, at the end-cap toroids the wheels can be moved to either the maintenance or the run position. While at the maintenance position, technical interventions are possible with the placement of proper scaffolding as both the HO and IP sides are exposed. Several of these movements had to be made during the Point 1 installation and commissioning and will be made in the future for upgrades and maintenance.

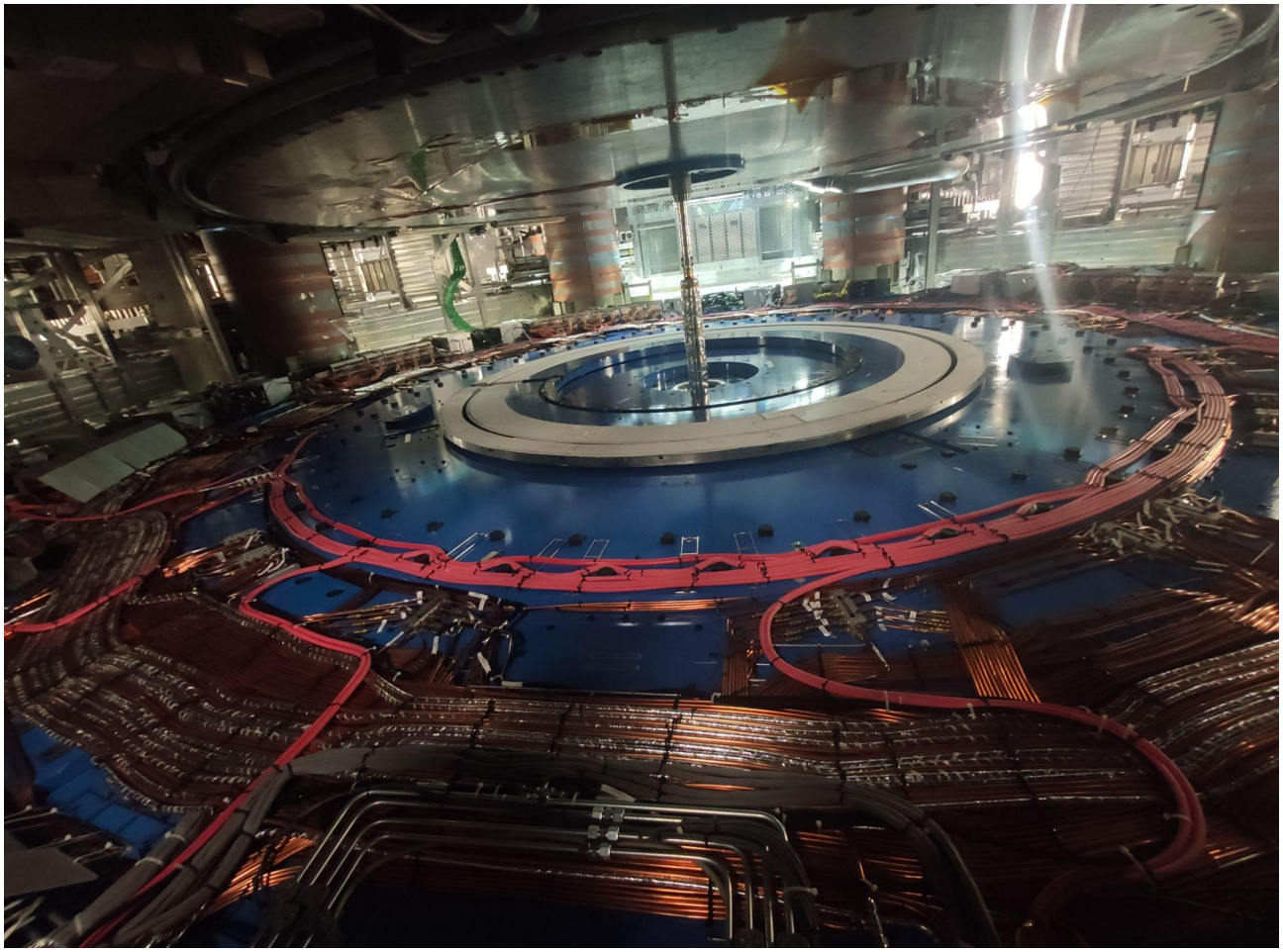

Figure 6.5: HO view of NSW-C at maintenance position with no scaffolding installed.

In a similar fashion to B191 each subsystem of each sector was separately tested to ensure the performance is on par with the tests before transportation. As expected, this was not always true. In several sectors, there were minor or even major differences in the performance measured. Also, some hardware problems occurred after installation, and some of them were impossible to reach and fix them.

Speaking of performance, noise in many sectors was on the same levels compared to B191 or even slightly less than that, reaching the noise levels that were recorded at BB5. On the other hand, some sectors showed more noise than expected, and some sectors had a serious problem with that.

One case of a sector that had a better noise performance than in B191 was sector A07. As seen in Figure 6.6, while this sector was in B191 it had serious noise problems on layers IP1 and IP2 but this problem disappeared when it was retested at P1. This could happen due to differences in the surrounding systems compared to B191 like the cooling unit or something that could not be defined, or it could even be due to reduced background interference. These effects were not global of course and each sector was affected in a different way. For example, during the movement, some of the aforementioned copper plates could have loosened up and the improved grounding situation might have been reversed for some sectors.

Note that most of the baseline graphs in this chapter are presented in comparison with the finalised situation of the noise levels of each sector at building 191 after the sector was considered fully commissioned.

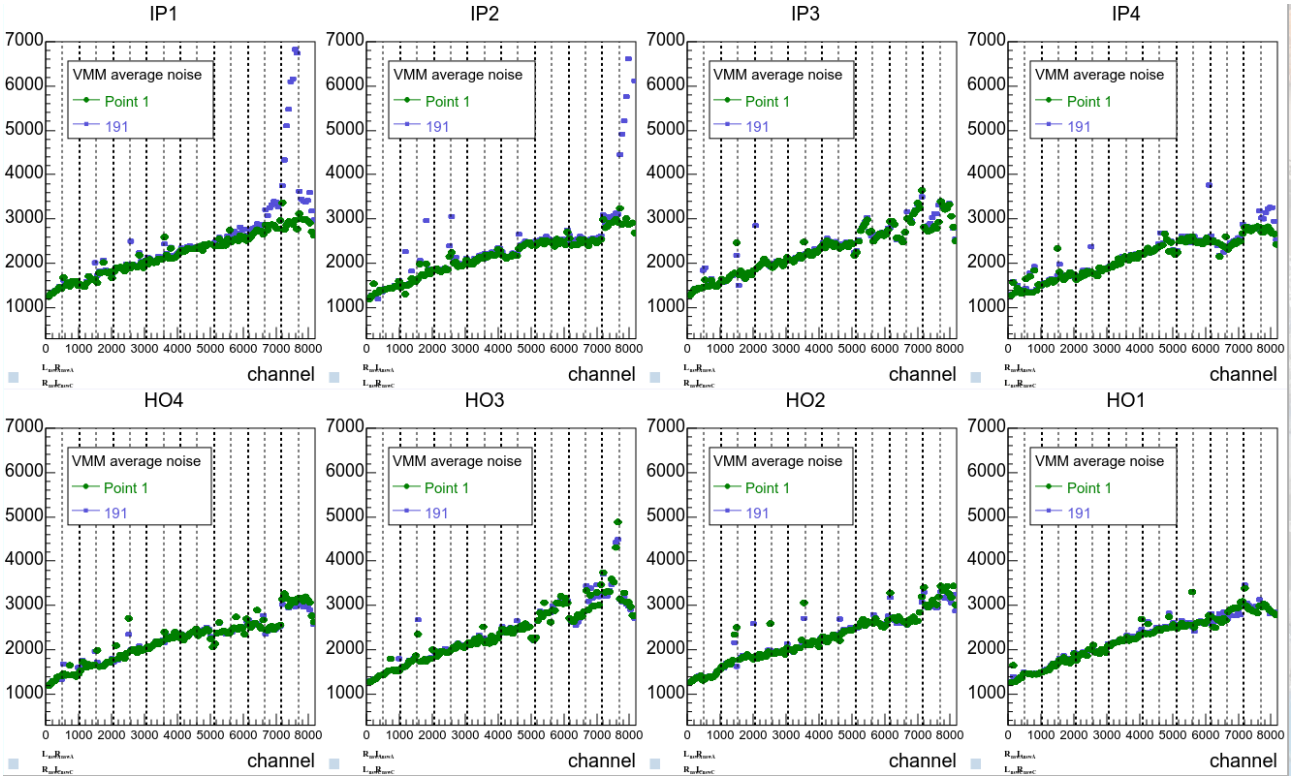

Figure 6.6: Sector A07 first run at P1 compared to B191 reference. Vertical units are ENC.

While some sectors like A07 have shown some improvement in noise levels, other sectors had the opposite effect. In Figure 6.7 one can clearly notice the problem of C09 performance in terms of noise compared to the noise on 191.

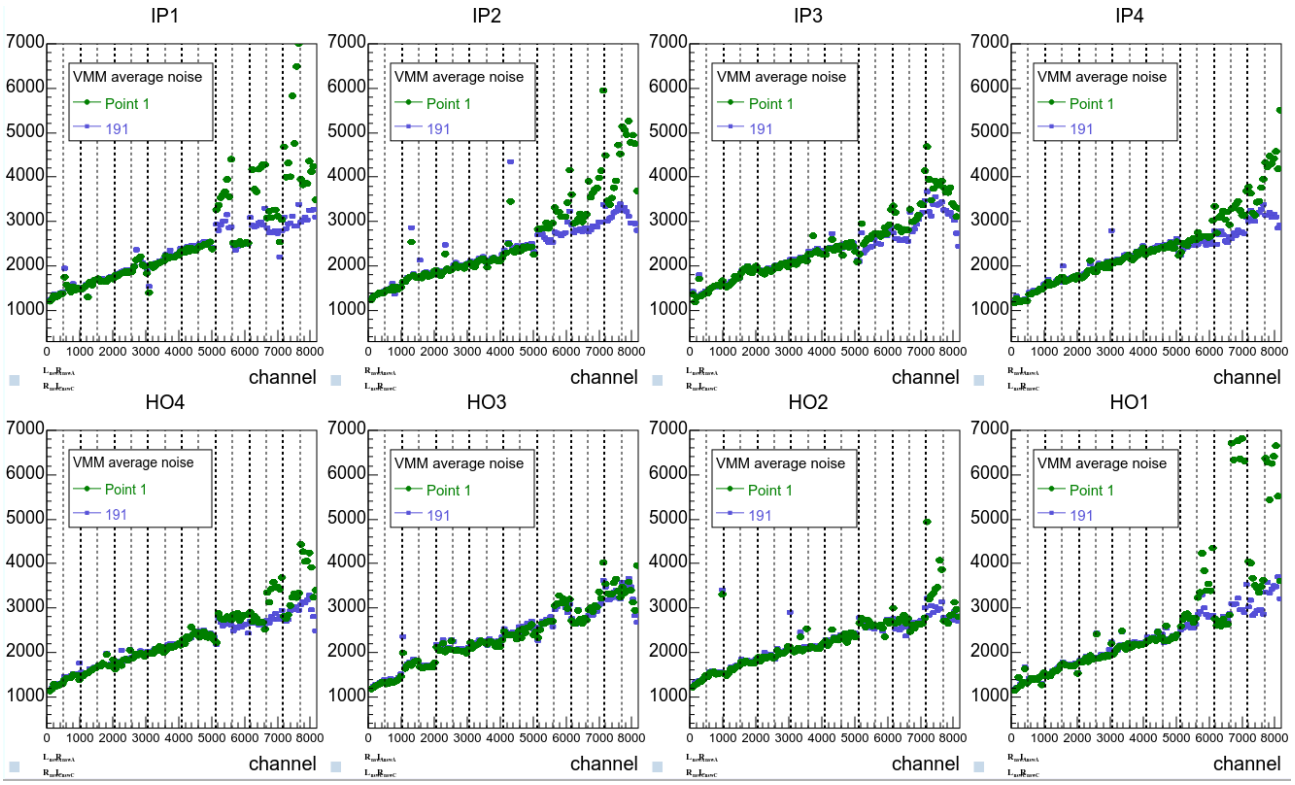

Figure 6.7: Sector C09 at P1 compared to B191 reference. Vertical units are ENC.

The noise levels in this sector are extremely high on layers IP2, IP4 and HO1 while for the rest of the layers are similar to the B191 reference. Using the experience from the commissioning in 191 the team suspected that the T-sensor subsystem could introduce this noise. Indeed, turning off the ELMB power supply of C09 made the following effect on the noise levels of that sector.

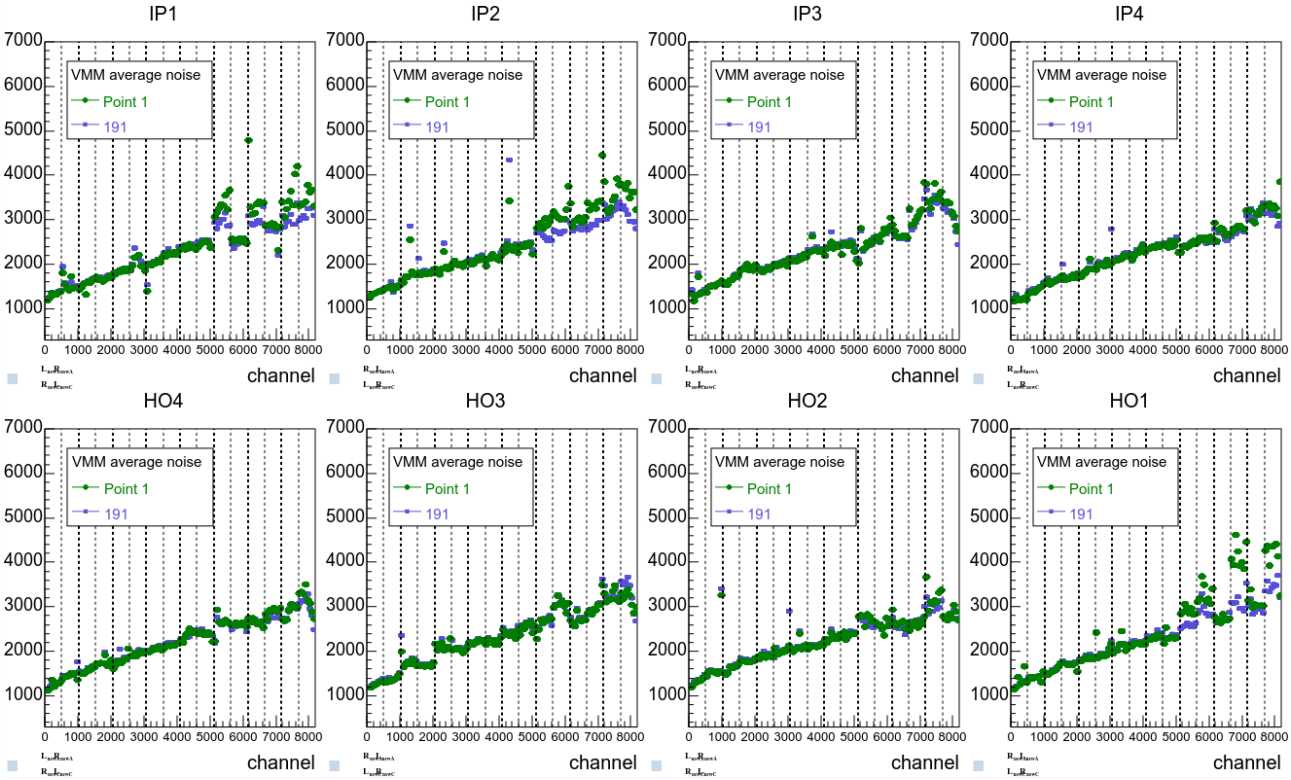

Figure 6.8: Sector C09 performance - ELMB off. Vertical units are ENC.

Looking at these baseline graphs makes it crystal clear that the power supply introduces all that noise, but since it is not a choice to leave the sector's temperatures unmonitored, some other solution than turning off the ELMBs had to be found.

The first thing to try was replacing the ELMB power supply cable with a new one and seeing the performance. On the first attempt the cable was not routed, and a significant difference in the noise levels could be noticed but the noise levels were still way too high. After that, the cable was then routed to its final position because it is obvious that it couldn't be left unrooted and hung in the air. Unfortunately, the noise got a little bit worse but kind of better than the old cable so another test was held, this time by partially unrooting, the cable part lying near the detector to see if the noise profile would change. The result was the same as can be seen. Subsequently, the cable was rerouted differently but the noise only got worse and the last thing to check was shortening the cable to avoid surplus parts of the routing without encouraging results. One could say that this configuration was the worst possible among all the others. Each of these runs and their performance results are shown in Figure 6.9 for the HO1 layer which was the worst of all in terms of noise levels.

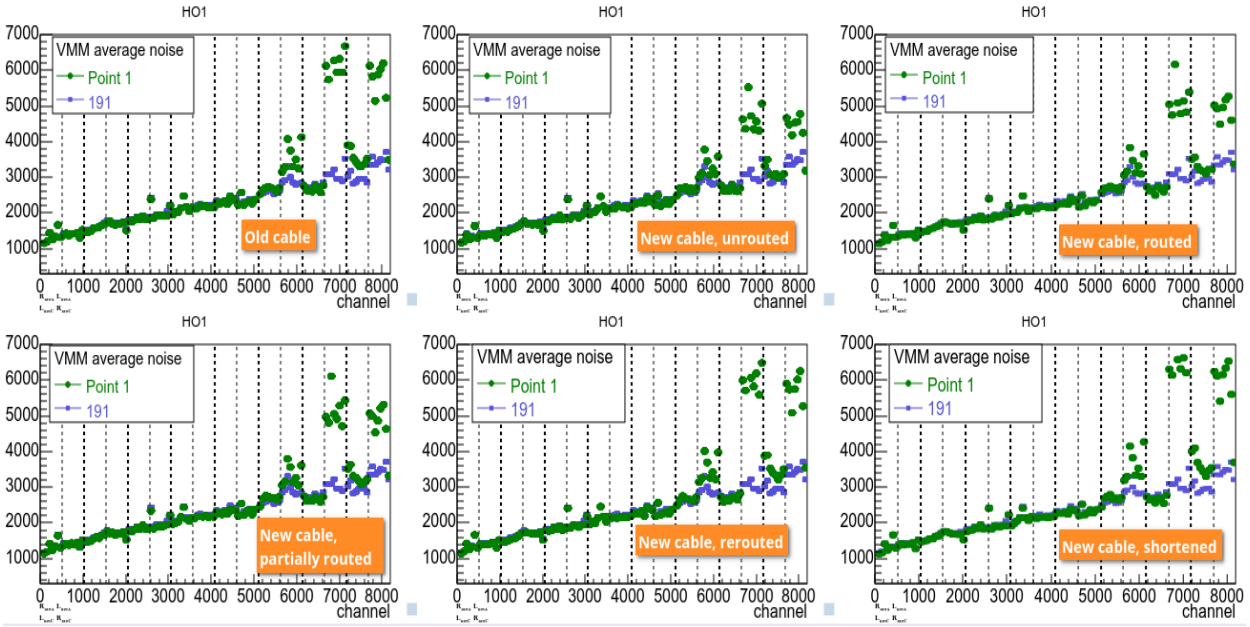

Figure 6.9: Different Configurations of the C09 ELMB cable and their effect on the HO1 layer. Vertical units are ENC.

Unfortunately, even at the time of presenting this thesis, the issue still needs to be resolved. Certain issues still need to be resolved and the most prominent reason for this is that interventions are harder at Point 1 since, as mentioned before, to have access to the sectors, the whole wheel has to be moved for access to be made possible.

There are also non-noise-related issues that have been faced during the Point 1 commissioning. One example of such an issue is Sector A14s burnt LVDB incident. On the 19th January of 2022, Sector A14 was fully operational. But after a few days on the 24th when the sector was turned on LVDB HOR L4 PCB8 Analog was blown and as a result, 8 MMFE8s were lost. The result of this damage can be seen in Figure 6.10.

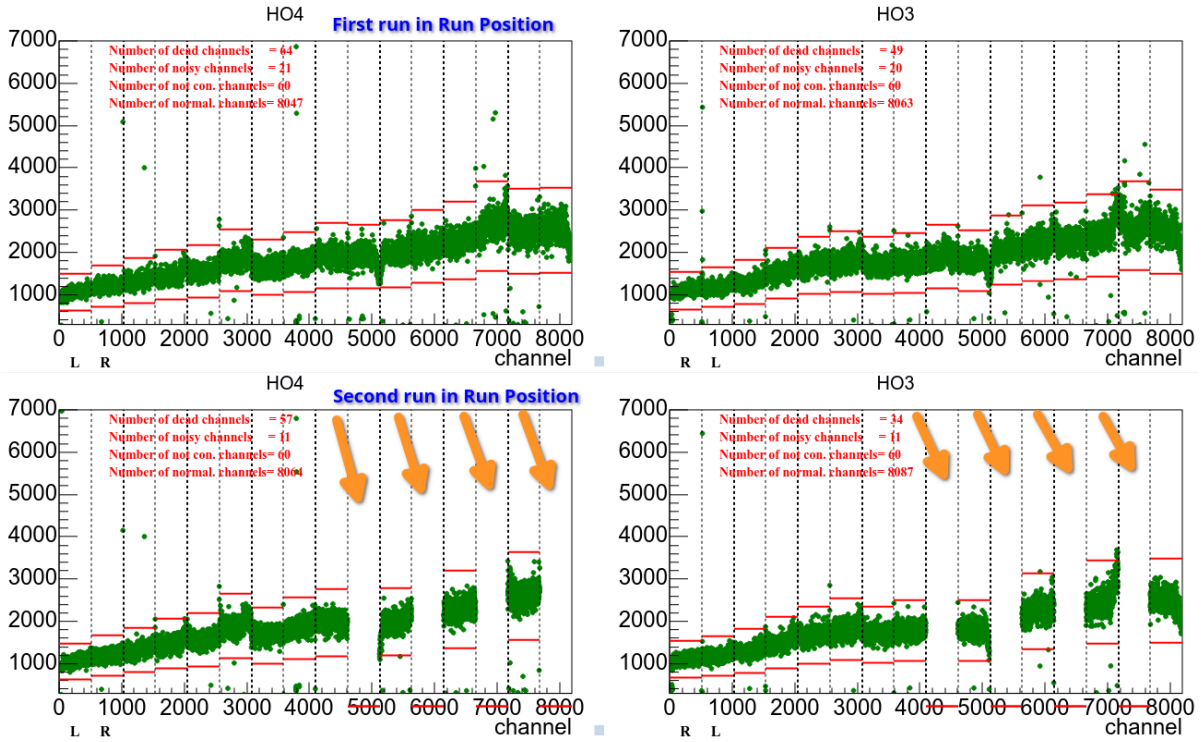

Figure 6.10: Sector A14 burnt LVDB issue. Vertical units are ENC.

Another issue that we faced was the loss of communication with some L1DDCs. During transportation and probably during the movement of the Wheels inside the cavern, a few individual fibres inside the fibre bundles between the LFB and the Felix machines (Section 3.5) could have been damaged. Thankfully there were two spare fibre pairs per bundle so if we were lucky enough it was only a matter of using said spare fibres. Four sectors have had this issue and for all of them, the issue was resolved. These sectors were A11, A16, C03, C09.

The list of all the open or known issues is maintained in the MicroMegas/sTGC expert manual and its current state as of writing this thesis can be seen in Figure 6.11.

Sector	Affected cards	Description
A04	MMFE8_L[1-2]P[1-4]_HOL	LVDB HOL L1 PCB2 Analog: blown fuse (already at 191, not fixable)
A06	MMFE8_L[1-2]P[1-4]_HOL and MMFE8_L[1-2]P[1-4]_HOR	LVDB HOL and HOR L1 PCB2 Analog: blown fuse (already at 191, not fixable)
A14	MMFE8_L[3-4]P[5-8]_HOR	LVDB HOR L4 PCB8 Analog seems to have a short, not fixable
A11		spare fiber: Fiber 861 (L1DDC_L4P4_HOR) moved from A6 (pc-tdq-flx-nsw-mm-03 device 2, link 11) to B3 (pc-tdq-flx-nsw-mm-04 device 1, link 5) slot in small box (nothing to be fixed here)
A16		spare fiber: LTX L3 IPL moved from A3 (device 2, link 2) to B3 (device 3, link 8) slot in small box (from 191, nothing needs to be fixed here)
C02	MMFE8_L[1-2]P[5-8]_HOL	LVDB HOL L1 PCB8 Analog (EIZ3C02 L1&L2 AnalogLeft OR) draws no current: faulty ICS connector (was fixed in 2022/02 but the problem came back on 2022/04/21)
C03		spare fiber: Fiber 1254 (L1DDC_L1P5_IPL) was moved from A2 (pc-tdq-flx-nsw-mm-06 device 2 link 1) to B3 (pc-tdq-flx-nsw-mm-07 device 1 Link 2)
C09		spare fiber: Fiber 1443 (L1DDC_L1P4_IPL) was moved from A1 (device 1 link 0) to spare-fiber slot B3 (device 0 link 2)
A03	MMFE8_L[1-2]P[1-8]_IP[L-R]	EIZ2A03 Digital L1-L2 and EIZ2A03 Analog Left L1&L2 merged to the same channel, that failed.

Figure 6.11: Known issues of the MicroMegas detectors.

7: Conclusions

This thesis is the result of one and a half years of commissioning work from the authors as part of the collaboration between ATLAS and the University of West Attica. During the COVID-19 pandemic, the ATLAS project has fallen far behind schedule and on top of that complications caused by noise issues mostly have made the need of extra manpower necessary. For these reasons, the authors have been called to join the MicroMegas commissioning team, among other people in order to increase productivity and be able to meet the strict deadlines that were set along the course of the ATLAS project.

During their stay there, they developed a great understanding of the system and the common troubleshooting steps, which as a result, brought them to a position where they could actively contribute and also train new people that eventually kept coming to the experiment for longer or shorter periods of time. All of the described resolutions in chapters 4, 5, and 6 which are related to the typical commissioning workflow, the troubleshooting and the installation at Point 1 had the active participation of the authors who were actively supporting the commissioning process developing also the experience to indicate issues and solutions or even work independently to deliver the desired results mostly on the typical workflow process but also on the troubleshooting.

The commissioning proved to be a non-smooth process since while facing a problem that came up for the first time, it could take from a day to even several weeks to be resolved. Especially the excessive noise levels in some sectors were a massive struggle before it was resolved because many things could be blamed as possible sources of noise. They were thoroughly investigated before applying the optimal solutions.

Other problems also appeared, such as the bad grounding of the New Small Wheel and the MicroMegas sectors. This was particularly relevant to the noise and proved to be a serious challenge for the commissioning. Looking for possible interventions was demanding, especially for the side A NSW MM sectors that had already left the integration stage. Modifications had to be performed on the wheel for side A while for the side C sectors, some interventions were possible during their integration stage.

On top of these, unexpected things could arise such as damages or minor problems in the communication between the subsystems such as damaged optical fibres, bad connections, and completely damaged connectors that in many cases needed time-consuming and difficult interventions to be resolved just for the sector to return to working order before checking the effect of each possible fix on any of the problems that were being resolved each time.

After all, the commissioning and the assembly were finished for both of the wheels, they were put in the cavern in their foreseen positions in the ATLAS detector where they were recommissioned in their final position in the environment that they designed to be working, which was obviously different from conditions in the building that they were assembled and commissioned initially. Indeed their performance was slightly - or in some cases even quite - different because of the new environmental conditions. In the end, some of these problems were resolved while other problems such as burnt fuses or damaged connectors were unable to be fixed because they were unreachable from any possible point. These issues are known and are kept in a list so anyone who tries to retrieve data from the MM detectors is informed about what data cannot be collected from which specific cards.

References

[1] CERN home page - https://home.cern/

[2] CERN member states https://home.cern/about/who-we-are/our-governance/member-states

[3] EXTRAORDINARY CLOSED COUNCIL 206 th Session 8 March 2022 CERN/3626

[4] CLOSED COUNCIL 207th Session 25 March 2022 CERN/3638/Corr.

[5] LHC website - https://home.cern/science/accelerators/large-hadron-collider

[6] CERN's accelerator complex - https://www.home.cern/science/accelerators/accelerator-complex

[7] LHC collisions - https://lhc-machine-outreach.web.cern.ch/collisions.htm

[8] Facts and figures about the LHC - https://home.cern/resources/faqs/facts-and-figures-about-lhc

[9] CMS experiment - https://home.cern/about/experiments/cms

[10] ALICE experiment - https://home.cern/science/experiments/alice

[11] LHCb experiment - https://home.cern/science/experiments/lhcb

[12] TOTEM experiment - https://home.cern/science/experiments/totem

[13] LHCf experiment - https://home.cern/science/experiments/lhcf

[14] MoEDAL - MAPP experiment - https://home.cern/science/experiments/moedal-mapp

[15] ATLAS experiment - https://home.cern/science/experiments/atlas

[16] The ATLAS detector layout - https://www.researchgate.net/figure/The-ATLAS-detector-layout-40_fig9_274319826

[17] ATLAS Collaboration. ATLAS inner detector : Technical Design Report, 1. ATLAS TDR 4 Volume 1; CERN-LHCC-97-16. Geneva: CERN, 1997.

[18] ATLAS pixel detector electronics and sensors G. Aad et al., JINST 3 P07007 (2008), DOI: 10.1088/1748-0221/3/07/P07007

[19] The Silicon microstrip sensors of the ATLAS semiconductor tracker, Carter et al, Nucl. Instrum. Meth. A578 98-118 (2007), DOI 10.1016/j.nima.2007.04.157

[20] The ATLAS Transition Radiation Tracker (TRT) proportional drift tube: Design and performance, ATLAS TRT Collaboration, J. Instrum. 3 (2008) P02013. DOI: 10.1088/1748-0221/3/02/P02013

[21] The ATLAS Calorimeter - https://atlas.cern/Discover/Detector/Calorimeter

[22] ATLAS calorimetry - https://www.mpp.mpg.de/en/research/structure-of-matter/atlas-detector-particle-collisions-at-the-lhc/atlas-calorimetry/

[23] ATLAS Calorimeter | Brookhaven and the LHC - https://www.bnl.gov/atlas/lar.php

[24] ATLAS Collaboration. ATLAS calorimeter performance: Technical Design Report. ATLAS TDR 1; CERN LHCC 960 40. Geneva: CERN, 1996.

[25] ATLAS Collaboration. ATLAS liquid argon calorimeter: Technical Design Report. ATLAS TDR 2; CERN LHCC 96 041. Geneva: CERN, 1996.

[26] ATLAS Collaboration. ATLAS tile calorimeter: Technical Design Report. ATLAS TDR 3; CERN LHCC 96 042. Geneva: CERN, 1996.

[27] The ATLAS Muon Spectrometer - https://atlas.cern/Discover/Detector/Muon-Spectrometer

[28] The ATLAS Magnet Sytem - https://atlas.cern/Discover/Detector/Magnet-System

[29] ATLAS Collaboration. ATLAS magnet system : Technical Design Report, 1. ATLAS TDR 6; CERN-LHCC-97-18: Geneva: CERN, 1997

[30] ATLAS Collaboration. ATLAS central solenoid : Technical Design Report. ATLAS TDR 9; CERN-LHCC-97-21: Geneva: CERN, 1997.

[31] ATLAS Collaboration. ATLAS barrel toroid : Technical Design Report. ATLAS TDR 7; CERN-LHCC-97-19: Geneva: CERN, 1997.

[32] ATLAS Collaboration. ATLAS end-cap toroids : Technical Design Report. ATLAS TDR 8; CERN-LHCC-97-020; Geneva: CERN, 1997.

[33] Trigger and Data Acquisition System - https://atlas.cern/Discover/Detector/Trigger-DAQ

[34] Owen, Rhys Edward [ATLAS Collaboration]. The ATLAS Trigger System; ATL-DAQ-SLIDE-2018-074: Puebla City, Mexico, 2018

[35] ATLAS Collaboration. Technical Design Report for the Phase-II Upgrade of the ATLAS TDAQ System. ATLAS-TDR-029; CERN-LHCC-2017-020; Geneva: CERN, 2017

[36] Affolder, Tony [ATLAS Collaboration]. ATLAS Phase II Upgrade. ATL-UPGRADE-SLIDE-2021-734; Manchester, 2022.

[37] ATLAS Collaboration. Letter of Intent for the Phase-I Upgrade of the ATLAS Experiment. CERN-LHCC-2011-012 ; LHCC-I-020; Geneva, CERN, 2011.

[38] ATLAS Collaboration. New Small Wheel Technical Design Report. ATLAS-TDR-020; CERN-LHCC-2013-006; Geneva, CERN, 2013.

[39] Mancini, Giada [ATLAS Collaboration]. Ready for LHC Run III - The ATLAS New Small Wheel and the MicroMegas chambers performances. ATL-MUON-SLIDE-2022-642;

[40] Guan, Liang [ATLAS Collaboration]. Performance of the ATLAS New Small Wheels in preparation for LHC Run-3 data-taking. ATL-MUO-PROC-2022-001: Bologna, Italy, 2022.

[41] Press release: The 1992 Nobel Prize in Physics - https://www.nobelprize.org/prizes/physics/1992/press-release/

[42] MICROMEGAS: a high-granularity position-sensitive gaseous detector for high particle-flux environments Y. Giomataris'*, Ph. Rebourgeard", J.P. Robert", G. Charpakb

[43] Vogel, Fabian [ATLAS Collaboration]. Test of ATLAS Micromegas detectors with a ternary gas mixture at the CERN GIF++ facility. ATL-MUON-PROC-2021-009;

[44] Bianco, Michele [ATLAS Collaboration]. Micromegas detectors for the muon spectrometer upgrade of the ATLAS experiment. ATL-MUON-SLIDE-2015-334;

[45] Ntekas, K; Alexopoulos, T; Zimmermann, S [ATLAS Collaboration]. The ATLAS New Small Wheel Upgrade Project. ATL-MUON-PROC-2014-004; Amsterdam, Netherlands, 2014.

[46] Gkountoumis, Panagiotis [ATLAS Collaboration]. Level-1 Data Driver Card of the ATLAS New Small Wheel Upgrade Compatible with the Phase II 1 MHz Readout. ATL-MUON-SLIDE-2016-216: Thessaloniki, Greece, 2015.

[47] Viaux Maira, Nicolas [ATLAS Collaboration]. The ATLAS New Small Wheel new Muon Stations Ready for LHC Run3. ATL-MUON-PROC-2022-003; La Biodola - Isola D'elba, Italy, 2022.

[48] P. Gkountoumis [ATLAS Muon Collaboration], "Level1 Data Driver Card of the ATLAS New Small Wheel upgrade," doi:10.1109/NSSMIC.2015.7581785 56 S. Ryu, FELIX: the detector readout upgrade of the ATLAS experiment, ATL-DAQ-SLIDE-2015-558 (2015).

[49] Politis, Epameinondas. Configuration and testing of the Micromegas detectors' data acquisition and transmission card (L1DDC) for the upgrades of the ATLAS experiment. Athens: UniWA 2019.

[50] Popa, Stefan. The Read Out Controller ASIC for the ATLAS Experiment at LHC. CERN-THESIS-2021-159. Geneva: CERN 2021.

[51] Tzanis, Polyneikis [ATLAS Muon Collaboration]. Development of the Configuration, Calibration and Monitoring System of the New Small Wheel Electronics for the ATLAS experiment. ATL-MUON-PROC-2021-005. 2021.

[52] Wang, Jinhong; Guan, Liang; Sang, Ziru; Chapman, J.W.; Dai, Tiesheng; Zhou, Bing; Zhu, Junjie. Characterization of a Serializer ASIC chip for the upgrade of the ATLAS muon detector. arXiv:1509.06636; DOI: 10.1109/TNS.2015.2480855; IEEE Trans. Nucl. Sci. 62 (2015) 3242-3248. 2015.

[53] Iakovidis, George [ATLAS Muon Collaboration]. VMM3, an ASIC for Micropattern Detectors. DOI: 10.22323/1.322.0035. 2017.

[54] GBTX Manual - https://espace.cern.ch/GBT-Project/GBTX/Manuals/gbtxManual.pdf

[55] Vafeiadis, Theodoros [ATLAS Collaboration]. Integration and commissioning of ATLAS New Small Wheel Micromegas detectors with electronics at CERN. ATL-MUON-PROC-2020-021; DOI: 10.22323/1.390.0791; ICHEP 2020.

[56] Haas, Stefan; Ask, S; Berge, D; Ellis, Nick; Farthouat, P; Krasznahorkay, A; Debrecen U. ; Pauly, T; Schuler, G; Spiwoks, R ; Wengler, T. The Octant Module of the ATLAS Level-1 Muon to Central Trigger Processor Interface. ATL-DAQ-CONF-2007-019 ; ATL-COM-DAQ-2007-025 ; CERN-ATL-COM-DAQ-2007-025; DOI: 10.5170/CERN-2007-001.319. Geneva: CERN, 2007.

[57] Ulrich Landgraf: NSW cooling system and distribution. ATLAS Weekly 22.06.2016.

[58] Ulrich Landgraf: Cooling Commissioning Steps. ATLAS Weekly. 15.03.2019

[59] Sahal Yacoob: MM b191 Gas supply configuration. ATLAS Weekly. 12.04.2021.

[60] Internal Atlas Report (Private)

[61] NGPS - User's Manual - https://www.caenels.com/wp-content/uploads/2015/12/NGPS-User_s-Manual-v1.6_web.pdf

[62] CAEN Manual: EASY 6000 System for Atlas NSW ICS Rev. 2 - 24 February 2020 - https://www.caen.it/?downloadfile=5267

[63] EASY BRIC B and Rad tolerant Intermediate Converter - https://www.caen.it/products/easy-bric1/

[64] STAR MTP to LC MODULE - https://www.fibernet-tech.com/product/star-mtp-to-lc-module/

[65] Micromegas Weekly Report. ATLAS Weekly. 08.02.2021.

[66] Micromegas Weekly Report. ATLAS Weekly. 08.03.2021.

[67] CLOSED COUNCIL 207th Session 25 March 2022 CERN/3637/Corr.

Acronyms

AC: Alternate Current
ADDC: ART Data Driver Card
ALICE: A Large Ion Collider Experiment
ART: Address in Real Time
ASIC: Application Specific Integrated Circuit
ATLAS: A Toroidal LHC ApparatuS
BC: Bunch Crossing
BCID: Bunch Crossing ID
BRIC: B and Rad tolerant Intermediate Converter
CERN: Conseil Européen pour la Recherche Nucléaire
CMS: Compact Muon Solenoid
COTS: Commercial off-the-shelf
CSC: Cathode Strip Chamber
DAQ: Data Acquisition System
DC: Direct Current
DCS: Detector Control System
ELMB: Embedded Local Monitor Board
ELX: Electronics
ENC: Electronic Noise Charge
FCal: Forward Calorimeter
FE: Front End
FELIX: Front-End Link eXchange
fFEX: forward Feature EXtractor
FPGA: Field Programmable Gate Array
FSM: Finite State Machine
FTK: Fast TracKer
GBTx: Gigabit Transceiver
GUI: Graphical User Interface
HL-LHC: High Luminosity LHC
HLT: High Level Trigger
HO: The side of a detector facing towards the HO structure, i.e. facing away from the Interaction Point
HV: High Voltage
I/O: Input/Output
ICS: Intermediate Conversion Stage
ID: Inner Detector
IP: Interaction Point
JD: The shielding structure of the New Small Wheel
JINR: Joint Institute for Nuclear Research
L1DDC: Level-1 Data Driver Card
LAr: Liquid Argon Calorimeter
LC: Lucent Connector
LED: Light Emitting Diode

LFB: Large Fibre Box
LHC: Large Hadron Collider
LHCb: Large Hadron Collider beauty
LHCf: Large Hadron Collider forward
LS: Large Sector
LTI: Local Trigger Interface
LV: Low Voltage
LVDB: Low Voltage Distribution Board
MDT: Monitored Drift Tubes
MM: MicroMegas
MMFE8: MicroMegas Front End Boards
MoEDAL: Monopole and Exotics Detector at the LHC
MTP: Multi-fiber Termination Push-on
NGPS: New Generation Power Supply
NSW: New Small Wheel
OPC: Open Platform Communications
PCB: Printed Circuit Board
PS: Proton Synchrotron
PSB: Proton Synchrotron Booster
R&D: Research and Development
RIM: The literal rim of the New Small Wheel
RMS: Root Mean Square
ROC: Read-Out Controller
ROD: Read-Out Device
ROI: Regions of Interest
RPC: Resistive Plate Chambers
Rx: Receive Direction
SCA: Slow Control Adapter
SCSI: Small Computer System Interface
SCT: Semiconductor Tracker
SFB: Small Fibre Boxes
SFP: Small Form-factor Pluggable
SS: Small Sector
sTGC: Small-strip Thin Gas Chambers
SW: Small Wheel
T-sensor: Temperature Sensor
TGC: Thin Gap Chambers
TileCal: Tile Calorimeter
TOTEM: TOTal Elastic and diffractive cross section Measurement
TRT: Transition Radiation Tracker
TTC: Trigger and Control system
Tx: Transmit Direction
UNESCO: United Nations Educational, Scientific and Cultural Organization
USB: Universal Serial Bus
VMM: Venetios MicroMegas